An In-depth Study of the On-disc Counterpart to Type II Spicules

by

Dan Henrik Sekse

Submitted
in partial fulfillment of the requirements
for the degree of

Philosophiæ Doctor

Institute of Theoretical Astrophysics
Faculty of Mathematics and Natural Science
University of Oslo
Oslo, Norway
March, 2013

Series of dissertations submitted to the
Faculty of Mathematics and Natural Sciences, University of Oslo
No. 1349

ISSN 1501-7710

Cover: Inger Sandved Anfinsen.
Printed in Norway: AIT Oslo AS.

Produced in co-operation with Akademika Publishing.
The thesis is produced by Akademika publishing merely in connection with the thesis defence. Kindly direct all inquiries regarding the thesis to the copyright holder or the unit which grants the doctorate.

Acknowledgements

My Ph.D. at the Institute of Theoretical Astrophysics in Oslo became a reality mainly thanks to Mats Carlsson, who persuaded me to accept a position in the solar physics group even though my initial application was for cosmology. My four years at ITA have been a great experience and for this I am very grateful.

This thesis would never have been completed without the excellent supervision of Luc Rouppe van der Voort, who has always been available for guidance and discussions (mainly about work, but also skiing and skating). In addition, I would like to thank Bart De Pontieu, whose knowledge and ideas guided the investigation throughout this work and who invited me to an extended visit to LMSAL which I will always remember fondly.

Furthermore, a big thanks to my office mates: Sandro, Patrick, Bhavna, and Amir, for all their help and understanding over the years. And for all those who filled my days at the ITA with laughter and discussions, cheers for the coffee, I hope you (Viggo, Sven, Jorrit, Per, Borris, Eamon, Håkon, Thomas, and Ada) won't miss me too much during the coming coffee breaks. A special thanks goes to my office mate Kosovare, who began her road towards a Ph.D. on the same day as me and has been my "canary down the mine" for the past four years, Gregal and Torben, for making several trips to La Palma very enjoyable, and Pit, who was indispensable during our observations. And to Nuno, rest assured you have not been forgotten, and I think everyone I have worked with will agree that the days at the Institute would not have been the same without you.

Finally, I have to thank my family for standing by me for all the years before and during my Ph.D., in particular my fiancée, Anne-Lise, who have supported me every step of the way, and my son, Vetle, who, during my final work to finish this thesis, showed me that there are much more important things to life, such as sleep, food, and lots of fun and laughter.

Research is what I'm doing
when I don't know what I'm doing.
-Wernher von Braun-

Contents

Part I

Introduction

Chapter 1

The Sun

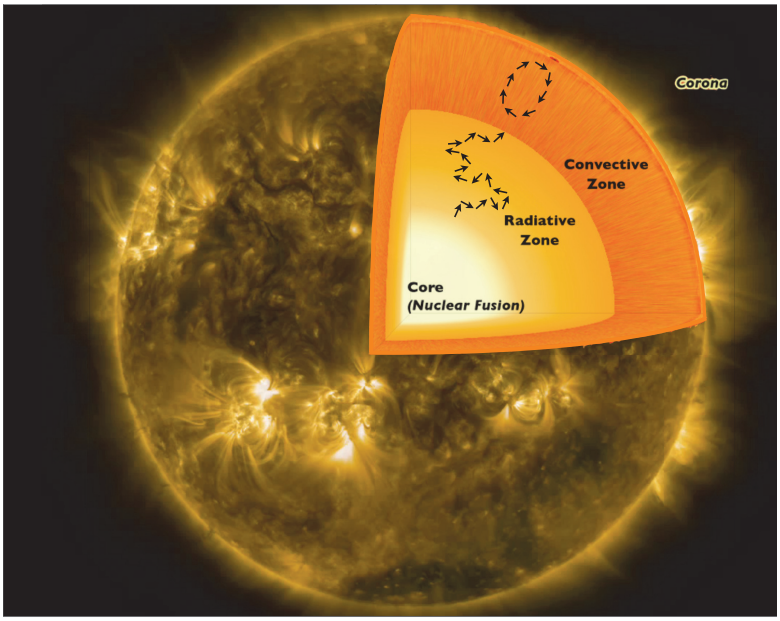

Figure 1.1: The Sun seen from NASA's Solar Dynamics Observatory in the 171 Å channel. A cut displaying the interior structure of the Sun and the energy transport from the solar centre to the surface through a random walk of photons and convection is drawn on top of the image.

The Sun, like most stars, is a huge ball of hydrogen and helium plasma with a few percent of other elements and gets its energy from nuclear fusion

in the core. In newborn stars, the energy release is solely from the fusion of hydrogen into helium, a process that will continue until there is no more hydrogen left in the core. Depending on the original size of the star, it will either stop releasing energy in the core after the hydrogen burning or continue with the fusion of heavier elements into even heavier elements. Either way, after the hydrogen in the core is depleted, the main lifetime of the star is over, and each process after this will take only a small fraction of the total lifetime. For a G2V star, like the Sun, the process of hydrogen fusion lasts for roughly 10 billion years, a period in which the Sun remains stable and burns roughly 600 tons of hydrogen per second. The energy produced in the core is then transported to the surface of the Sun through a couple of different mechanisms. Firstly, the energy is transported through the radiative zone, which stretches from the core to $0.7R_{\odot}$, by radiation. This means that photons created in the core have to make their way outwards towards the surface. Because of the small mean free path due to high density in the radiative zone, these photons collide with atoms all the time and are being absorbed and reemitted. When they are reemitted this happens in a random direction causing the photons to move through the entire radiation zone in a random walk (see Fig. 1.1). After walking randomly through the radiative zone for 170000 years, the photons finally reach the convective zone. Now the energy can be transported the rest of the way to the surface by means of convection, which, in the Sun, is a mechanism of hot plasma close to the radiative zone rising towards the surface while the colder plasma at the surface falls back down towards the radiative zone. This final journey takes about a week to complete and the temperature has gone down from approximately 16 million K at the core to roughly 5800 K at the surface. After a journey of 170000 years and 1 week the energy, once created in the centre of the Sun, have reached the photosphere (surface) and can finally move freely further out into the solar system (more information on the Sun in general can be found in e.g. Priest 1982; Carroll & Ostlie 2006).

1.1 The Solar Atmosphere

1.1.1 The Photosphere

Every gas has an optical depth which is a measure of the number of mean free paths needed to travel through the gas. In the case of the Sun, everything below the surface has an optical depth, τ, larger than one. Hence, photons in this region have to travel farther than its mean free path in order to reach the surface and will most likely be scattered again. Once τ equals one, the photons only need 1 mean free path through the rest of the plasma and will be able to travel the distance to us without further scattering,which means they are the photons we observe. Hence, where τ=1 becomes the "surface" known as the photosphere, meaning "sphere of light", and is the region of

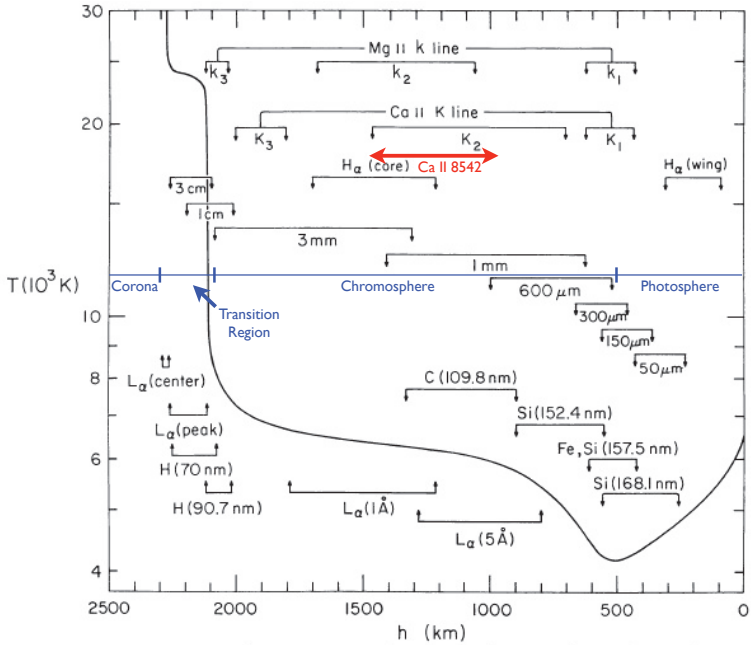

Figure 1.2: Temperature stratification in the VAL3C model of the solar atmosphere (Vernazza et al. 1981) with indicators of the formation height of different spectral lines (the formation height range of Ca II 8542 in red provided by Jorrit Leenaarts). The blue line shows the height range of the different atmospheric layers.

the Sun from which we receive most of our radiation (for a more detailed coverage of the photosphere, see e.g. Priest 1982; Foukal 2004). This 500 km thick layer (see Fig. 1.2) is located approximately 696000 km from the centre of the Sun, has an average temperature of 5800 K, and is dominated by a hexagonal pattern called granulation (see Fig. 1.3). The granulation pattern is a direct result of convection where hot plasma rises up from below in the centre of the granules, while the dark intergranular lanes are formed by cooler plasma falling down into the convection zone. These granules are on average about 1 Mm across and live for approximately 6 minutes (Stein & Nordlund 1998; Priest 1982).

The pressure exerted by the gas in the photosphere is much higher than the magnetic pressure, which causes the magnetic field to be rooted in the plasma and having to follow the motions in the solar surface. This leads to

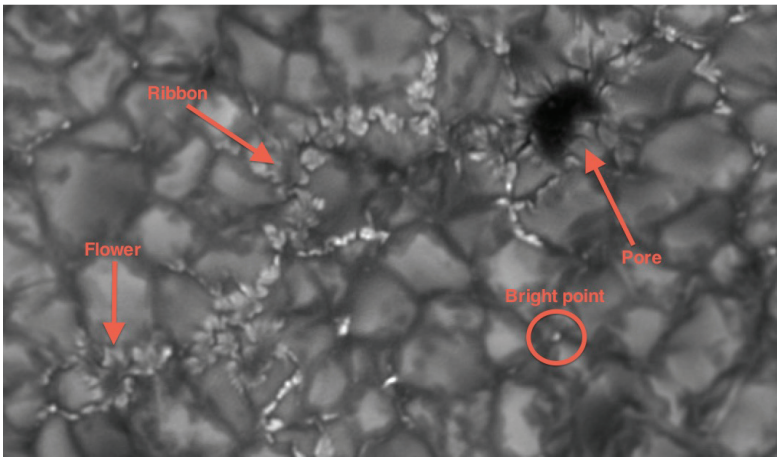

Figure 1.3: An unprecedented high quality image of the photosphere as seen from the Swedish 1-m Solar Telescope displaying bright points, ribbons, flowers, and a micro-pore. Courtesy of Luc Rouppe van der Voort.

the magnetic field in the photosphere being concentrated in the intergranular lanes due to hot plasma rising up in the middle of granules, pushing both matter and magnetic fields to the sides. Although the intergranular lanes are usually cold and dark compared to the rest of the granule, there are small bright points scattered around in these dark lanes. These bright points are small regions with enhanced magnetic flux (concentration of magnetic field) which pushes plasma away causing this region to be less dense than its surroundings. Less dense means a larger mean free path and, subsequently, a smaller optical depth, resulting in radiation escaping from lower layers of the Sun where the temperature is higher (appears brighter) (Spruit 1976). When bright points cluster together they can form ribbons, where they follow an intergranular lane and develop a darker line in the middle, or flowers, which is a circular manifestation of a ribbon with a dark centre (see Fig. 1.3) (Berger et al. 2004). If the collection of bright points exceed approximately 1 arcsec in size they will normally form dark pores. Here the magnetic flux is high enough to slow the convection of hot plasma from deeper down in the convection zone to the point where it results in a noticeably lower temperature than the photospheric average (Spruit 1977). This explains why dark pores are dark and bright points are bright even though both allows us to see layers of the Sun deeper down than the photosphere. It is also the reason why ribbons and flowers develop dark centres where convection is starting to break down, as these are showing the evolution of a

collection of bright points that might evolve into a pore. The final, largest, and by far most renowned feature in the photosphere is the sunspot. These appear when dark pores grow, combine, and become strong enough to form a penumbra, which is the brighter filamentary region surrounding the dark centre of the sunspot, called the umbra.

1.1.2 The Chromosphere

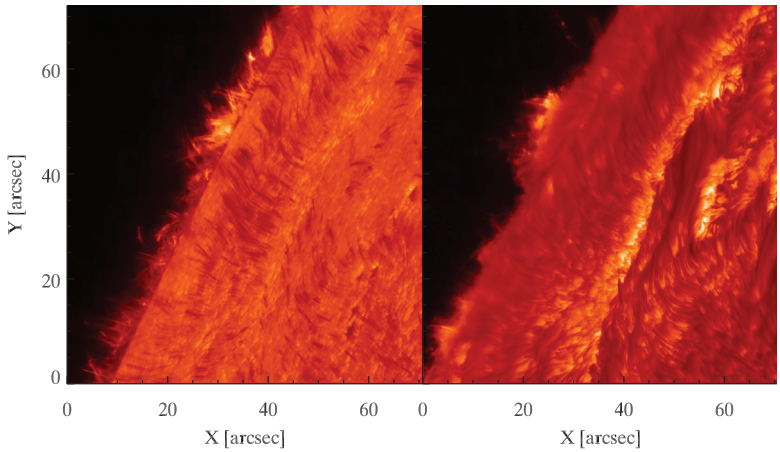

Figure 1.4: The chromosphere seen at the limb in the Hα spectral line from the Swedish 1-m Solar Telescope. The left image is taken from the blue wing of the Hα line with a Doppler offset of 41 km s^{-1} and, hence, only display chromospheric features with a net Doppler shift towards us (the observer), otherwise we see the photosphere. The right image is from the line centre where the chromosphere at the limb resembles a diffuse "blanket" due to the superposition of spicules.

Going outwards from the photosphere the density of the plasma goes down rapidly, and even though the pressure of the plasma and magnetic field both decrease, at a height of approximately 1500 km above the photosphere, the magnetic pressure overtakes the gas pressure (red line in Fig. 1.5). This is roughly in the middle of the chromosphere, which stretches for roughly 2500 km between the atmosphere's temperature minimum, at the top of the photosphere, and the transition region (see Fig. 1.2). When the magnetic pressure is larger than the gas pressure, the plasma is in a "frozen in" condition and has to follow the magnetic field, which is expanding into and filling the chromosphere, thus creating a highly dynamical and chaotic

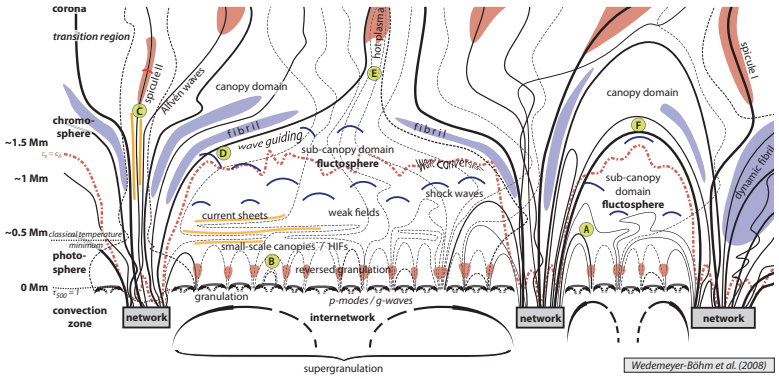

Figure 1.5: Schematic of a 2D cut through the atmospheric layers (from Wedemeyer-Böhm et al. 2009) with convective flows beneath the photosphere and magnetic field lines stretching from the convective zone to the corona. Deeper rooted magnetic fields in the network regions are drawn in thick solid lines, the weaker internetwork fields in thin dashed lines. A theoretical surface showing where the magnetic field pressure overtakes the plasma pressure, also known as the β=1 surface, is marked by the red dotted line which on average lies just below 1.5 Mm. Above the β=1 surface, plasma concentrations follow the magnetic field lines and are shown as red and blue blobs. These are named fibrils, dynamic fibrils, hot plasma, and type I and II spicules. It should be noted that the generation of type II spicules is still poorly understood and that the exact location of these spicules in a representation like this is still under intense investigation and debate.

atmospheric layer (Priest 1982). Here we can see a complex combination of structures such as fibrils, jets, swirls, and blobs on the disc, while the limb is dominated by spicules (see Fig. 1.4 and 1.7) (Rutten 2007; Wedemeyer-Böhm et al. 2012; Vissers & Rouppe van der Voort 2012; Tsiropoula et al. 2012).

The chromosphere is also known as the interface layer between the solar surface and the hot corona as the temperature increase of the solar atmosphere starts here. Because the plasma density of the chromosphere is much higher than in the corona, roughly 10 times as much energy is required to perform the heating from approximately 5000 K up to 10000–20000 K in the chromosphere than the rise from 10000 K to 1 million K in the corona.

In the continuum and most of the spectral lines in the visual part of the spectrum, the chromosphere is optically thin. There are only a handful of spectral diagnostics that have sufficient opacity in the chromosphere and

therefore can be used to probe the conditions in this part of the atmosphere (see Fig. 1.2). In particular the Hα and Ca II 8542 lines are interesting as they are the only ones that can be observed with traditional telescopes from the ground. In addition, they form in the middle of the chromosphere where the magnetic pressure is dominant and they both cover a wide range of heights while being offset with respect to each other, hence, probing slightly different layers while retaining an overlap region. The different formation heights of spectral lines is a useful tool when analysing dynamic events as it provides an opportunity to trace events as they move through different heights and temperatures of the solar atmosphere.

Looking at the chromosphere as it is seen on the limb in Hα in Fig. 1.4, second panel, it is a thick undistinguishable haze with structures becoming more visible towards disc centre. Protruding from the haze at the limb we find the tops of spicules as the only clear chromospheric feature, whereas these spicules are not observed on the disc as they can no longer be separated from the rest of the chromosphere. In stead, the disc is filled with a myriad of features, such as fibrils, swirls, and blobs, which interact and complicates the understanding and description of this atmospheric layer. Since the fundamental processes on the Sun takes place on very small spatial and temporal scales, the observations of the small scale features seen in disc observations complements the features visible on the limb and creates a strong basis for the investigation of the chromosphere.

1.1.3 Transition Region & Corona

In Fig. 1.2, the top of the chromosphere has a temperature of roughly 10000 K, while just 100–200 km further out it has increased to 1–2 million K in the corona (above the range of the figure). This is the outermost atmospheric layer of the Sun and it stretches out into the solar system for millions of kilometres (Carroll & Ostlie 2006). The incredibly high temperature of the corona compared to the photosphere (and chromosphere) is equivalent to the hypothetical situation of having a heater in the middle of a room at 20 degrees while the walls of the room reach 1000 degrees when the only source of heating in that room is the heater (so no energy from outside the room). This is the source of one of the largest mysteries still remaining in solar physics and is known as the coronal heating problem (see e.g. Zirker 1993). An important part of the answer might be found by studying the transition region, which hosts the entire temperature increase. The transition region is a thin atmospheric layer only a few hundred kilometres thick wedged between the chromosphere and the corona. As the transition region has a near constant thickness and has to follow the top of the chromosphere, it really is just a transition from the chromosphere to the corona. Most likely, the solution to the coronal heating problem will come from simultaneous studies of the photosphere, chromosphere, transi-

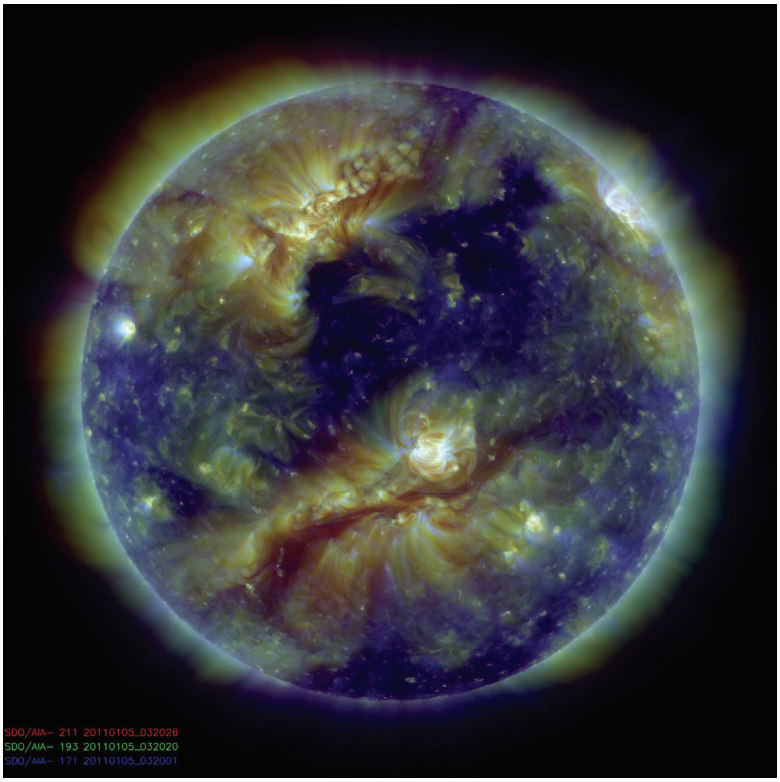

Figure 1.6: The corona seen in three different spectral lines (211 Å - 2 million K in red, 193 Å - 1.3 million K in green, 171 Å - 600 000 K in blue) with NASA's SDO/AIA instrument. The dark regions at the poles and centre of the Sun are coronal holes, while the long dark structure in the south between two of the coronal holes is a large filament. In the bright active regions, several coronal loops can be seen connecting magnetic islands of opposite polarity.

tion region, and corona. This would enable us to see which events on the surface and in the lower atmosphere trigger the rise in temperature, seen in the transition region, and reveal which mechanisms are responsible for transporting the energy required to heat the corona. This task is not trivial as the extreme temperatures of the transition region and corona, unlike the chromosphere, is responsible for emitting mainly UV and X-ray radiation which are mostly blocked by the Earth's atmosphere. Hence, observations

of these regions requires telescopes in space which are expensive and limited in the amount of tasks they can perform.

When observed in X-rays, the corona is usually characterised by the coronal loops (Bray et al. 2006) going between regions of opposite magnetic activity. These loops connect to magnetic islands in the photosphere which lie on the edge of larger active regions and usually appear in systems which can last for several solar rotations, whereas a single loop within the system only lasts for about one day (Priest 1982). Other striking features in the corona are the X-ray bright points (Harvey 1996) which typically are 22000 km wide and evenly distributed over the solar disc. They are the coronal signs of tiny bipolar regions in the photosphere and approximately 1500 of them appear every day and live for 8 hours on average. Other features appear at coronal heights but contain material that is more similar to chromospheric plasma, such as prominences (Hirayama 1985) at the limb, which are know as filaments (Martin 1998) on disc (see Fig. 1.6). These are the most stable and longest lived features seen on the solar surface with lifetimes up to 200 days (Priest 1982). In addition to these features the corona is usually seen to have some larger dark patches on the disc and mainly around the poles, called coronal holes, which appear in the corona as colder and less dense regions than the average (see Fig. 1.6).

1.2 Quiet Sun, Active Regions & Coronal Holes

The solar surface is usually divided into different regions based on the magnetic field configuration in the photosphere and atmosphere. In regions where the magnetic field concentration in the photosphere is low with a myriad of mixed polarity fields, the chromosphere displays, as a result of this, a complicated magnetic geometry with a great deal of horizontal field lines and closed loops which is typical for quiet Sun conditions. Where the magnetic field is more unipolar and dominated by vertical field lines on the other hand, are strikingly visible in coronal spectral lines and known as coronal holes. During the Skylab period, consisting of three manned missions between 1973-1974, the average amount of coronal hole on the Sun at any give time was measured and found to be around 20% of the total solar surface. Of these 20%, 3/4 were located in polar regions whereas the remaining quarter were observed elsewhere on the disc (Priest 1982). The final solar region is the active regions. These appear where large amounts of magnetic flux from beneath the photosphere emerges, forming bright points everywhere, and, instead of vanishing within a day, continues to grow into an active region. Hence, in the photosphere, active regions look like large concentrations of bright points, called plage, which are split into regions of opposite polarity when examined in magnetograms. Living alongside the bright points in an active region it is common to find several pores and

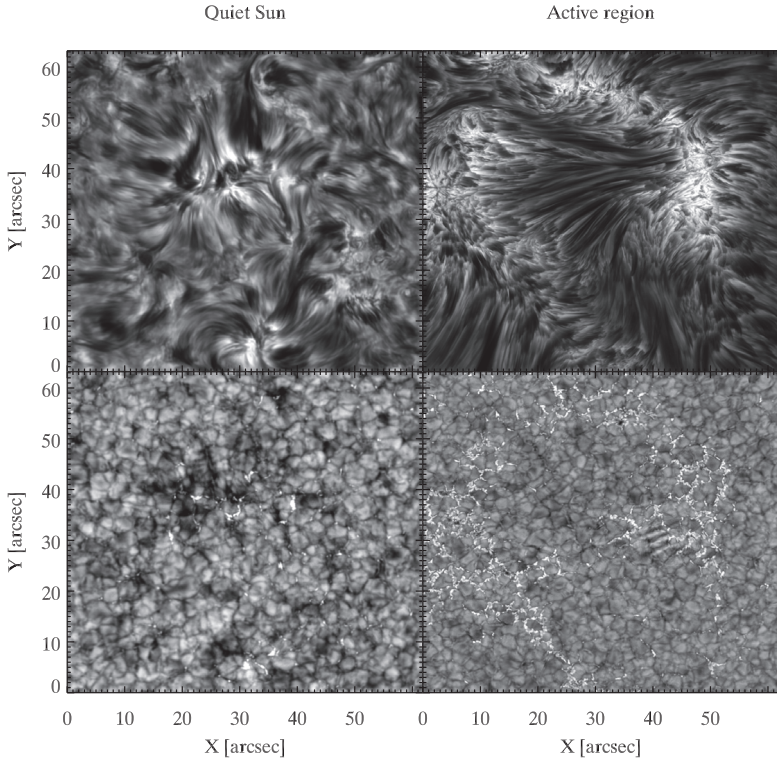

Figure 1.7: The chromosphere and photosphere in quiet Sun and active region conditions as seen in Hα on 2011 May 05 and 2008 June 14, respectively. The quiet Sun photosphere displays a small collection of bright points in the centre resulting in a clear rosette being visible in the chromosphere. The active region is full of bright points which are ordered in two clear groups of opposite polarity resulting in long fibrils in the chromosphere connecting the two concentrations.

sometimes even sunspots. Going to the chromosphere, an active region can be recognised by long fibrils following the magnetic flux loops, which expand out into the corona, connecting the opposite polarity regions (Priest 1982). In total, no more than 5–10% of the solar surface is normally considered an active region, which, when combined with the average area covered by coronal holes, leaves 70–80% of the solar surface constantly displaying quiet Sun conditions. These numbers are, to some extent, time dependant as the

Sun is displaying an 11 year magnetic activity cycle in which the number of sunspots observed on the solar surface increases drastically. Close to the solar maximum, when the sunspot number peaks, the average area of active regions increase while the polar coronal holes, which are among the longest lived solar features, disappear completely.

Chapter 2

Observing the Sun

2.1 Ground vs. Space

Observations of the Sun are mainly done from either the ground or space (there have been some balloon experiments, e.g. Barthol et al. 2011) and both have advantages and disadvantages. The advantages for one can often be disadvantages for the other, or just impossible to do in one of the two locations. For instance, the costs for ground-based telescopes are not negligible, but they are far lower than the cost of sending a solar telescope outside the Earths atmosphere, and becomes a huge advantage for ground-based observations. On the other side, UV and X-ray radiation can only be observed from space and, hence, becomes an advantage for space-based observations mainly because these spectral lines are impossible to observe from the ground. The largest solar telescope in space has an aperture with a diameter of 0.5 m, the SOT instrument aboard the Hinode spacecraft (Kosugi et al. 2007), while the largest ground-based solar telescope, the New Solar Telescope (NST) at the Big Bear Solar Observatory (Cao et al. 2010), has a diameter of 1.6 m. This means that another win for ground-based observations is the size of the telescopes as well as the ease of maintaining and improving them, which is impossible with space telescopes (with a notable exception being the Hubble Space Telescope). In addition to this comes the visibility of the Sun, where space-based telescopes have an advantage as there are no obstructions, such as clouds, between them and the Sun and orbits can be chosen such that the day/night cycle on Earth is not an issue, meaning that continuous observations can be made. Measures can be met by ground-based telescopes to reduce the advantage of no obstructions that space telescopes have, but no ground-based telescope can do continuous observations of the Sun due to the day/night cycle. A final difference between space and ground-based observatories is the amount of data that can be stored. Ground-based observatories are only limited by the amount of storage they are able to acquire while space-based observatories are limited by

the bandwidth of the connection with storage facilities on the ground. This results in a limited field of view or/and a limited cadence of the observations.

The importance of observing very small and rapid events on the Sun in order to understand the fundamental processes in the solar atmosphere fuels the need for ground-based observatories such as the Swedish Solar Telescope and NST, as these are able to resolve small spatial scales and can have a very fast cadence.

2.1.1 Seeing

After taking into account every easily observed obstruction of the Sun, such as clouds, haze, pollution, and dust, there is still a remaining factor which space telescopes do not have a problem with, called "seeing". Seeing is the combined term for anything that degrades the quality of the images through disturbances in the Earths atmosphere. The effect of seeing is easily seen with the naked eye on a hot summers day when the air just above the ground seems to quiver as it gets heated by the hotter surface and begins to rise. When sunlight passes through air that is full of turbulent motions it is distorted and the images from a solar telescope can become blurry to the point where the entire image looks like a grey indistinguishable background. There are also other atmospheric disturbances higher up which can come from e.g. shearing winds in different layers going in opposite directions causing turbulence, but they do not distort the images as much as the hot air close to the ground. With a little luck, sunlight can pass through most of the atmosphere with little or no disturbance from the higher levels of the atmosphere.

The ways of reducing the effects of seeing is by carefully selecting the location of the telescope, carefully design the telescope (paint white, high tower, free wind exposure, etc.), using additional instruments within the telescope that can correct for the atmospheric disturbance, and post-processing of the images. In the last two methods, the seeing effects are decomposed into a series of polynomials which are constructed such that most of the seeing power is in the lower modes.

2.2 The Swedish Solar Telescope

Placed on top of a 2500 m high mountain on the Canary island, La Palma, the Swedish 1 m Solar Telescope is located in an almost ideal area for a solar telescope. The SST sees few clouds, long sunny days and a lot of wind which can blow away the rising heat from the surface, which is also covered in small bushes that reduce the heating significantly. In addition, the telescope is a 17 m high tower, which puts the entrance of the telescope above most of the hot air from the ground. One drawback with La Palma as a location is the proximity of the Sahara desert which deposits huge amounts of sand

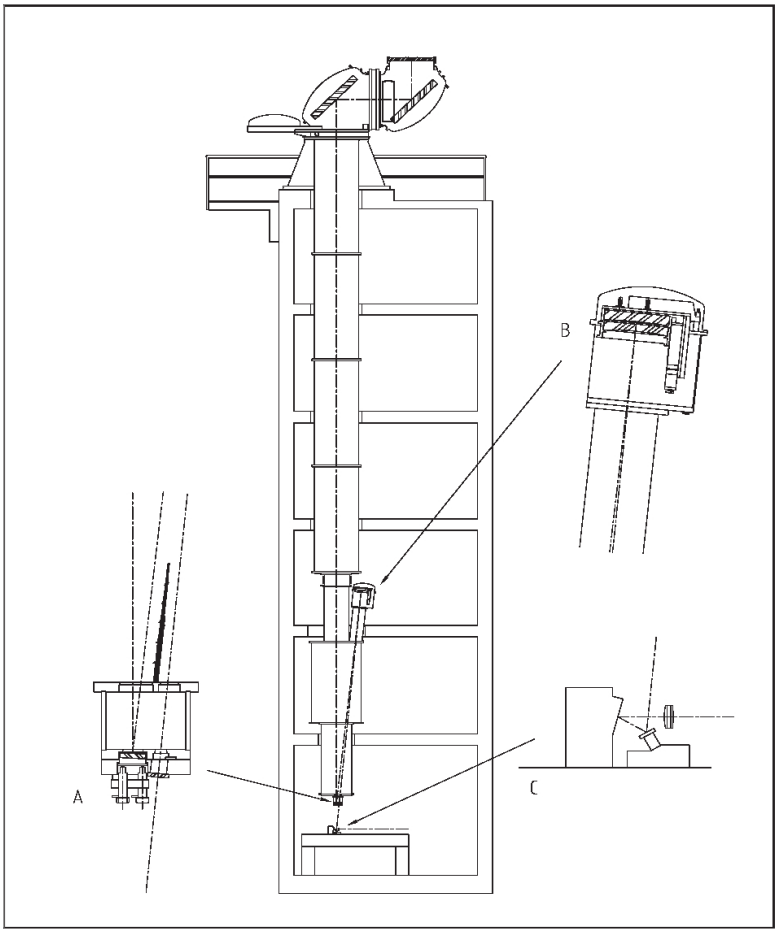

Figure 2.1: Technical specification of the Swedish 1-m Solar Telescope (Scharmer et al. 2003a). a) The box holding the field mirror and primary focus. b) The Schupman corrector. c) The AO and the tip-tilt mirror.

dust high into the air through the wind, and when the wind is blowing from the south-east on La Palma, a haze of dust can cover the entire island. On the other hand, when the wind is coming from the west and north, it is usually in the form of trade winds which cross the entire Atlantic ocean, undisturbed, and can result in excellent seeing conditions.

The telescope has an inner vacuum tube which avoids the internal turbu-

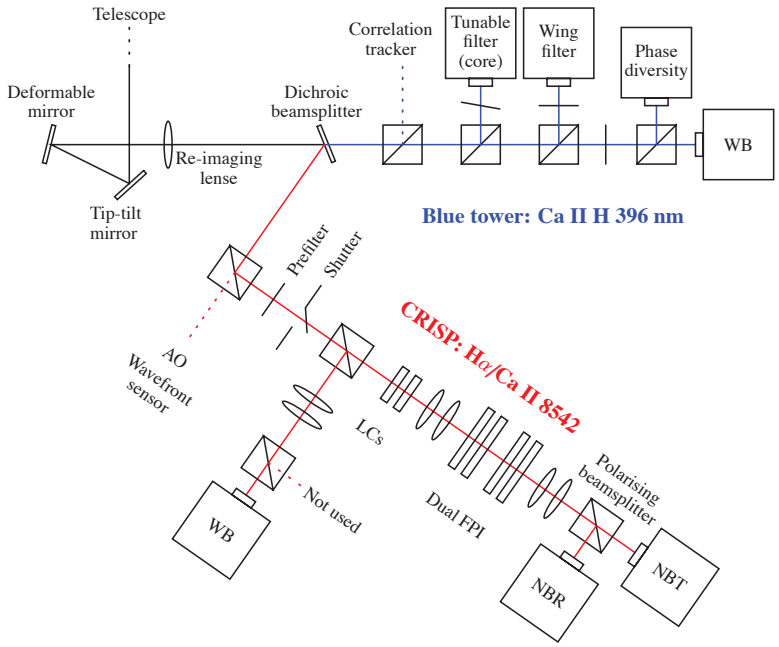

Figure 2.2: The optical table at the SST with both the blue tower and CRISP. Explanation for abbreviated parts of CRISP: wideband camera (WB), narrowband cameras (NBT, NBR), liquid-crystal polarisers (LCs). Figure adapted from Mats Löfdahl.

lence and the first optical component of the telescope is the vacuum window which has to be polished to high optical quality. Because of the thickness needed by the vacuum window to withstand the pressure difference between the vacuum and air, there is a probable upper limit to high quality polished optical vacuum windows of just over 1 m. To reduce the number of optical surfaces, which adds to the deformation of the wavefront through irregularities, inhomogeneities, etc., and increase photon efficiency, the vacuum window on SST is a refractor lens instead of a flat window (Scharmer et al. 2003a). Sunlight passes through the vacuum tube and hits a mirror at the bottom which reflects the light up to a Schupman corrector. Because different wavelengths in the light beam are focused at different distances from the lens due to chromatic aberrations, the Schupman corrector is required to put the different wavelengths together at a single focus before reflecting the light beam to the primary focus. Just after the primary focus and first on

the optical table lies a tip-tilt mirror, along with a deformable mirror and a re-imaging lens, on a rotatable plate, which can be used to switch between the two main observing modes at the SST: high resolution slit spectroscopy with the TRIPPEL spectrograph or imaging spectroscopy with the CRisp Imaging SpectroPolarimeter (CRISP) and other imaging channels. The tip-tilt mirror corrects for the tip and tilt modes of the wavefront deformation by seeing before the light beam reaches the deformable mirror of the Adaptive Optics system (AO) which also consists of a wavefront sensor located further along on the optical table. First, the wavefront sensor observes and measures the positions of the solar fine structure as seen through many small parts of the telescope aperture. When the Earths atmosphere disturbs the solar image, the image moves differently in the different parts of the aperture and the measured difference in the images can be translated to a deformable mirror which then changes into the shape that compensates for the distortions. Because the atmosphere changes very quickly, the AO system has to deform the mirror more than 1000 times per second with a very high accuracy each time (Scharmer et al. 2003b).

Further along on the optical table (see Fig. 2.2) a series of beam splitters divides the light between different cameras. To reduce the loss of photons for the cameras, a dichroic beamsplitter is used to send the blue part of the light beam to the blue tower with four cameras, while the red part is sent to the CRISP instrument (Scharmer et al. 2008). At the front of the CRISP instrument sits a pre-filter and a chopper that synchronises the images for the three cameras at the back of CRISP, while the core of CRISP consist of a dual Fabry-Pérot interferometer (FPI) and two fast-response liquid-crystal polarisers. The second etalon has a wider passband than the first, effectively selecting only one of the periodic narrower passbands from the first etalon. In combination with an even broader pre-filter, only one transmission peak is left from the periodic passband of the first etalon. When it comes to the two liquid crystals, the combination of their states allows CRISP to also perform full Stokes polarimetry. The fast wavelength tuning of the FPI in CRISP allows for a change between any two wavelength positions allowed by the pre-filter in less than 50 ms. These high speed capabilities of CRISP makes it uniquely ideal for studies of fast-moving and short-lived chromospheric dynamics using imaging spectroscopy, where the images cover an area of about 60×60 arcsec, or 44000 km$\times$44000 km (the diameter of Earth is 12500 km).

Located at the back of CRISP are three high-speed low-noise CCD cameras operating at a frame rate of 35 frames per second with an exposure time of 17 ms. Two of the cameras are called narrowband cameras and are located behind the FPI, LCs, and a polarising beamsplitter. This beamsplitter allows the narrowband cameras to measure orthogonal polarisation states simultaneously, enabling the removal of the cross-talk between measured states due to seeing. The third camera, the wideband camera, is

located in a branch of the beam that is split off before the FPI, but after the pre-filter, and is used as an anchor channel for the image processing. The transmission passbands for the CRISP pre-filters are so large (4.9 Å in Hα) that this channel also serves as photospheric reference.

2.3 Image Restoration

Many of the systems in today's ground-based telescopes are designed to reduce the effect of seeing down to a minimum. But even in space telescopes, where seeing is not an issue, the observations are not ready for use without some processing of the images. In common for all observations is the need to apply standard operations of flat fielding and dark current correction to obtain a clean solar image. In the case of the solar space telescopes, the images after flat fielding and and dark current corrections are the finished result, but ground-based observatories still have seeing effects to account for that the optical systems, however excellent they may be, were not able to remove entirely. For this part of the processing there are several methods, Speckle Imaging (SI), Phase Diversity (PD), and Multi-Frame Blind Deconvolution (MFBD), and the preference of one over the other is usually down to the setup of the telescope that performed the observation. In common, however, is that they all assume that the blurring resulting from seeing can be described as a convolution of the real image and a (space invariant) point spread function (Löfdahl et al. 2007).

In the Speckle imaging method, estimates of the amplitude and phase of an object act as a basis for a reconstruction of the complex Fourier transform of that object. In order to get an estimate of the amplitude one needs an estimate of the magnitude of the atmospheric seeing, which can be acquired from a statistical sample of the seeing (typically 100 frames) (Löfdahl et al. 2007).

If an unknown image is convolved with an unknown point spread function and noise, the problem is to determine both unknowns in a blind deconvolution. Because several combinations of object and point spread function can give a particular observed image, constraints are needed to find a more unique correct solution. One good constraint is the use of multiple frames which will allow for a determination of the separation between the common object in all frames and the point spread function. Further improvements to this can be made by also using multiple objects, which are images at different wavelengths displaying different solar scenes (photosphere, chromosphere, etc.), within the frames to determine the separation. This approach is employed by the Multi-Object Multi-Frame Blind Deconvolution method (MOMFBD). By introducing a second camera which records defocused images simultaneously with the main camera, one can use the phase diversity technique to further improve on the constraints for a unique solution in the

MOMFBD method (Löfdahl et al. 2007; van Noort et al. 2005).

Due to the chromospheric sound speed, $\sim$7 km s^{-1}, and the resolution of 0.″1 from a 1 m solar telescope, an object seen with the SST will only remain unchanged for 5 seconds (or less) given that this is the time it takes for plasma traveling at the chromospheric sound speed to travel half a 0.″1 resolution element. In most cases this gives Speckle just enough time to gather its 100 frames which it needs for a good restoration of the images. However, in this work we look at features which display apparent velocities of 30-110 km s^{-1} at the limb which requires observations with a cadence that is impossible to achieve with Speckle. MOMFBD on the other hand, which could only use 5-8 frames for a successful restoration, does not suffer from the high chromospheric sound speed and can also be made to have a cadence of $\frac{1}{4}$ second, which is sufficient even for very rapid events, while Speckle is stuck at a minimum cadence of 2-3 seconds due to the much larger statistical sample needed. Another difference between the two processing methods is the processing time, which for Speckle scales linearly with the number of frames used for the reduction while MOMFBD is based on an iterative, non-linear model fitting, and therefore scales badly with the number of frames per time interval. A few years ago, the severe computational demands of MOMFBD was considered to be a serious disadvantage while for Speckle affordable systems existed that could do the processing close to realtime. The MOMFBD processing is, however, gaining speed rapidly with the enormous advances in computing power that has been made in the last decades, making a semi-realtime reduction with MOMFBD a realistic prospect with a large modern computer cluster (Löfdahl et al. 2007).

Chapter 3

Spicules

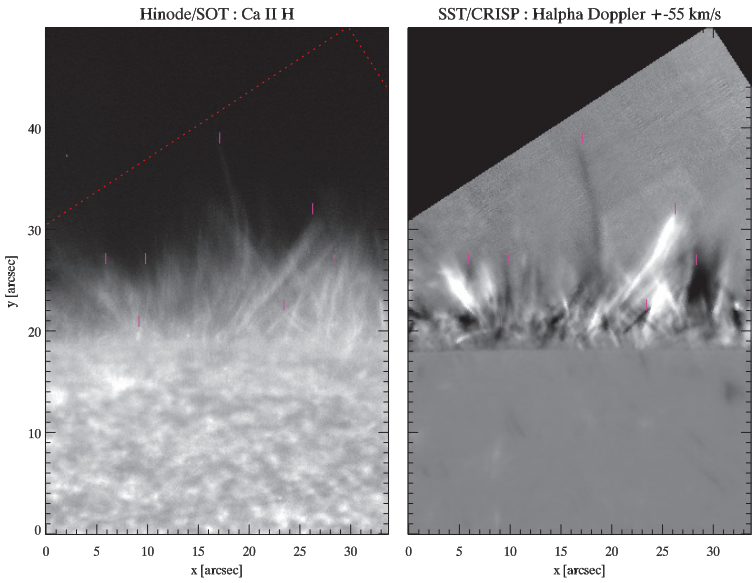

Figure 3.1: Coronal hole at the South Pole observed from space by Hinode (left) and from the ground by SST (right). Spicules are seen as straw-like features protruding from the limb at varying directions. Small pink markers guide the eye to identify spicules observed both in Ca H intensity and Hα at high Doppler shift. The superposition of spicules is clear from still images like these and even more so in time-lapse movies which show a bewildering level of dynamics.

In 1877, Pietro Angelo Secchi became the first man to describe and hand draw jet-like features protruding from the solar limb (Secchi 1877) and in 1945 these events were finally named spicules (Roberts 1945). Over the decades that followed some of the physical details of spicules were determined, such as: they extend to heights of 5000–10000 km above the photosphere before they fall back down during a lifetime of 5–10 minutes and display upward propagation speeds of 20–50 km s^{-1} (for extensive reviews see Beckers 1968; Suematsu et al. 1995; Sterling 2000; Tsiropoula et al. 2012). But progress on the understanding of their nature was relatively modest until the launch of the Hinode satellite. With the launch of the Hinode satellite in 2006, solar physicists received an unprecedented view of the solar limb with the high temporal and spatial resolution resulting from SOT's 0.5 m aperture situated in a seeing-free environment. This resulted in the discovery of a second type of spicule in 2007, living alongside the classical type I spicule, which only displayed upwards propagation before they vanished from the field of view (De Pontieu et al. 2007b). During their short lifetimes of 20-160 seconds, these new so-called type II spicules reach heights between 1.5-11.5 Mm and displayed apparent velocities from 30 km s^{-1} to 110 km s^{-1}(Pereira et al. 2012).

Since the discovery of type II spicules there have been growing speculations about their role in the heating of the corona (De Pontieu et al. 2007c, 2009; McIntosh et al. 2011). Type II spicules are characterised by an apparent fading along the entire length within a short time period and only displaying apparent upward propagation. Because of this, it has been theorised that type II spicules are heated as they accelerate outwards from their footpoint causing them to heat out of the passband of Ca H, Ca II 8542 and Hα diagnostics (De Pontieu et al. 2007b, 2011). These claims have also been further supported by signals appearing in transition region and coronal lines, with much higher temperatures, moments after the disappearance of a chromospheric type II spicule, without an observed succeeding downfall (De Pontieu et al. 2011). If type II spicules are indeed heated as they move outwards and they reach coronal heights, the major unanswered question is how much hot plasma and energy are they able to transport to coronal heights and how much of this stays in the corona. There have been studies showing that the total mass flux of spicules is two orders of magnitude larger than the mass flux needed to maintain the solar wind. Hence, if only 1% of the material in type II spicules is heated to coronal temperatures it could have a major impact on the solar wind flux and/or quiet Sun coronal heating (Beckers 1972).

So far the spicule picture is quite straight forward, as long as they are treated as jets, where some event in or below the chromosphere ejects plasma upwards towards the transition region and corona. In the case of the classical type I spicule, the initial event has been limited to magneto-acoustic waves expanding and retreating, causing these spicules to take non ballistic paths,

i.e. not caused by gravity (De Pontieu et al. 2007b). The picture, however, is not so well established in the type II spicule case where the best educated guess for a trigger is either a reconnection event or the emergence of magnetic flux (De Pontieu et al. 2007b; Sterling et al. 2010; Martínez-Sykora et al. 2011). In addition to not knowing with certainty what drives type II spicules, they do not behave simply as outwards propagating jets but also display significant sideways swaying motions which follows wave patterns. The most recent type II spicule study also revealed associated redshift alongside the "normal" blueshift which is expected in anything moving outwards and, hence, towards us. Since a redshift usually indicates something moving away from the observer, seeing strong redshifts in features with a clear outwards motion was puzzling. Through careful analysis of the mixture of red and blueshifts in type II spicules it was concluded that they are composed of three different types of motion, a field aligned flow, a sideways swaying motion, and a torsional motion around the spicule axis resulting in twisting and turning of type II spicules (De Pontieu et al. 2012). This could mean that previous measurements of type II spicules need to be revisited as not all three types of motion were taken into consideration. Others again claim that the number of type II spicules present on the Sun at any give time is far too low to heat coronal loops and consequently, that they do not play an important role in the temperature structure of the corona (Klimchuk 2012). There are also those suggesting that type II spicules are not jets propagating outwards from the chromosphere, but rather current sheets twisting and turning in and out of view (Judge et al. 2011).

The curvature of the solar surface means that when we observe the solar limb we are looking through a considerable amount of solar atmosphere from the side. In combination with the incredibly large number of spicules, both type I and II, present on the Sun at any given time, means that there is a significant overlapping of spicules when observed at the limb. This makes spicules at the limb notoriously difficult to separate and, hence, almost impossible to measure the spicule properties. In Fig. 3.1 the effect of superposition of spicules can be seen clearly as observed from the Hinode spacecraft and the SST and it does not take a lot of imagination to see the difficulties in separating the individual spicules. Figure 1.4 illustrates how a tangled mess of chromospheric features at the limb becomes much more separated chromospheric events when the viewing angle changes slightly towards disc centre and the chromosphere is seen more from above. In on-disc observations there is only a depth of 1000–2000 km of chromosphere to look through, which can be reduced significantly by observing separate and different spectral lines and line positions, making it much easier to measure individual features. The ability to pinpoint spicule properties and observe them in isolation will make a huge difference in the investigation of their nature and their importance for the solar atmosphere. In addition, the prospect of finding exact occurrence rates and full spectral samplings of

spicules can decide their role in the coronal heating debate. Since spicules prove to be very small thin events, close to the diffraction limit of today's telescopes, the use of the larger apertures of ground-based telescopes with AO systems can prove to be a vital step in spicule observations. In the end, a deeper understanding of the physics of spicules and the solar atmosphere is likely to come from detailed modelling, and the more constraints can be put on solar features, the easier it is for scientists to work towards a working atmospheric model.

3.1 Dynamic Fibrils

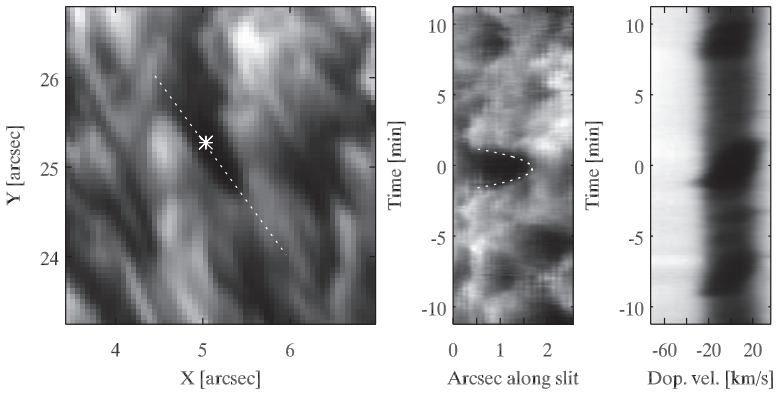

Figure 3.2: A close up of a dynamic fibril, moving towards the bottom right corner, seen in Hα along with its spacetime (xt) plot extracted along the dotted line, showing the parabolic path, and a λt-plot from the position marked with the asterisk, showing the change from blueshift to a redshift in DFs.

Going to the disc as it is observed in Ca II 8542 and Hα with the SST's CRISP instrument in Fig. 1.7, we can see lots of fibrillar structures and smaller jet-like dark features around the magnetic network (bright areas). These smaller fibrils seem to be rooted in the magnetic network and are seen to move away from it for a short while before ending their lifetime falling back towards their respective footpoints. Around 2006 these "Dynamic Fibrils", along with similar structures in quiet Sun called mottles, were linked to spicules at the limb and are now known as the on-disc counterpart to the type I spicule (Tsiropoula et al. 1993, 1994; Rouppe van der Voort et al. 2007; De Pontieu et al. 2007b; Langangen et al. 2008b). The dynamic fibrils found in on-disc active regions display typical lifetimes of 2-8 minutes,

reaching lengths of 500-2500 km, with maximum velocities ranging from 10-35 km s^{-1}, and a deceleration of 50-200 ms^{-1} (De Pontieu et al. 2007a). Figure 3.2 shows a dynamic fibril as seen in Hα on 2008 June 14, left, along with a spacetime plot, middle, taken along the dynamic fibril, showing the clear parabolic path taken by the top point of the DF, and a λt-plot, right, from the pixel marked in the left panel, showing the clear sudden blueshift of the DF along with the following redshift as it falls back down.

The deceleration of DFs is not equal to the gravitational deceleration of the Sun and, hence, they do not follow a ballistic path, even though it is parabolic (Hansteen et al. 2006). Through simulations that spanned from the upper convective zone to the lower corona, it was concluded that DFs and type I spicules are driven upwards by chromospheric shock waves which are generated by convective flows and global oscillations in the photosphere and convective zone (De Pontieu et al. 2007a).

3.2 Rapid Blueshifted Events

After the discovery of two types of spicules at the limb, it was realised that DFs and mottles could only be the disc counterpart of type I spicules. Less than a year later the first indications of what might be the disc counterpart to type II spicules emerged in the form of "Rapid Blueshifted Excursions" (RBEs) in Ca II 8542 observations from the Interferometric BIdimensional Spectrometer (IBIS) at the Dunn Solar Telescope (Langangen et al. 2008a). These were found, as the name suggests, in the blue wing of Ca II 8542 and looked like small dark streaks propagating rapidly outwards from the magnetic network within a short period of time and without a succeeding redshift indicating a down-flow (Rouppe van der Voort et al. 2009; Langangen et al. 2008a). Two years later, in 2009, both Ca II 8542 and Hα observations from the SST finally confirmed RBEs as the disc counterpart to type II spicules (Rouppe van der Voort et al. 2009). In blue wing images of Ca II 8542 and Hα, Fig. 3.3 bottom row, RBEs can be seen as dark streaks pointing radially outwards from the magnetic network, whereas, in the line centre images in the top row of Fig. 3.3, they are indistinguishable from the chromospheric plasma. Hence, the disc counterpart of type II spicules are much more elusive than dynamic fibrils or mottles.

Early studies of RBEs found them to reach lengths between 1-5 Mm within a lifetime of 10-120 seconds. During this time they displayed Doppler velocities ranging from 10 to 30 km s^{-1} in Ca II 8542 and 25-45 km s^{-1} in Hα and Doppler widths between 3-15 km s^{-1} and 8-20 km s^{-1} in Ca II 8542 and Hα, respectively (Rouppe van der Voort et al. 2009).

In the three papers presented in this thesis we firstly expand on the statistical sample of RBEs in both Ca II 8542 and Hα attempting to more accurately measure the physical properties of RBEs, as well as investigating

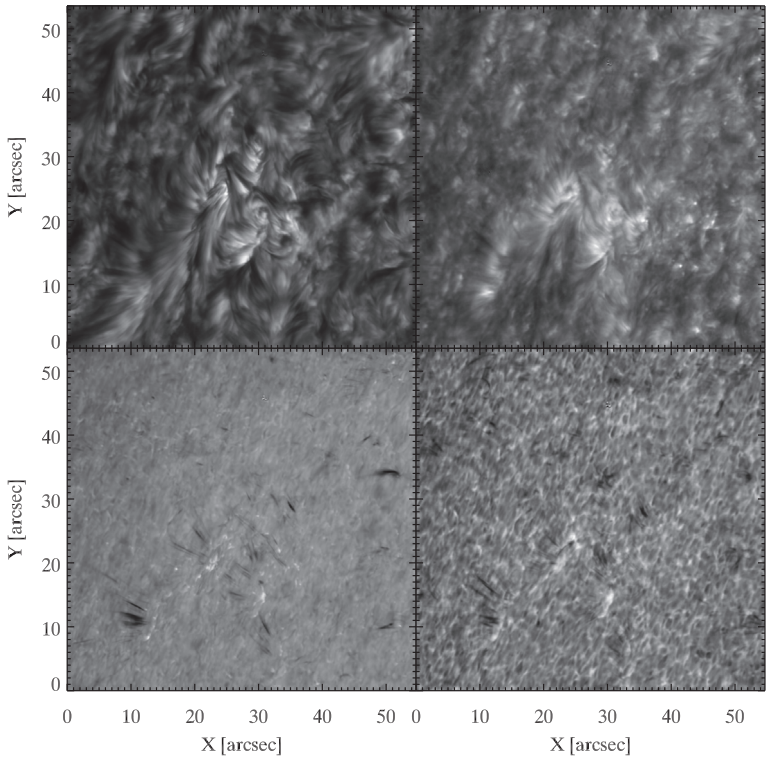

Figure 3.3: Hα and Ca II 8542 images from 2010 June 03 in the left and right column, respectively. Top row shows images from line centre while the bottom row shows a blue wing position commonly used for RBE detection with doppler shifts of 47 and 20 km s^{-1} for Hα and Ca II 8542, respectively. The target region is a coronal hole close to the north pole limb where a number of clear RBEs (dark streaks) can be seen in the wing images of both Hα and Ca II 8542.

the connection between RBEs observed in the two spectral lines through the use of simultaneous Ca II 8542 and Hα observations. Furthermore we attempt to describe the temporal evolution of RBEs and, by examining the on-disc occurrence rate, give more prominence to RBEs as a source for coronal heating. Finally, we search for the on-disc counterpart to the redshifted type II spicules seen on the limb in De Pontieu et al. (2012). Throughout these studies, the role of RBEs as the on-disc counterpart to type II spicules

is strengthened, and we provide modellers with more constraints to their simulations of type II spicules.

3.3 Outlook to Future Work

During our work with type II spicules and their on-disc counterparts we have discovered and firmly established several key characteristics. However, there is still work to be done. For instance, RBEs and RREs have not been investigated in active regions, which Pereira et al. (2012) found to be dominated by type I spicules. In addition, the exact nature of type II spicules is not yet firmly established, which is most likely a task best suited for large ground-based telescopes with the ability to do spectral line scans within short time periods. Adding the ability of Stokes diagnostics would enable to study the relation between magnetic fields and spicules. This would shed light on the mechanism that trigger type II spicules.

Furthermore, the pinpointing of the minimum lifetime of RBEs to five seconds gives future observers the opportunity to spend at least several seconds to build up a spectral sampling of the RBE without sacrificing too much of the details in the temporal evolution. This would be important in measuring the temporal evolution of the change in Doppler shift (e.g. from blueshifted to redshifted for the most extreme cases), and appears to be possible with present-day instrumentation. Finally, with today's space observatories and the possibility of aligning their observations with the high resolution observations from the ground, it is possible to trace the evolution of RBEs from their birth in Ca II 8542 through Hα and well into the transition region and corona, enabling a build up of statistics and expanding the work done by De Pontieu et al. (2011). Particularly exciting is the upcoming launch of the IRIS satellite (Wülser et al. 2012) which will open a new window on the interface layer between the chromosphere and corona. We may expect that the observations from IRIS, combined with e.g. Hα and Ca II 8542 observations from the ground, will provide more detailed measurements on the amount of hot plasma and energy that is carried from the lower chromosphere into the corona by type II spicules.

Chapter 4

Thesis overview

The papers in my thesis are built on the work by Rouppe van der Voort et al. (2009), employing a similar automated detection routine which has been modified to work on specialised datasets. This detection routine locates a large number of blue and redshifted events in constructed detection images with a high associated Doppler velocity.

4.1 Statistical Properties of the Disk Counterparts of Type II Spicules from Simultaneous Observations of RBEs in Ca II 8542 and Hα

In this paper we utilise observations optimised for simultaneous detection of RBEs in the Hα and Ca II 8542 spectral lines at high temporal cadence taken with CRISP at the SST.

We provide solid evidence that RBEs seen separately in Ca II 8542 and Hα are connected with the the Ca II 8542 RBEs lying closer to the magnetic network while the Hα RBEs are a continuation of the Ca II 8542 RBEs. Furthermore, the validity of RBEs as the on-disc counterpart to type II spicules has been questioned based on earlier detection numbers of RBEs by Rouppe van der Voort et al. (2009) which did not correspond to the high number of type II spicules observed at the limb. We found that the number of detected RBEs is strongly dependent on the associated Doppler velocity of the image used for detection. At low Doppler velocities the detection numbers of RBEs are indeed of the same order magnitude as expected from Hinode Ca H observations of limb spicules.

Because of the much higher number of RBEs detected in this study as compared to Rouppe van der Voort et al. (2009), we were able to improve on the statistics of RBEs, showing that their physical properties correspond well with measurements of type II spicules at the limb (including the extensive sample of Pereira et al. 2012). In addition, automated detection of the

transverse motion of a large sample of RBEs enabled us to determine that RBEs, just like type II spicules, undergo significant transverse displacement during their lifetimes. Finally, we interpret the intergranular jets discovered at Big Bear Solar Observatory (Goode et al. 2010) compatible with a subset of isolated RBEs that we find in our data.

4.2 On the Temporal Evolution of the Disk Counterpart of Type II Spicules in Quiet Sun

Here we describe RBEs seen in quiet Sun based on three different high quality datasets from CRISP at the SST. Our measurements of RBEs in a quiet Sun region deviates from the previously studied coronal hole RBEs (Rouppe van der Voort et al. 2009, Paper I) by displaying lower Doppler velocities and Doppler widths. In addition, there can be found no clear trend to the spatial dependance of Doppler velocities and widths along quiet Sun RBEs neither over the entire FOV nor in individual RBEs. These differences from coronal hole studies are attributed to the much more varying configuration of the magnetic field in quiet Sun.

One of the datasets analysed here had an extremely high cadence which allowed us improve greatly on the determination of lifetimes as well as the transverse motions of RBEs. At this extreme cadence, many RBEs displayed a clear sinusoidal wave pattern in their transverse motions with amplitudes and periods agreeing well with wave motion seen in spicules at the limb (Okamoto & De Pontieu 2011). This extreme cadence dataset also enabled us to investigate the appearance of RBEs over their full length within a few seconds, first reported by Judge et al. (2012). We interpret this sudden appearance as the result of the interplay of three kinds of motion reported in type II spicules by De Pontieu et al. (2012).

Furthermore, we examine the temporal connection between the Ca II 8542 and Hα RBEs which were found to connect spatially in Paper I. In addition to being located closer to the footpoint, Ca II 8542 RBEs are found to appear before the Hα RBEs, supporting the idea that progressive heating occurs in spicules and adding more weight to the prominence of type II spicules as a source for heating and mass loading of the corona. Finally, the high cadence and absence of line-of-sight confusion in our data allowed us to measure the recurrence rate of RBEs. This measurement is an important constraint for modelling coronal heating by spicules.

4.3 Interplay of Three Kinds of Motion in the Disk Counterpart of Type II Spicules: Up-flow, Transversal and Torsional Motions

This paper is an extension of the work done by De Pontieu et al. (2012), who demonstrated that dynamics of spicules at the limb is dominated by three kinds of motion: up-flow, transversal, and torsional motions. We investigate signs of these kinetic modes in the disc counterpart of type II spicules. De Pontieu et al. (2012) reported the appearance of both blueshifted and redshifted spicules of similar morphology right next to each other, at and close to the limb. Here we report the existence of Rapid Redshifted Excursions (RREs) all over the solar disc. These rapid redshifted events are seen and investigated in an extensive set of observations from different seasons. We find that RREs occur in the same regions as RBEs and have similar lengths, lifetimes, and average Doppler velocities. The average Doppler width, however, was found to be slightly lower for RREs than for RBEs. These results indicate that RREs are a manifestation of the same physical phenomena as RBEs and that there are motions in spicules than can give a net redshift when observed on the disc. Our results on RREs strengthen the interpretation that the dynamics of spicules is governed by three kinds of motions.

The relative importance of field aligned flows in spicules can be deduced from the imbalance in the abundances of RBEs and RREs. The fact that the RRE/RBE detection count ratio is found to be less imbalanced towards the limb indicates that field-aligned up-flows are a significant contributor to the net Doppler shift of spicules. Furthermore, torsional motions are deduced from touching RRE-RBE pairs lying in parallel which we interpret as a sign that many spicules have varying Doppler shifts across their widths. Finally, it should be mentioned that most RBEs and RREs are observed in isolation which fits very well with the idea that transversal swaying is the third kinetic mode in spicules.

Bibliography

Barthol, P., Gandorfer, A., Solanki, S. K., et al. 2011, Sol. Phys., 268, 1

Beckers, J. M. 1968, Sol. Phys., 3, 367

Beckers, J. M. 1972, ARAA, 10, 73

Berger, T. E., Rouppe van der Voort, L. H. M., Löfdahl, M. G., et al. 2004, A&A, 428, 613

Bray, R. J., Cram, L. E., Durrant, C., & Loughhead, R. E. 2006, Plasma Loops in the Solar Corona

Cao, W., Gorceix, N., Coulter, R., et al. 2010, Astronomische Nachrichten, 331, 636

Carroll, B. W. & Ostlie, D. A. 2006, An introduction to modern astrophysics and cosmology

De Pontieu, B., Carlsson, M., Rouppe van der Voort, L. H. M., et al. 2012, ApJl, 752, L12

De Pontieu, B., Hansteen, V. H., Rouppe van der Voort, L., van Noort, M., & Carlsson, M. 2007a, ApJ, 655, 624

De Pontieu, B., McIntosh, S., Hansteen, V. H., et al. 2007b, PASJ, 59, 655

De Pontieu, B., McIntosh, S. W., Carlsson, M., et al. 2011, Science, 331, 55

De Pontieu, B., McIntosh, S. W., Carlsson, M., et al. 2007c, Science, 318, 1574

De Pontieu, B., McIntosh, S. W., Hansteen, V. H., & Schrijver, C. J. 2009, ApJl, 701, L1

Foukal, P. V. 2004, Solar Astrophysics, 2nd, Revised Edition

Goode, P. R., Yurchyshyn, V., Cao, W., et al. 2010, ApJl, 714, L31

Hansteen, V. H., De Pontieu, B., Rouppe van der Voort, L., van Noort, M., & Carlsson, M. 2006, ApJl, 647, L73

Harvey, K. L. 1996, in Astronomical Society of the Pacific Conference Series, Vol. 111, Astronomical Society of the Pacific Conference Series, ed. R. D. Bentley & J. T. Mariska, 9–18

Hirayama, T. 1985, Sol. Phys., 100, 415

Judge, P. G., Reardon, K., & Cauzzi, G. 2012, ApJl, 755, L11

Judge, P. G., Tritschler, A., & Chye Low, B. 2011, ApJl, 730, L4

Klimchuk, J. A. 2012, Journal of Geophysical Research (Space Physics), 117, 12102

Kosugi, T., Matsuzaki, K., Sakao, T., et al. 2007, Sol. Phys., 243, 3

Langangen, Ø., De Pontieu, B., Carlsson, M., et al. 2008a, ApJ, 679, L167

Langangen, Ø., Rouppe van der Voort, L., & Lin, Y. 2008b, ApJ, 673, 1201

Löfdahl, M. G., van Noort, M. J., & Denker, C. 2007, in Modern solar facilities - advanced solar science, ed. F. Kneer, K. G. Puschmann, & A. D. Wittmann, 119

Martin, S. F. 1998, Sol. Phys., 182, 107

Martínez-Sykora, J., Hansteen, V., & Moreno-Insertis, F. 2011, ApJ, 736, 9

McIntosh, S. W., de Pontieu, B., Carlsson, M., et al. 2011, Nature, 475, 477

Okamoto, T. J. & De Pontieu, B. 2011, ApJl, 736, L24

Pereira, T. M. D., De Pontieu, B., & Carlsson, M. 2012, ApJ, 759, 18

Priest, E. R. 1982, Solar magneto-hydrodynamics (D. Reidel Publishing Company)

Roberts, W. O. 1945, ApJ, 101, 136

Rouppe van der Voort, L., Leenaarts, J., de Pontieu, B., Carlsson, M., & Vissers, G. 2009, ApJ, 705, 272

Rouppe van der Voort, L. H. M., De Pontieu, B., Hansteen, V. H., Carlsson, M., & van Noort, M. 2007, ApJ, 660, L169

Rutten, R. J. 2007, in Astronomical Society of the Pacific Conference Series, Vol. 368, The Physics of Chromospheric Plasmas, ed. P. Heinzel, I. Dorotovič, & R. J. Rutten, 27

Scharmer, G. B., Bjelksjo, K., Korhonen, T. K., Lindberg, B., & Petterson, B. 2003a, in Society of Photo-Optical Instrumentation Engineers (SPIE) Conference Series, Vol. 4853, Society of Photo-Optical Instrumentation Engineers (SPIE) Conference Series, ed. S. L. Keil & S. V. Avakyan, 341–350

Scharmer, G. B., Dettori, P. M., Lofdahl, M. G., & Shand, M. 2003b, in Society of Photo-Optical Instrumentation Engineers (SPIE) Conference Series, Vol. 4853, Society of Photo-Optical Instrumentation Engineers (SPIE) Conference Series, ed. S. L. Keil & S. V. Avakyan, 370–380

Scharmer, G. B., Narayan, G., Hillberg, T., et al. 2008, ApJ, 689, L69

Secchi, A. 1877, Le Soleil, Vol. 2 (Paris Gauthier-Villars)

Spruit, H. C. 1976, Sol. Phys., 50, 269

Spruit, H. C. 1977, Sol. Phys., 55, 3

Stein, R. F. & Nordlund, A. 1998, ApJ, 499, 914

Sterling, A. C. 2000, Sol. Phys., 196, 79

Sterling, A. C., Harra, L. K., & Moore, R. L. 2010, ApJ, 722, 1644

Suematsu, Y., Wang, H., & Zirin, H. 1995, ApJ, 450, 411

Tsiropoula, G., Alissandrakis, C. E., & Schmieder, B. 1993, A&A, 271, 574

Tsiropoula, G., Alissandrakis, C. E., & Schmieder, B. 1994, A&A, 290, 285

Tsiropoula, G., Tziotziou, K., Kontogiannis, I., et al. 2012, Space Sci. Rev., 65

van Noort, M., Rouppe van der Voort, L., & Löfdahl, M. G. 2005, Sol. Phys., 228, 191

Vernazza, J. E., Avrett, E. H., & Loeser, R. 1981, ApJS, 45, 635

Vissers, G. & Rouppe van der Voort, L. 2012, ApJ, 750, 22

Wedemeyer-Böhm, S., Lagg, A., & Nordlund, Å. 2009, Space Sci. Rev., 144, 317

Wedemeyer-Böhm, S., Scullion, E., Steiner, O., et al. 2012, Nature, 486, 505

Wülser, J.-P., Title, A. M., Lemen, J. R., et al. 2012, in Society of Photo-Optical Instrumentation Engineers (SPIE) Conference Series, Vol. 8443, Society of Photo-Optical Instrumentation Engineers (SPIE) Conference Series

Zirker, J. B. 1993, Sol. Phys., 148, 43

Part II

Articles

Paper I

Statistical Properties of the Disk Counterparts of Type II Spicules from Simultaneous Observations of RBEs in Ca II 8542 and Hα

Sekse, D.H., Rouppe van der Voort, L. and De Pontieu, B.

ApJ, 752, 108 (2012)

The Astrophysical Journal, 752:108 (14pp), 2012 June 20 doi:10.1088/0004-637X/752/2/108

STATISTICAL PROPERTIES OF THE DISK COUNTERPARTS OF TYPE II SPICULES FROM SIMULTANEOUS OBSERVATIONS OF RAPID BLUESHIFTED EXCURSIONS IN Ca II 8542 AND Hα

D. H. Sekse[1], L. Rouppe van der Voort[1], and B. De Pontieu[2]
[1] Institute of Theoretical Astrophysics, University of Oslo, P.O. Box 1029 Blindern, N-0315 Oslo, Norway
[2] Lockheed Martin Solar & Astrophysics Lab, Org. A021S, Bldg. 252, 3251 Hanover Street Palo Alto, CA 94304, USA
Received 2012 February 15; accepted 2012 April 12; published 2012 June 4

ABSTRACT

Spicules were recently found to exist as two different types when a new class of so-called type II spicules was discovered at the solar limb with the Solar Optical Telescope on board the *Hinode* spacecraft. These type II spicules have been linked with on-disk observations of rapid blueshifted excursions (RBEs) in the Hα and Ca II 8542 lines. Here we analyze observations optimized for the detection of RBEs in both Hα and Ca II 8542 lines simultaneously at a high temporal cadence taken with the Crisp Imaging Spectropolarimeter at the Swedish Solar Telescope on La Palma. In this study, we used a high-quality time sequence for RBEs at different blueshifts and employed an automated detection routine to detect a large number of RBEs in order to expand on the statistics of RBEs. We find that the number of detected RBEs is strongly dependent on the associated Doppler velocity of the images on which the search is performed. Automatic detection of RBEs at lower velocities increases the estimated number of RBEs to the same order of magnitude expected from limb spicules. This shows that RBEs and type II spicules are indeed exponents of the same phenomenon. Furthermore, we provide solid evidence that Ca II 8542 RBEs are connected to Hα RBEs and are located closer to the network regions with the Hα RBEs being a continuation of the Ca II 8542 RBEs. Our results show that RBEs have an average lifetime of 83.9 s when observed in both spectral lines and that the Doppler velocities of RBEs range from 10 to 25 km s^{-1} in Ca II 8542 and 30 to 50 km s^{-1} in Hα. In addition, we automatically determine the transverse motion of a much larger sample of RBEs than previous studies, and find that, just like type II spicules, RBEs undergo significant transverse motions of the order of 5–10 km s^{-1}. Finally, we find that the intergranular jets discovered at Big Bear Solar Observatory are a subset of RBEs.

Key words: Sun: atmosphere – Sun: chromosphere – Sun: corona

1. INTRODUCTION

Observing the chromosphere at the solar limb, a great number of thin jet-like features called spicules can be seen protruding outward from the limb. While spicules have been known and studied for a long time (for an extensive overview, see Beckers 1968; Sterling 2000), progress in understanding their nature has been relatively modest. However, interest in this phenomenon has revived considerably in recent years. The seeing-free environment and aperture of sufficient size for high spatial resolution allowed the *Hinode* satellite to provide an unprecedented view of the solar limb in the form of high temporal resolution, long-duration time series of Ca II H filtergrams. From these observations, a new class of spicules was discovered (De Pontieu et al. 2007) that is characterized by short lifetimes (typically 10–100 s), vigorous dynamics, and exclusively upward motion (50–150 km s^{-1}). Their nature is quite different from what are now considered as classical spicules, or type I spicules, which have lifetimes from 5 to 10 minutes and display clear rise and downfall phases at more modest velocities (20–30 km s^{-1}). The characteristic sideways swaying motion that this newly identified class (or type II spicules) displays has been regarded as a sign that the chromosphere is permeated with Alfvénic waves of sufficient energy to accelerate the solar wind and potentially heat the quiet corona (De Pontieu et al. 2007). Later studies have further strengthened the conjecture that type II spicules have an important role in mass loading and heating of the corona (De Pontieu et al. 2009, 2011)

The driving mechanism behind type I spicules seems to be well understood. Type I spicules have been identified as the off-limb manifestation of what is known as dynamic fibrils in active regions on the disk. The observations and modeling of De Pontieu et al. (2004), Hansteen et al. (2006), and De Pontieu et al. (2007) demonstrated that dynamic fibrils are driven by magnetoacoustic shocks that result from flows and waves that leak along magnetic field lines from the photosphere into the chromosphere. A similar mechanism is responsible for driving part of the quiet Sun mottles (Rouppe van der Voort et al. 2007), which helps explain why type I spicules can be detected in both active regions and the quiet Sun.

In contrast to type I spicules, the formation and driver of type II spicules is not well understood and is still under debate. Martínez-Sykora et al. (2011) describe in detail the formation of what resembles a type II spicule in their three-dimensional radiative magnetohydrodynamics simulation. The simulated jets show similarities to type II spicules in that rapid ejection of cool chromospheric plasma into the corona occurs while it is being heated to temperatures that are high enough to cause apparent fading in typical chromospheric diagnostics. In the simulation, small-scale flux emergence leads to chromospheric plasma being accelerated by a strong, mostly horizontal, Lorentz force into a region of a very strong vertical magnetic field. The subsequent increase in gas pressure induces the ejection of plasma into the low-density corona while being heated to coronal temperatures by heating processes at the footpoint.

While this scenario is tantalizing, further modeling is required in order to firmly establish the physics behind type II spicules. Perhaps more importantly, high-quality observations are essential in order to constrain the models and guide the direction of investigation. A complicating factor here is that due to their narrow spatial extents, short lifetimes, and significant displacement, as well as the superposition of many spicules along the line of sight, spicules are notoriously difficult to properly

measure at the limb. Finding the disk counterparts of type II spicules makes it possible to separate them spatially and overcome the problem of superposition encountered at the limb.

Langangen et al. (2008) investigated so-called "rapid blueshifted excursions" (RBEs) in on-disk Ca II 8542 data obtained with the Interferometric Bidimensional Spectrometer at the Dunn Solar Telescope. In their data, events with short-lived blueward asymmetries of the Ca II 8542 line were tentatively linked to type II spicules. Rouppe van der Voort et al. (2009, Paper I) used high-quality Hα and Ca II 8542 observations from the Crisp Imaging Spectropolarimeter (CRISP) at the Swedish Solar Telescope (SST) to make a firm connection between these RBEs and type II spicules. They found a large number of RBEs for which properties such as lengths, velocities, and lifetimes were found to agree well with what was measured for type II spicules. In addition, the appearance, including both swaying motions and apparent propagation away from magnetic field concentrations in the photosphere, was considered a clear indication that RBEs are the disk counterpart of type II spicules.

Recently, Judge et al. (2011) challenged the identification of RBEs as type II spicules by arguing that the global occurrence rate of RBEs as inferred from the Paper I measurements is too low. In this work, we further investigate the occurrence rate of RBEs in new high-quality CRISP observations as well as the observations used in Paper I. For the new observations, we employed a dual-line program that provides both spectrally well-sampled Ca II 8542 and Hα profiles at relatively high temporal cadence. This program allows for a direct comparison between RBEs measured in Ca II 8542 and Hα, a comparison that could only be done indirectly from the sequentially recorded data sets used in Paper I. Furthermore, we expand on previous results (from Paper I) by extending the automated detection routine for RBEs so that we can automatically determine lifetimes and transversal motion for a much larger statistical sample than in Paper I.

2. OBSERVATIONS AND DATA REDUCTION

The data was obtained from observations at SST (Scharmer et al. 2003a) on La Palma using the CRISP (Scharmer et al. 2008) instrument. CRISP is equipped with a dual Fabry–Pérot interferometer (FPI) system and three high-speed low-noise CCD cameras. These cameras operate at a frame rate of 35 frames per second with an exposure time of 17 ms per frame and are synchronized by an optical chopper. Two of the cameras are positioned behind the FPI and a polarizing beam splitter, while the third camera, which is used as an anchor channel for image processing, is positioned before the FPI but after the CRISP pre-filter and is referred to as the wideband channel. The field of view (FOV) with the CRISP instrument is roughly 61×61 arcsec with an image scale of $0\farcs0592$ pixel^{-1}. CRISP allows for fast wavelength tuning (<50 ms) between any two positions within a spectral region given by the spectral width of the pre-filter, which makes it ideal for studies of the dynamic time evolution of the chromosphere through imaging spectroscopy. Here we are interested in the Hα and Ca II 8542 spectral lines. For Hα, CRISP has a transmission FWHM of 66 mÅ and a pre-filter FWHM of 4.9 Å. For Ca II 8542, the transmission FWHM is 111 mÅ and pre-filter FWHM is 9.3 Å. High spatial resolution down to the telescope diffraction limit ($\lambda/D = 0\farcs14$ and $0\farcs18$ for Hα and Ca II 8542, respectively) is accomplished by the use of the SST adaptive optics system (Scharmer et al. 2003b) and the Multi-Object, Multi-Frame Blind Deconvolution image restoration technique (MOMFBD; van Noort et al. 2005).

A 38 minute data set obtained on 2010 June 27 (17:35–18:13 UT) has been analyzed. The target area was a coronal hole with a unipolar magnetic island, at solar coordinates $(x, y) \approx (-70'', 508'')$, ($\mu = 0.84$). Figure 1 gives an overview of the target region.

The observational program was made specifically for the detection of RBEs in Ca II 8542 and Hα, simultaneously, with a rather high cadence so that the time evolution of RBEs could be resolved properly. The pre-filter wheel limited the amount of dead time to 0.63 s when switching between the two lines. For the Ca II 8542 line, we ran a program with symmetric sampling at seven positions in each of the two wings, from ± 120 to ± 1452 with steps of 222 mÅ. In addition, we observed the line core and the blue wing at -600 mÅ with modulation of the liquid crystals with the purpose of obtaining photospheric magnetograms. For Hα we ran a program with dense sampling of 28 positions in the blue wing, from -300 mÅ to -2082 mÅ with steps of 66 mÅ. More detailed information on the sampling positions and their respective Doppler velocities can be seen in Figures 2(d) and (c), respectively. This program was based on our experiences from Paper I and specifically designed to simultaneously detect RBEs in both lines. RBEs are detected in Ca 8542 in Doppler maps constructed from the subtraction of symmetric positions from the line center, and in Hα in maps constructed from the subtraction of the far blue wing image from positions closer to the line center. The program is sufficiently fast (11.8 s cadence) to allow for temporal analysis of RBEs. The symmetric sampling of the Ca 8542 line allows for verification that the detected events are indeed asymmetric in the blue wing, which is the defining characteristic of RBEs.

We acquired 8 exposures per line position, which were used for MOMFBD image restoration (van Noort et al. 2005). Exposures from each spectral line were processed in separate MOMFBD restorations. Precise alignment between the wideband and narrowband cameras is achieved by a separate alignment procedure involving a reference pinhole array target. For the MOMFBD restoration of the sequentially recorded CRISP images, the wideband channel serves as a so-called anchor channel that ensures accurate alignment between the different line positions. For certain seeing conditions, the assumption of the size of the isoplanatic patch used to divide the FOV in subimages (here 128×128 pixels, or $7\farcs6$ squared) is not sufficiently accurate and the derived point-spread function (PSF) is not the optimal solution over the whole area of the subimage. This results in remaining rubber sheet deformations between the CRISP line positions in a single restoration. To reduce this effect, we employed an extra step in the processing following an idea from V.M.J. Henriques (2011, private communication). The wideband images are used twice in a restoration: (1) all images combined in the normal way resulting in a single restored "anchor" image and (2) separated in sets associated with the corresponding CRISP line positions resulting in one restored wideband image per CRISP line position. Even though individual wideband exposures enter twice in the restoration procedure, they are only used once for the determination of the PSF. For the use of the wideband images separated in sets per CRISP line position, the weight is put to zero for the wavefront sensing. The separately restored wideband images have the same rubber sheet deformations as the corresponding CRISP line positions, which can now be accurately measured by cross-correlation to the anchor wideband images. The deformation grid determined from the wideband images is then applied to the CRISP images, which results in precise alignment between the different line positions.

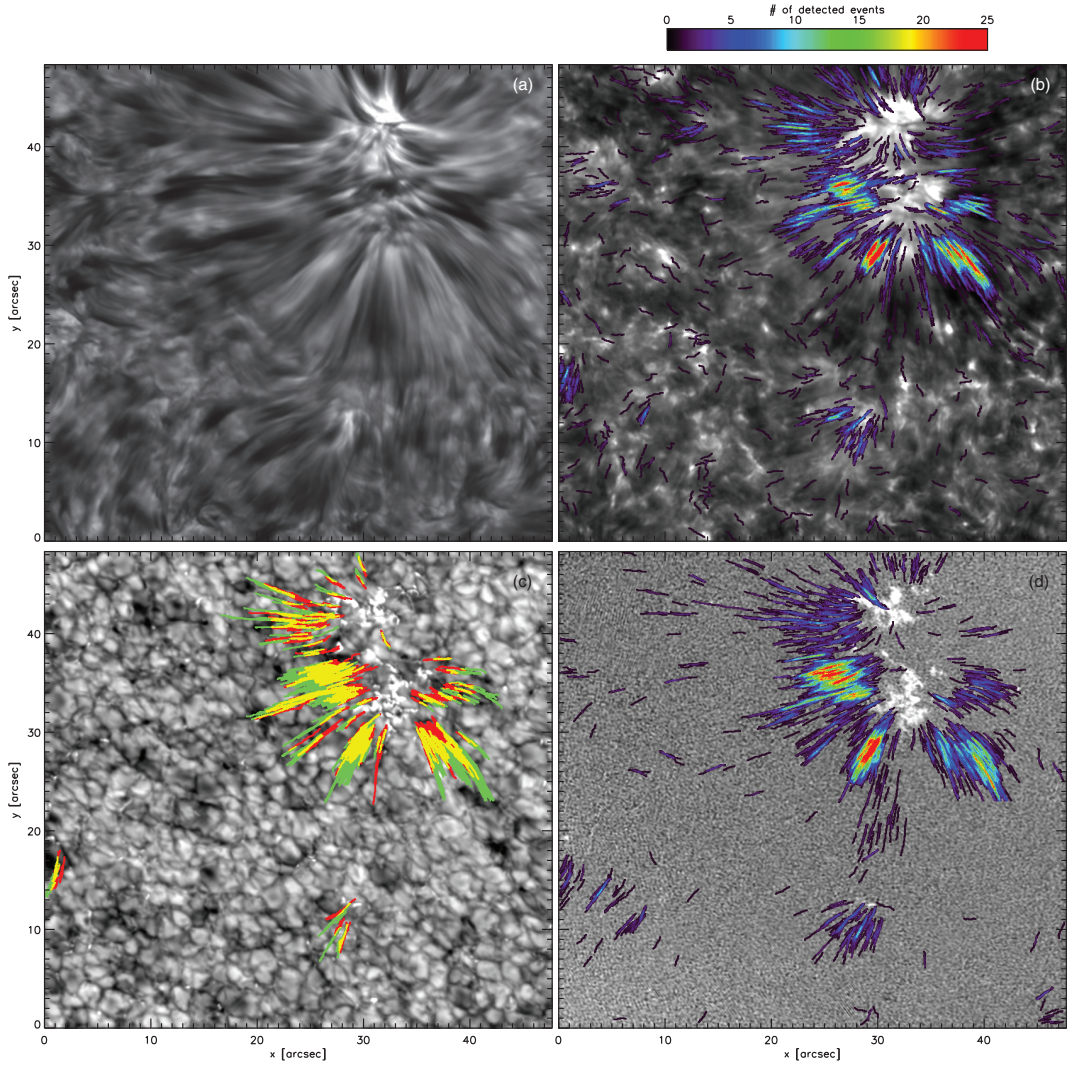

Figure 1. Overview of the observed target area. (a) Hα line core image. (b) Ca II 8542 line core image with overplotted in rainbow color scale a density map of identified RBEs detected at -20 km s^{-1} over the whole time series. (c) Hα wideband image (FWHM = 4.9 Å CRISP pre-filter) with overdrawn temporally resolved RBEs that are identified in both Ca II 8542 and Hα: the Ca II 8542 RBEs are drawn in red, the Hα RBEs are green, and the region where they overlap is yellow. (d) Ca II 8542 -600 mÅ Stokes V image in gray color scale with a density map overplotted of the number of identified RBEs detected in Hα at -45 km s^{-1} during the whole time series.

The data analyzed in this study benefited significantly from this extra step in the processing.

After the MOMFBD restoration the images from the individual line scans were combined to form a time series and the Ca II 8542 images in each scan were aligned with respect to the Hα images from the same time step. This alignment between the two lines was done using the wideband images which show photospheric scenes for both spectral lines so that the alignment is done with high accuracy. The images from both lines were then de-rotated to account for diurnal field rotation, aligned and de-stretched to remove warping due to seeing effects by determining local offsets on the wideband images and applying these to the CRISP images.

For the Ca II 8542 -600 mÅ magnetograms, all 32 exposures of the four different liquid crystal states were included in a single MOMFBD restoration, following the scheme described by van Noort & Rouppe van der Voort (2008) and Schnerr et al. (2011). For the polarimetric response of the telescope at 8542 Å, we used the model derived by de la Cruz Rodríguez (2010; also see de la Cruz Rodríguez & Socas-Navarro 2011). With the 17 ms exposure time, the effective acquisition time for the resulting Stokes V magnetogram is 544 ms. The noise

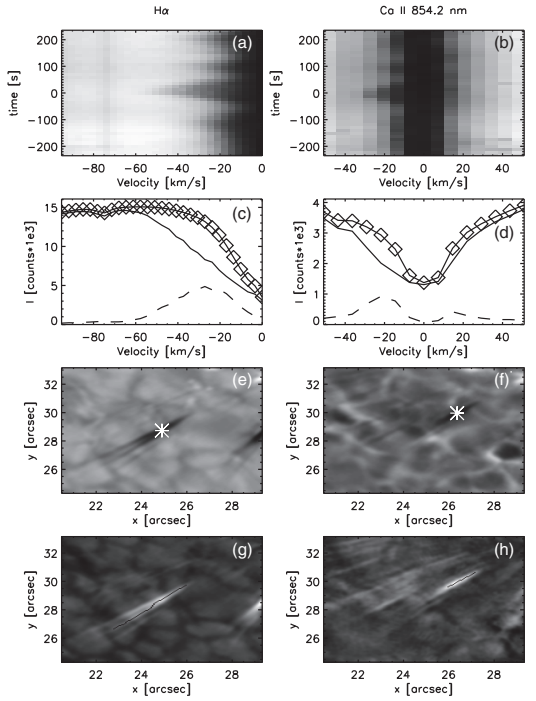

Figure 2. Details of an RBE observed in both Hα (left column) and Ca II 8542 (right column). Panels (a) and (b) show the temporal evolution of the spectrum at a central location in the RBE, marked with asterisks in panels (e) and (f) (note that this is not the same spatial location for the two spectral lines). The temporal axis is centered on the time used for the panels below. Panels (c) and (d) show the spectral profile at the asterisks' location with the solid line, the average spectrum over the full FOV with the solid line with diamonds at the sampling points, and the difference between these profiles is shown as the dashed line. Panels (d) and (e) show blue wing images at -45 km s^{-1} for Hα and -20 km s^{-1} for Ca II 8542. The RBE is seen as a dark streak which was seen to originate from the magnetically enhanced region in the upper right direction in the time steps before. The Ca II 8542 RBE is shorter and closer to this region than the Hα RBE. Panels (g) and (h) show the maps used for automated detection: a difference image in Hα with the -45 km s^{-1} image subtracted from the far wing -2 Å image, and a Ca II 8542 Doppler map at ± 20 km s^{-1}. The detection skeleton from the automated method is marked with a thin black line.

level is estimated at 0.14% of the continuum. It should be noted that at -600 mÅ, the Ca 8542 magnetogram is dominated by photospheric signals and is not affected by strong Doppler shifts. Strong Doppler shifts make single wavelength magnetograms closer to the line core, which are more chromospheric in nature, difficult to interpret. Furthermore, it should be noted that the Ca II 8542 line is less sensitive to polarization than for example more traditional diagnostics, like the Fe I 630 lines. In addition, the wavelength position used here, -600 mÅ, is relatively less sensitive to polarization than positions closer to the line core. All these factors combine to a rather limited diagnostic value of the magnetograms used in this study, in particular for the weak magnetic field environment of the coronal hole observed here: the strongest signals barely reach 1% polarization. Despite these limitations, the magnetograms serve as a reliable indicator of the position and polarity of the strongest magnetic field concentrations. These concentrations appear as photospheric bright points in continua and in the far wings of the spectral lines studied here.

We acquired another high-quality data set with the same observing program during the 2010 SST observing campaign: on 2010 July 3, we observed a coronal hole at $(x, y) \approx (19, 862)$ ($\mu = 0.41$) for 45 minutes. In this paper, we present results from the analysis of the 2010 June 27 data set but the 2010 July 3 data set is used as a reference to verify and check our results and conclusions.

3. METHOD

The data set was searched for RBEs in the Ca II 8542 and Hα lines separately, where they appear in the spectral wings as roundish or elongated dark absorption features against the photospheric background. An automated algorithm that locates RBEs by isolating the location and time of a long thin feature at high blueshifts was used to find a large number of RBEs in both data sets and both spectral lines in order to get reliable RBE statistics. Apart from some minor refinements, the method is identical to the method used for Paper I.

To make a clean detection of the upper chromospheric RBEs, the background, which often contains linear photospheric features (such as intergranular lanes), has to be reduced or removed from the images. For Ca II 8542 this is done by subtraction of the opposite wing position, thereby constructing a Doppler map, and for Hα this is done by subtracting the far blue wing image, at 2 Å, creating a difference image. To minimize the number of false detections, a lower limit for the length of blueshifted structures is set at ~725 km, 17 pixels, and any thin blueshifted feature with a length below this threshold is not counted. Like in Paper I, we find that this length threshold limits the probability of false detections significantly. A shorter length threshold allows small linear features in intergranular lanes to enter the sample, which upon further scrutiny do not display the typical spectral character of RBEs. The output of the automated algorithm contains every detected event in every time frame, and it also attempts to connect these single events over several time frames by making chains of events, which represents the time evolution of an RBE over several time steps. If an event from one time frame has 30% of its pixels within a 3 pixel distance from any pixel in an event from the next time frame, these two events are considered to be the same RBE observed at different stages in its time evolution. Because the lengths of events may vary greatly from frame to frame, the check has to be done in both temporal directions as the following event, which is supposed to link up with the current event, might be shorter than 30% of the current event's length. In this case, even if the following event lies completely on top of the current event, it would not be recognized as a valid link, while when performing the check "backward" there is a 100% overlap and the link is approved. This check is performed on all events in a time frame using all the events from the next time frame and also the frame after that, meaning that it allows for a jump in the chain of one time step, thus accounting for occasional moments of bad seeing. This automated method of connecting RBEs in time is an improvement compared to Paper I, where the lifetimes of RBEs were estimated manually by looking at a subset of 35 separate events and following their existence in following time steps.

Having the chains made automatically gives a large sample from which one can study the time evolution and produce accurate statistics of the typical lifetimes of RBEs. The cases where RBEs are connected in chains are also less likely to be false

detections, as it would take errors to occur very close together spatially and temporally. When it comes to the selection threshold for determining the temporal connection in chains, the threshold values were chosen based on trial and error. Allowing for events to be further away from one another introduces a significant number of wrong connections, particularly in the regions where the RBE detections are densest, and by constraining the percentage of pixels that has to be within the selected distance, too many good connections are disallowed. We found that the chosen parameters resulted in the most reliable statistics.

Once the chains are found, these can be used to get a measure of the transverse displacement and velocity. This is achieved by finding the average orientation of all events in a chain and determining its perpendicular direction. The transverse distance is then measured by taking the middle point of each event and projecting it onto the normal, which allows for both a measurement of the distance traversed transversally from one event to the next and also the velocity at which the RBE is moving transversally as we know the time difference between the two events. As explained above, there is an upper limit of 3 pixels on the spatial separation between RBEs in subsequent time frames. Combined with the cadence of 11.8 s, one would expect to have an upper limit for the transverse velocity of 11 km s^{-1}. However, this is not the case since the transversal displacement is measured from the RBE midpoints along the normal to the average direction of the RBE and this can give a larger separation than 3 pixels.

We have made extensive use of CRISPEX (Vissers & Rouppe van der Voort 2012) a widget-based analysis tool programmed in the Interactive Data Language (IDL) that allows for an efficient exploration of multi-dimensional data sets. With CRISPEX, the Hα and Ca II 8542 data sets can be examined at the same time and the tool was particularly useful for the verification of the RBE identifications from the automated detection method.

Figure 2 shows details of one RBE event, clearly identified in both Hα and Ca II 8542. Panels (e) and (f) show the RBE as dark streaks against a background of granulation in Hα and inverse granulation in Ca II 8542. For the spatial locations marked with asterisks, the spectral time evolution is shown in the top panels. This particular RBE displayed little sideways motion so that a single pixel location shows the actual spectral evolution of the RBE. These panels illustrate the defining characteristic of RBEs: a short-lived asymmetry in the blue wings of these strong absorption lines. The bottom panels show the maps used in the automated detection process: in Hα the disturbing background is attenuated by subtraction of the corresponding far blue wing image. Through this subtraction, the granulation intensity pattern is inverted so that intergranular lanes, narrow linear features, become bright. Our detection method is based on the negative of this difference images and searches for bright linear structures, removing the risk of intergranular lanes becoming false detection as these are now dark. In Ca II 8542, a Doppler map is used and RBEs are identified as bright linear structures against a low-contrast background. The detected structures are marked as thin black lines. Panels (c) and (d) show the detailed spectra at the time and location of the asterisks in panels (e) and (f) as solid lines. To separate the RBE spectral profile from the background profile, a reference spectrum constructed from averaging over the whole FOV is subtracted, resulting in the dashed profile. This RBE profile is clearly a blueshifted component separated from the background spectrum, a characteristic that is also apparent from its dynamical evolution, which appears to be unrelated to the chromospheric background seen closer to line center. The RBE profile is used to determine the Doppler velocity and Doppler width, following the method of Paper I. For this location in the RBE, the Hα Doppler velocity is 39 km s^{-1} and width 16 km s^{-1}, the Ca II 8542 Doppler velocity is 23 km s^{-1} and width 13 km s^{-1}.

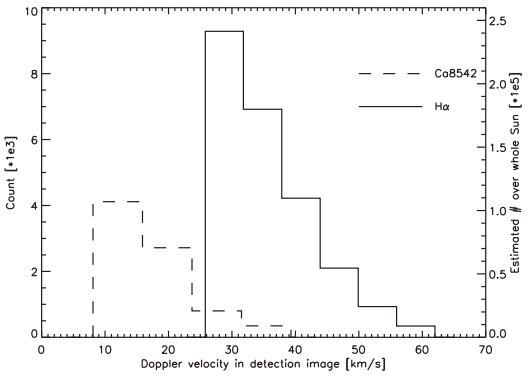

Figure 3. Histograms of the number of detected events as a function of the Doppler velocity used in the detection image. Hα detection numbers in solid lines, Ca II 8542 in dashed lines. The right axis scale indicates the estimated total number of events at any time over the whole surface of the Sun.

The length of an RBE was determined using the same method as Paper I: by first extending the detection skeleton (the thin black line in panels (g) and (h) outlining the detected event) by 20 pixels in both directions and dilation in width and then determining the points where either the Doppler velocity or Doppler width of the RBE profile is 0. This definition is equivalent to measuring the length for which a feature shows enhanced absorption compared to the average spectral profile. Hence, detected events have a possibility of becoming shorter than the minimum length threshold set by the detection routine since the measured Doppler width can become 0 even though there is signal in the detection map.

4. RESULTS

4.1. Number of RBE Detections

We found that the number of RBE detections varies significantly with the Doppler velocity from which the detection maps are constructed. Figure 3 shows histograms for the number of detected events as a function of the Doppler velocity in the detection map. For both spectral lines, we see a significant increase in the number of detected events for lower Doppler velocities. This trend is most pronounced for Hα, where we measure an increase from 341 at 63 km s^{-1} to 9285 events at 30 km s^{-1}. We manually verified a large subsample of the events detected at 30 km s^{-1} and we confirmed that almost all events are genuine RBEs. For Ca II 8542 we see a raise in the number of detected events from 346 at 35 km s^{-1} to 4116 at 12 km s^{-1}. Manual inspection at 12 km s^{-1}, however, revealed a high fraction of false identifications. We conclude that this line position cannot be trusted for the automated detection of RBEs. For the remainder of this paper, we present results from Ca II 8542 RBEs detected at 20 km s^{-1}, where we find the highest number of detections (2717 events). For Hα, we present results from RBEs detected at 45 km s^{-1} (2099 events), which gives a sample of similar size

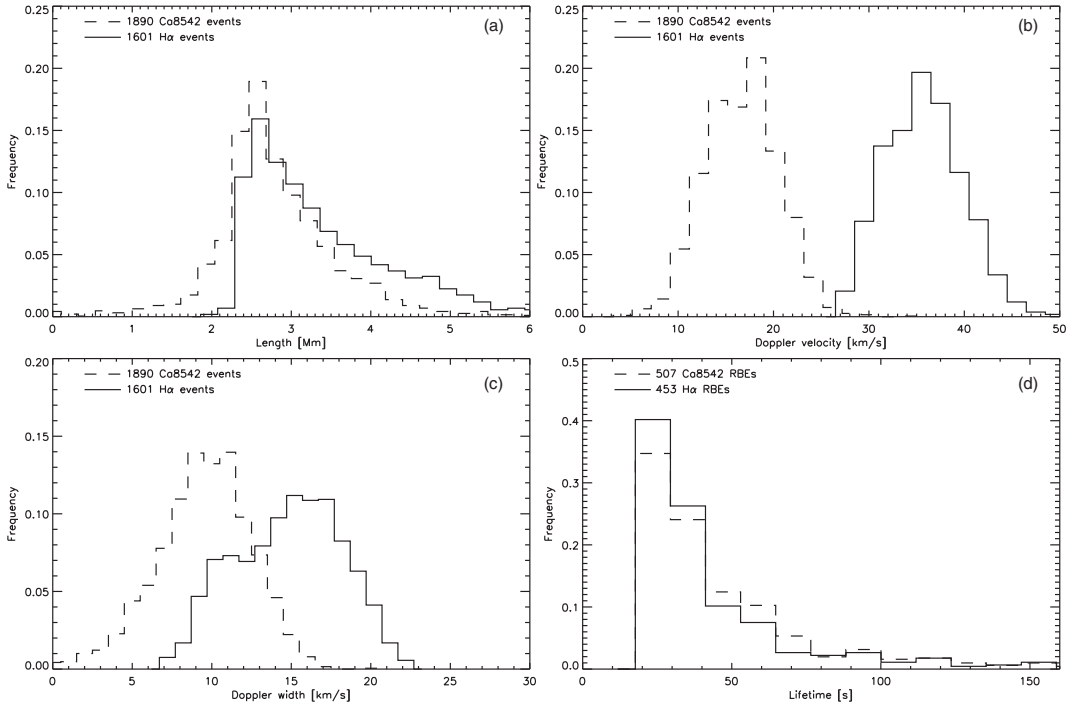

Figure 4. Histograms for (a) length, (b) Doppler velocity, (c) Doppler width, and (d) lifetime of RBEs that were identified for more than one time step. Solid lines are Hα RBEs; dashed lines are Ca II 8542 RBEs. The histograms for Doppler velocity and width are average measures for each time step in each event.

as for Ca II 8542. This choice is rather arbitrary since we regard all Doppler velocities reliable for RBE detection. We found it practical to have similar sample sizes for the two lines for the process of linking up the Hα and Ca II 8542 RBEs.

The right axis scaling of Figure 3 gives an estimate of the total number of RBEs at any time on the Sun. This estimate is derived from the average number of detections per time step extrapolated to the whole surface of the Sun.

4.2. Statistical Properties of RBEs

Figure 1(d) shows a density map of the spatial locations of the 2099 Hα RBEs detected at 45 km s^{-1} drawn on a Stokes *V* magnetogram. Most RBEs are found around the patch of unipolar magnetic field in the upper right part of the FOV, the region that is dominated by fibril structures in the line core images and bright points in the wideband image. There is another notable concentration of RBE detections below the center which is associated with a small concentration of enhanced Stokes *V* signal, and another smaller concentration to the left edge of the FOV. Besides these RBE concentrations there are a number of isolated RBEs scattered over the FOV that are not obviously associated with patches of Stokes *V* signal. As explained in Section 2, the diagnostic potential of the Ca II 8542 −600 mÅ magnetograms is rather limited and it is very conceivable that a more sensitive polarization diagnostic would reveal an association of the more isolated RBE signals with areas of enhanced polarization.

Of the 2099 Hα events, 498 were detected only in one time frame, while the rest linked up to other events in nearby time frames to create a total of 453 RBEs existing over several sequential time steps. We will call the events that could not be linked up with events in other time steps "single-frame RBEs," and the others "multi-frame RBEs."

The map of Ca II 8542 events (Figure 1(b)) shows a similar distribution of most RBEs being associated with the magnetic field concentrations and a number of events scattered over the FOV. Of the 2717 Ca II 8542 events, 827 were single-frame events, and the rest were linked up as 507 temporally resolved or multi-frame RBEs.

Most of the multi-frame and single-frame RBEs were located in regions with enhanced polarization signal, and of the isolated RBEs that lie scattered over the FOV, the majority are single-frame RBEs, as can be derived from Figures 1(b) and (d).

For each individual detected event the Doppler velocities and Doppler widths were calculated at each pixel in an event. The position of the pixels and time frame in which they were found used for a measure of lengths and lifetimes of the RBEs. Figures 4 and 5 display histograms of all the important properties of the 1890 and 1601 events that were found to make up 507 and 453 multi-frame RBEs in Ca II 8542 and Hα, respectively. The single-frame events are not included in this statistic as they lack time evolution, and thus cannot contribute to some of the histograms, such as transverse motions.

In panel (a) of Figure 4 the lengths of all events are shown for both Ca II 8542 and Hα. Typically, the Hα RBEs are found to have lengths of 2–6 Mm, with an average of 3.5 Mm, while the Ca II 8542 RBE lengths are seen to lie between 1.5 and 4.5 Mm with an average of 2.9 Mm. A few Ca II 8542 RBEs were found to have lengths shorter than the detection threshold of 725 km,

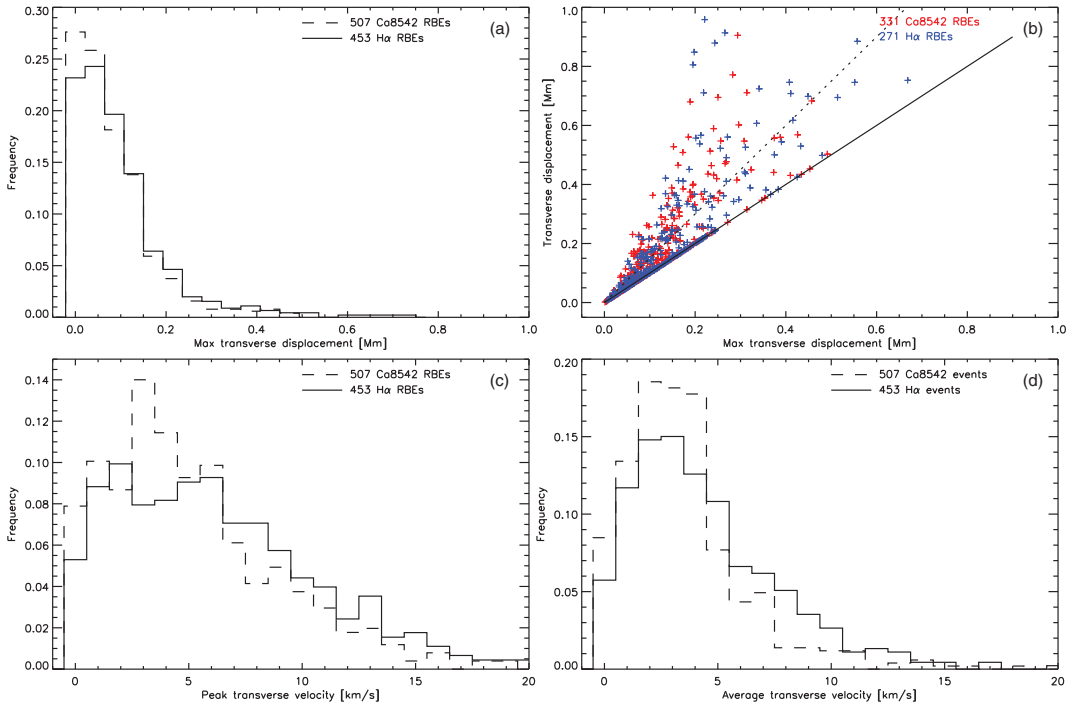

Figure 5. Histograms for measurements of the transverse motion of RBEs: (a) maximum transverse displacement or distance between the two most extreme positions during the lifetime of an RBE, (c) maximum transverse velocity of all measured velocities during the RBE lifetime, and (d) all measured transverse velocities over all time steps. The scatter plot in panel (b) shows the total transverse distance covered by an RBE during its lifetime against the maximum transverse displacement of (a). The solid line marks the line where the two measures are equal, and the dotted line marks where the total transverse displacement is 50% larger than the maximum transverse displacement.

which is possible since the method of measuring the RBE length is different from the RBE detection (see Section 3). No short Hα RBEs were found and we see a sharp lower cutoff at 2 Mm.

Panel (b) of Figure 4 shows the average Doppler velocity of all RBEs. The average RBE Doppler velocities lie between 10 and 25 km s^{-1} for Ca II 8542 and 30 and 50 km s^{-1} for Hα, with the mean value of the distribution of average Doppler velocities at 17.7 and 36.8 km s^{-1}, respectively. The maximum of all Doppler velocity measurements is as high as 50 km s^{-1} for Ca II 8542 and 62 km s^{-1} for Hα.

Panel (c) of Figure 4 shows the average Doppler width of all RBEs. As for the Doppler velocity, the Doppler widths are noticeably different in Ca II 8542 and Hα with averages of 10 km s^{-1} and 15.3 km s^{-1}, respectively, and the range going from 0 to 17 km s^{-1} in Ca II 8542, while Hα RBEs display Doppler widths from 7 to 23 km s^{-1}.

Panel (d) of Figure 4 shows the lifetimes of the RBEs. There is no major difference between the lifetime of Ca II 8542 and Hα RBEs and they both have lifetimes varying from 24 s up to 2.5 minutes. There were a few detections of very-long-lived RBEs with lifetimes of more than 3 minutes. They were all found in regions with a high density of RBEs and visual inspection exposed these events as falsely connected chains of several separate multi-frame RBEs.

Figure 5 show different measures of the transverse motion of RBEs. Panel (a) shows a histogram of the maximum transverse displacement, which is the distance between the two most extreme transverse positions of an RBE during its lifetime. All RBEs have some transverse displacement and several of the RBEs display transverse displacements of more than 400 km. The scatter plot in panel (b) shows the integrated transverse displacement, or the sum of the absolute values of each displacement during the RBE lifetime, against the maximum transverse displacement. The dotted line marks where the integrated transverse displacement is 50% larger than the maximum transverse displacement, the RBEs that lie above this line display considerable back-and-forth swaying motion during their lifetime. The RBEs that lie close to the solid line are mainly moving in one direction. Panel (c) shows the maximum transverse velocity for each RBE and panel (d) shows all measured transverse velocities. Transverse motions can be at velocities as high as 20 km s^{-1} although most events' velocities lie below 15 km s^{-1} with the bulk of the peak velocities around 5 km s^{-1}.

We observe many RBEs displaying back-and-forth sideways swaying motion during their lifetimes. For all of the RBEs that have a duration of more than two time steps, we measured how many times there is a change in direction. We found that for both Hα and Ca II 8542 RBEs, the change in direction happens an average of 1.7 times during their lifetime.

Figure 6 shows the variation of the Doppler velocity and Doppler width for RBEs along their length as color-coded lines

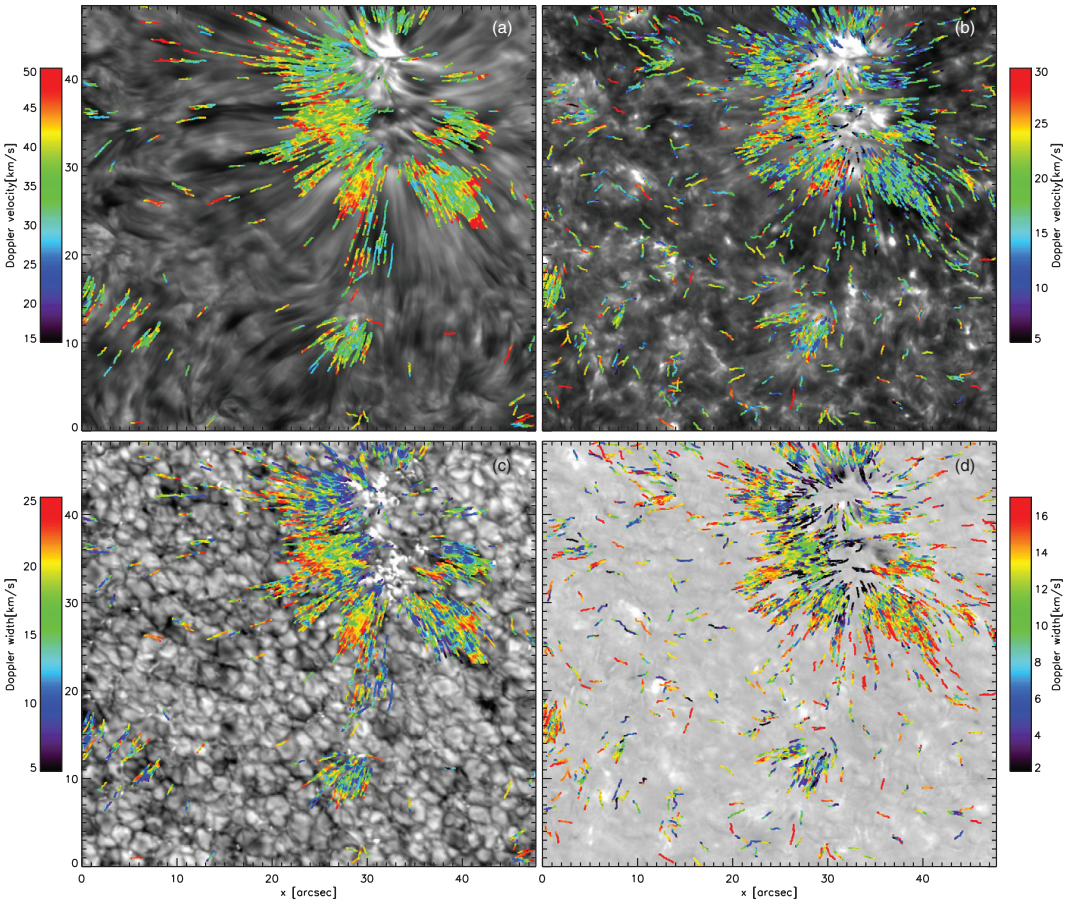

Figure 6. Doppler properties of RBEs as a function of their position in the FOV, Hα RBEs at left, Ca II 8542 RBEs at right. Color-coded Doppler velocities (top panels) and Doppler widths (bottom panels) drawn on background images of (a) Hα line center, (b) Ca II 8542 line center, (c) Hα wideband, and (d) Ca II 8542 -20 km s^{-1} detection map.

drawn at their spatial location in the FOV. All detected RBEs are drawn in successive order, with RBEs detected early in the time series drawn first so that they are covered by later RBEs that occur at the same spatial location. The RBE occurrence in the target area is dominated by the magnetic region, which gives a clear sense of the orientation of the RBEs and where they originate. This representation gives a clear visual impression of many RBEs increasing in both Doppler velocity and Doppler width toward their top. This trend is most clear for the Hα RBEs. It should be noted that despite the visual trend, there is a significant number of RBEs that have a more erratic variation of Doppler properties along their axis and even examples of decreasing trends.

There is a clear correlation between increased Doppler width for increasing Doppler velocity; this is illustrated in Figure 7.

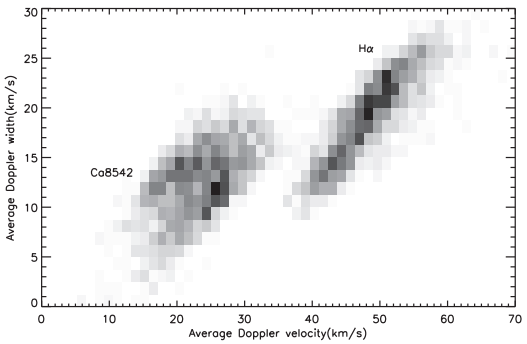

Figure 7. Scatter plot of average Doppler width vs. average Doppler velocity of all RBEs, represented as a two-dimensional density function. Darker regions represent the densest areas with data points.

4.3. The RBE Ca II 8542–Hα Connection

From the initial detection of 2717 and 2099 events in Ca II 8542 and Hα, respectively, a total of 1890 and 1601 events

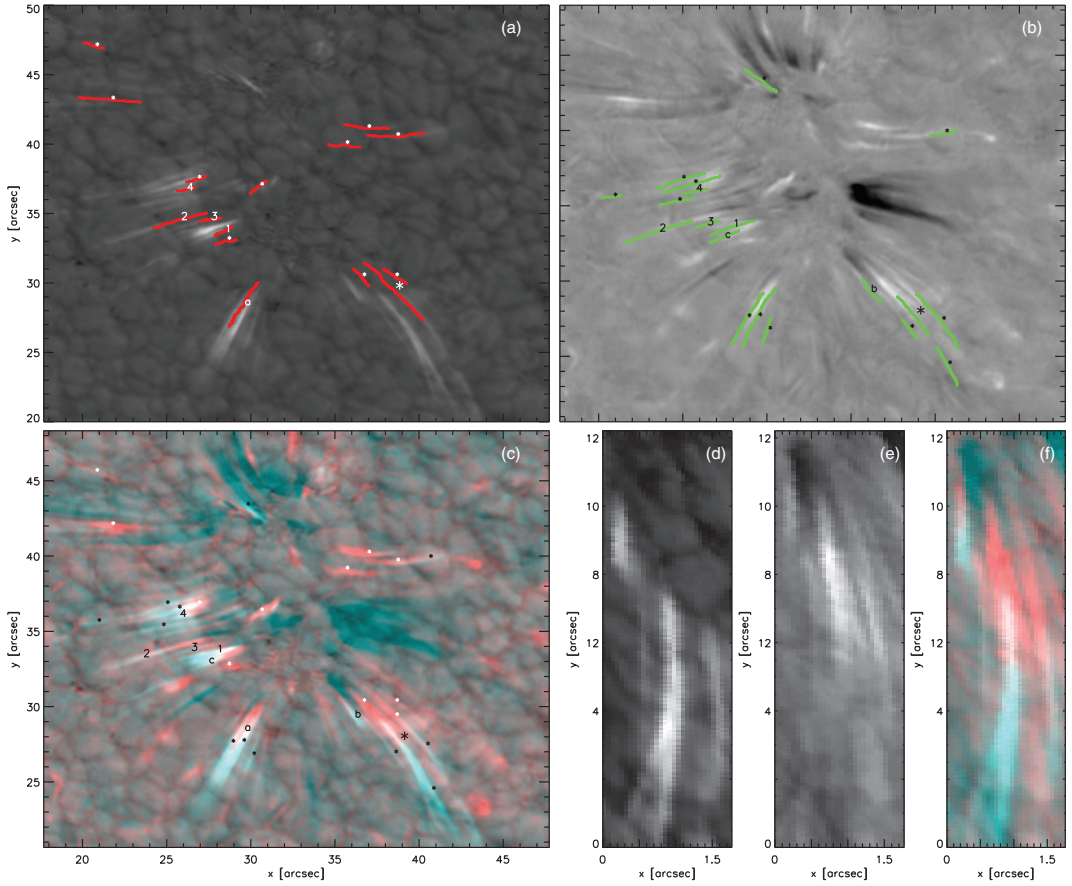

Figure 8. Examples of RBE detections. (a) Hα -45 km s^{-1} map used for RBE detection, RBEs are white. Red lines mark Ca II 8542 detections from the same time step. (b) Ca II 8542 -20 km s^{-1} detection map, RBEs are white. Green lines mark Hα detections from the same time step. (c) Composite image of the Hα and Ca II 8542 detection maps: the Ca II 8542 image filled the red channel, and the Hα image filled the blue and green channels of the true color RGB image. Detections marked 1–4 are RBEs connected in both Hα and Ca II 8542 for this time step, detections marked a–c are RBEs connected to the other spectral line in a different time step, and detections marked with stars are RBEs that are not identified in the other line. The three bottom right panels show a closer view of one RBE marked with a larger star at $(x, y) = (39, 28)$: (d) the Hα detection map, (e) the Ca II 8542 detection map, and (f) the Hα–Ca II 8542 composite image.

combined to form 507 and 453 multi-frame RBEs. These chains from both spectral lines were then compared to one another in order to see if there is a connection between the Ca II 8542 and Hα RBEs. The same method that was used for linking separate events to multi-frame RBE chains was employed to link the chains in the two spectral lines. The automated method managed to find about one-third of the multi-frame RBEs in both spectral lines simultaneously, resulting in 169 Ca II 8542–Hα RBE chains. Figure 1(c) shows the distribution of these 169 chains, drawn on a wideband image. The Hα parts of the chains are drawn as green lines, the Ca II 8542 parts as red lines, and the region where they overlap as yellow.

Our detection technique finds that a large fraction of the RBEs are detected and matched up in both lines, with a small fraction not matching up. However, from visual inspection of the data set, it becomes clear that for virtually all RBEs detected in one spectral line a corresponding RBE signature is observed in the other spectral line. This is illustrated in Figures 8(a) and (b), where close-ups of one time step are shown for both lines with the detected events in the other spectral line overplotted. The automated detection method managed to link seven RBEs in both spectral lines: four are found in both lines for this time step (marked as 1, 2, 3, and 4), one Ca II 8542 RBE is linked to an Hα RBE in another time step (marked "a"), and two Hα RBEs are linked to Ca II 8542 RBEs in another time step (marked "b" and "c"). The other detected RBEs were not flagged as connections (marked with small stars). Visual inspection, however, suggests a much higher connection rate which becomes even more apparent in the composite map in panel (c). Here, Hα and Ca II 8542 detection maps are combined in a color image where bright Hα features are blue-green, and bright Ca II 8542 Doppler features are red. Regions where these features overlap (i.e., overlapping RBEs) become white. This map suggests that all RBEs have signal in both Hα and Ca II 8542.

Panels (d)–(f) of Figure 8 offer a close-up centered on one of the longer RBEs. This long RBE was detected in both Hα and

Ca II 8542 (see panels (a) and (b)), but the automated method did not connect them. The images (and in particular the composite image) show that there is considerable overlap between the two lines. The other long but thinner RBE to the right is also detected in both lines but not flagged as connections—the composite image leaves no doubt that the two detections are of the same event. And the small RBE in the upper left was only detected for Hα for this time step (marked "b," connected to a Ca II 8542 detection in the next time step) but there is indeed RBE signal present also in Ca II 8542.

Figure 8 demonstrates that Ca II 8542 RBEs have their lower part closer to the magnetic regions, while Hα RBEs extend to larger distances away from these regions. This trend of Ca II 8542 RBEs being closer to the magnetic regions is also illustrated in Figure 1(c): most of the red lines (Ca II 8542) are at the base of the green Hα RBEs. The single RBE in Figure 2 is also found in Ca II 8542 with the latter feature located closer to the magnetic bright points in the upper right (where the RBE started to appear a few time steps earlier) than in Hα.

When comparing the statistics of RBEs connected in both spectral lines to the ones that are not connected, two properties stand out. The average lifetime of an RBE seen in both spectral lines is 83.9 s, whereas in the RBEs only detected in one of the lines the average lifetime is 45.6 s and 46.1 s for Ca II 8542 and Hα, respectively. Also, the average length of RBEs seen in both spectral lines, 3.1 Mm and 3.7 Mm for Ca II 8542 and Hα, respectively, is larger than that of the RBEs only observed in one spectral line, 2.8 Mm and 3.4 Mm for Ca II 8542 and Hα, respectively. This suggests that a successful connection between the two lines is more likely for RBEs that are longer lived and have a longer spatial extent.

The statistics for Doppler velocities and Doppler widths for the connected RBEs shows the same trend as for RBEs detected in only one line: Hα RBEs have generally larger Doppler velocity and larger width.

4.4. Scattered Events

Figures 1 and 6 show that apart from the dense concentrations of RBEs associated with regions of enhanced polarization, there are a significant number of events scattered over the FOV. Here we present statistical properties of these isolated events by masking out the three regions with densest RBE concentrations.

Figure 9 shows histograms for length, Doppler velocity, and Doppler width. The histogram for RBE length peaks just below 3 Mm, just like for the multi-frame RBEs in Figure 4(a), but there is no extended tail toward longer lengths (note that some of the scattered RBEs show temporal evolution and are part of both Figures 4 and 9). The histograms for Doppler velocity and width are similar as for multi-frame RBEs.

Figure 10 shows sample images of two scattered Hα RBEs. The top panels are from an event that appeared one time step earlier in the far blue wing in the middle of a granule. The RBE could be followed for four time steps so it has a lifetime of more than 36 s. In the left panel, the RBE appears to cross a granule, while in the images closer to the line core (for example the middle panel), it seems to be part of a structure that is rooted in the intergranular lane to the right of the granule. No photospheric bright point or enhanced polarization signal that is obviously associated with this event is present in this area.

The bottom panels show an RBE that was visible for eight time steps, and like the previous example seems to cross granules and is not obviously connected to magnetic regions in the vicinity. The line core image however suggests that the RBE is

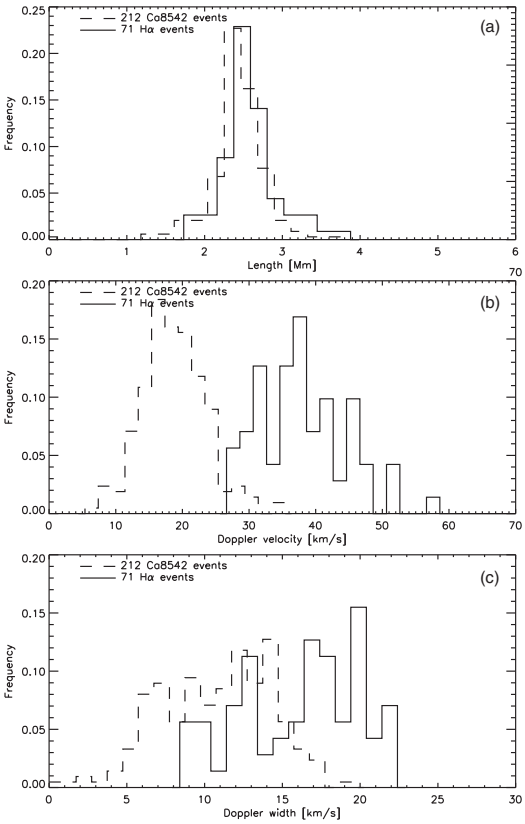

Figure 9. Histograms for (a) length, (b) Doppler velocity, and (c) Doppler width for RBEs scattered over the FOV, i.e., not associated with enhanced polarization signal (see Figure 1(d)).

associated with the dense fibrils that are rooted in the extended magnetic region to the upper right, which dominated the FOV in Figure 1. The closest photospheric bright points along the direction of the RBE main axis are more than 10″ away.

5. DISCUSSION

We studied the disk-counterparts of type II spicules that are observed as short-lived, elongated features in the blue wings of strong absorption lines like the Hα and Ca II 8542 spectral lines. These features are also known as rapid blueshifted excursions due to their asymmetric, blueward spectral profile. The work presented here is in many ways a continuation and elaboration of the work of Paper I. We observed a similar target, a coronal hole, and employed a program of simultaneous Hα and Ca II 8542 spectral scans. The observation program was specifically tailored for the observation of RBEs with reasonably high temporal cadence and sufficient resolution for robust spectral analysis. This allowed us to more directly compare the two spectral diagnostics, a comparison which could only be done indirectly from the data employed in Paper I, where RBEs were studied in two separate but sequentially recorded single-line time series in Hα and Ca II 8542. Furthermore, we have extended the method of automated detection of RBEs to allow for a

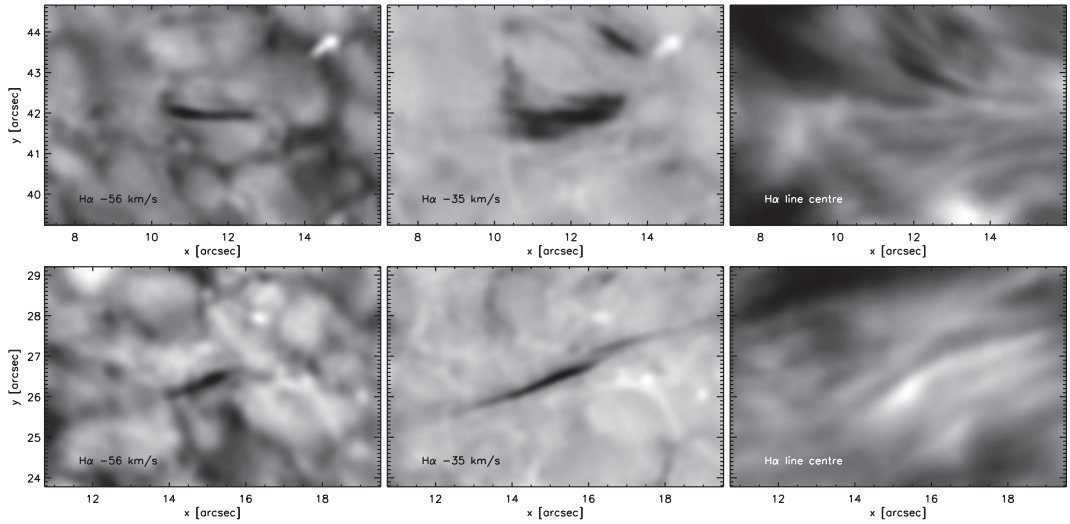

Figure 10. Sample Hα images of two scattered RBEs. Left panels are images in the blue wing at −1200 mÅ, middle panels at −760 mÅ, and right panels in the line center.

temporal connection between RBE detections so that properties such as lifetimes and transversal motion could be studied more rigorously on an extended statistical sample. In Paper I, these properties were measured manually on a limited subsample of the RBE detections.

5.1. Statistical Properties of RBEs

We present histograms on RBE lengths, and Doppler velocities and Doppler widths for 1890 Ca II 8542 and 1601 Hα RBEs in Figure 4. These measurements agree very well with those presented in Paper I. We confirm that a larger number of longer RBEs ($\gtrsim$3.5 Mm) can be observed in Hα, while the shortest RBEs ($\lesssim$2 Mm) are observed in Ca II 8542. We confirm that in Hα, one observes larger Doppler velocities and larger Doppler widths than for Ca II 8542 RBEs.

These RBEs were connected in temporal chains and combined to form 507 Ca II 8542 and 453 Hα multi-frame RBEs for which we could determine the lifetime and transversal motion. This is an increase in statistical sample size of more than an order of magnitude for this type of measurements.

T. Pereira et al. (2011, private communication) measure statistical properties of 111 type II spicules from two *Hinode* Ca II H limb time series. Their results allow for a more detailed comparison between RBE properties and spicule type II properties than was possible for Paper I. They find lifetimes ranging between 20 and 160 s, with the peak of the distribution around 1 minute and an average of about 80 s. For our sample of RBEs, we find a similar range in lifetimes but the peak of the distribution to be well below 1 minute and an average of 50 s. We note that for the RBEs that can be identified in both Ca II 8542 and Hα, we find an average lifetime that agrees well with the Pereira et al. result.

Pereira et al. find for the transverse motion the average velocity ranging between 0 and 20 km s^{-1}, with the peak of the distribution at about 6 km s^{-1}. We find a similar range in velocities, but most of the measurements for RBEs yield lower velocities, with the average at $\sim$4 km s^{-1} for Ca II 8542 and $\sim$5 km s^{-1} for Hα. The measurements of the transverse motion of 35 RBEs in Paper I, resulted in a transverse velocity of order 8 km s^{-1}. These Hα RBEs were selected manually but we confirmed that result by applying the method of automated measurement of transverse motion to the 2008 data set and found an average of 7.6 km s^{-1} for 179 Hα RBEs. We attribute this higher value for the transverse velocity to the higher cadence of the 2008 Hα data set which was almost two times faster than the 2010 data. This allows for the measurement of higher velocity motions because the upper limit of maximum allowed distance between time steps is larger. For the 2008 Ca II 8542 data set, which is at similar cadence as the 2010 data, we find an average of 4.4 km s^{-1} for 94 RBEs. For the 2010 July 3 data set, we find average transverse velocities that are very similar as for 2010 June 27.

De Pontieu et al. (2007) discovered Alfvénic waves in the chromosphere using type II spicules as tracers for oscillatory motions. The velocity amplitude was measured for 94 spicules, which can be compared to the distribution of the peak transverse velocity in Figure 5(c). They found a range between 0 and 30 km s^{-1}, with the peak of the distribution around 15 km s^{-1}. As for the average transverse velocity, RBEs display a comparable range but mostly lower values for the peak transverse velocity as compared to type II spicules at the limb. Continuing on the arguments of the previous paragraph, we note that the measurements of the RBE transverse velocities seem to be limited by the cadence of the time series. Faster cadence observations are needed to properly resolve the distribution of transverse velocities of RBEs.

For the transverse displacement, Pereira et al. find values ranging between 0 and 1.4 Mm, with most values between 0.1 and 0.5 Mm, in close agreement with the De Pontieu et al. (2007) measurements. We find a total transverse displacement of less than 1 Mm for RBEs, with most RBEs covering a distance of less then 0.2 Mm during their lifetime.

Even though the shapes of the statistical distributions of properties of RBEs and type II spicules observed at the limb differ in detail, the similarities between the distributions provide

a sufficient basis for the interpretation of RBEs being the disk counterparts of type II spicules, as already put forward in Paper I. In addition to similarity in statistics, we observe that RBEs rapidly disappear or fade, and that RBEs show both swaying motion and apparent motion away from magnetic regions, which can be interpreted as an upward motion. There are no signs of flows returning to the surface associated with RBEs. This kind of dynamical behavior is one of the defining characteristics of type II spicules observed in Ca II H at the limb.

The most striking difference between RBEs and type II spicules is the distribution of lengths. Pereira et al. measure a range between 1.5 and 11.5 Mm, with the average length around 6 Mm. We find for RBEs an average length around 3 Mm and only few Hα RBEs measure up to 6 Mm. This difference can be attributed to the fact that above the limb, faint signals toward the top of spicules can still be reliably detected against the dark background. Against the disk, however, these top parts of spicules are likely to have too little opacity to be detected as an integral part of RBEs. So there is likely an intrinsic bias for shorter lengths measured for RBEs. For length measurements of type II spicules at the limb, there is arguably also a selection effect for detecting longer spicules that stick out above the dense forest of spicules encountered in limb observations. The same projection effect could possibly explain the trend of higher transverse velocity and transverse displacement measured for spicules at the limb: tall spicules that extend to greater heights move in a lower density environment, so for equal wave energy flux they can be expected to display higher velocities and thus cover greater transverse distances.

5.2. RBE Detection Rate

In Paper I, in the 40 minute Ca II 8542 time sequence with a cadence of 11 s, 413 RBEs were detected from Doppler maps at 30 km s^{-1}. With the 215 time steps, this corresponds to a detection rate of 1.9 RBEs per time step. In the 24 minute Hα time sequence with a cadence of 6.7 s, 608 RBEs were detected from difference maps at 60 km s^{-1}. With the 245 time steps, this corresponds to a detection rate of 2.5 Hα RBEs per time step. We note that detection velocities of 30 km s^{-1} for Ca II 8542 and 60 km s^{-1} for Hα are on the extreme end of the average Doppler velocities found for RBEs; see Figure 4 (or Figure 10 in Paper I). Given the typical values for the Doppler width and velocity it is likely that at these extreme detection velocities, a significant fraction of RBEs have absorption signals that are too faint to be detected by the automated method. In this work we investigated the detection rate as a function of the detection velocity used in the automated method. We find similar detection rates to Paper I at the detection velocities used in Paper I: 3.4 RBEs per time step for Ca II 8542 and 1.8 RBEs per time step for Hα. Running the automated detection method on maps constructed at lower Doppler velocity, we find a significant increase in the detection rate; see Figure 3. At 30 km s^{-1} we had a detection rate of 48 Hα RBEs per time step, an increase in the number of detected events of more than a factor 25. For Ca II 8542 we see a similar increase in the detection rate toward lower Doppler velocity, but we found that at the lowest Doppler velocity possible in our data set, 12 km s^{-1}, the fraction of false detections was too large and the detections are not reliable. For the detection velocity for which we present RBE statistics, 20 and 45 km s^{-1} for Ca II 8542 and Hα, we see an increase in the detection rate with a factor of about 6, to 14.2 and 11.1 RBEs per time step, as compared to the Paper I detection velocity. This resulted in a significant increase of the RBE sample used for detailed analysis in this work.

We find similar trends of increased RBE detections at lower Doppler velocity for the 2010 July 3 data set and the 2008 June 15 data sets used in Paper I.

We also note that the automated detection method does not identify all RBEs present in the data. We estimate that for the 45 km s^{-1} Hα detection maps, only about half of the events that are visually identified as genuine RBEs are registered by the automated detection. Running the detection routine on lower Doppler velocity maps results in a lower relative number of undetected RBEs (about a quarter remains undetected), but we must underline that we considerably underestimate the abundance of RBEs in our data.

Judge et al. (2011) proposed that type II spicules correspond to warps in two-dimensional sheet structures as an alternative to the main-stream interpretation of spicules being tube-like structures. One of their arguments in favor of sheet-like structures is that RBEs (which are hard to interpret as "sheets") are not the disk counterparts of type II spicules because the occurrence rate of RBEs is at least an order of magnitude lower than type II spicules observed at the limb. From the number of detected RBEs in Paper I, they extrapolate to an estimate of 10^5 RBEs on the Sun at any given time. This is then orders of magnitude lower than estimates for type II spicules, e.g., 2×10^7 (Judge & Carlsson 2010), and Beckers's (1968) estimate of 10^6 for what are now considered as classical spicules.

The detection rate of RBEs at lower Doppler velocity we find here agrees with the estimate of a total number of $\sim 10^5$ RBEs (see Figure 3). However, as argued above, the RBE detection rate we find here is an absolute lower limit that significantly underestimates the actual number of spicules for several reasons.

First, the automated detection rate rejects a significant fraction of real RBEs to avoid false positives.

Second, there are clear indications that many spicules lack opacity to show a disk counterpart signal. Detecting an RBE-like feature against the disk requires observations of excellent quality, and most importantly requires that the RBE has a certain degree of enhanced opacity. Our disk observations indicate that the opacity of RBEs varies strongly between the Ca II 8542 and Hα lines, with the former showing significantly fewer and shorter features (concentrated toward the bottom of the Hα features). This is compatible with an ever decreasing opacity in chromospheric lines as one moves away from the footpoints. This is not surprising because limb spicules also show a very strong decrease in intensity (with scale height of the order of 2000 km) over their full length. It is thus highly likely that there is a significant number of faint RBEs that cannot be detected even in Hα. We note that RBEs are very difficult to observe: detecting RBEs was impossible before the advent of subarcsecond, high-cadence, high signal-to-noise imaging spectroscopy with Fabry–Perot interferometers. It is quite possible that even higher quality observations would increase the detection rate significantly.

Third, RBE detection is subject to strong "velocity filtering": due to the unknown angle between the velocity vector and line-of-sight vector, our method always misses features that are significantly inclined from the line of sight. This is especially the case because we cannot distinguish RBEs from other chromospheric features at velocities closer to the core. The increase of the number of RBE detections for lower Doppler velocity as illustrated in Figure 3 indicates that there might be a significant number of RBEs at even lower Doppler velocity that

are not detected by our method. Detection of type II spicules at the limb suffer much less from these latter two effects: it is relatively easy to detect faint signals against the off-limb dark background (with space-based instruments like *Hinode* that do not suffer from seeing effects introduced by Earth's atmosphere) and velocity filtering is much less an issue for the relatively wide passband of the *Hinode*/SOT Ca H filter.

In the discussion of Paper I, it was argued that the detection rate of RBEs on the disk corresponds to a detection of 1.9 RBEs per linear arcsec if they were observed at the limb. This was considered to be in reasonable agreement with an order of magnitude estimate of the number of type II spicules per linear arcsec from the De Pontieu et al. (2007) observations. In this study, we confirm the results from Paper I and find that the detection rate extrapolates to $\sim$1–2 $\times$ 10^5 RBEs over the whole Sun. We caution that all of these occurrence rate estimates, including those of Beckers (1968) and Judge & Carlsson (2010) are based on incomplete data sets, limiting assumptions, and observational limitations, and should thus be taken with a grain of salt. For example, it is not clear from Judge & Carlsson (2010) how deterministic their occurrence rate of 10^7 type II spicules really is. The visual comparison in their paper is unconvincing with their simulations showing many more spicules than observations do: $\sim 10^7$ type II spicules would correspond to more than 100 spicules per linear arcsec at the limb or more than 5 spicules per *Hinode*/SOT pixel, in contradiction to observations. This implies that the 10^7 type II spicules estimated by Judge & Carlsson (2010), is likely a significant overestimation of the number of type II spicules at the limb. In any case, their argumentation for that number is based on a series of assumptions and models whose effect on the estimated number of spicules has not been studied or estimated. This sheds doubt on the robustness of their determined detection rate.

We conclude that the rejection of Judge et al. (2011) of RBEs being the disk counterparts of type II spicules on the basis of too low an occurrence rate is unjustified. There may well be sheet-like features in the atmosphere, but challenging the "tube hypothesis" based on rejection of the RBEs as disk counterparts of spicules is not convincing for the reasons outlined above.

5.3. Acceleration along RBEs

Paper I reported a systematic variation of the Doppler velocities and widths: many RBEs were found to show an increase of Doppler shifts and widths from the footpoint to the top. We confirm this trend in the 2010 data, which is visually evident from Figure 6, which shows the Doppler measurements as a function of their position in the FOV. In this representation, the orientation of (most of) the RBEs can be comprehended with respect to their footpoints which appear to be rooted in the magnetic field concentrations. The trend of increasing Doppler velocity and width for many RBEs is particularly striking for the Hα RBEs. We note that there is also a significant number of RBEs displaying a more erratic variation of their Doppler properties.

Irrespective of the variation along the RBE main axis, we report a more general trend of increasing Doppler width for Doppler velocity in Figure 7. This trend illustrates the characteristic spectral profile at the location of RBEs, which consists of a wide blueward asymmetry (from which the RBE profile is then extracted by subtraction of a background profile). This is different from profiles with a narrow, isolated absorption component which can for example sometimes be observed for on-disk coronal rain (Antolin & Rouppe van der Voort 2012; Antolin et al. 2011). Sometimes coronal rain condensations appear as separated absorption profiles in the far wings of Hα. This is unusual for RBEs, even for RBEs that are oriented along the line of sight and appear as small, roundish features with strong absorption in the blue wing (dubbed "black beads" in Paper I); the spectral profile displays enhanced absorption throughout the blue extending to large Doppler offset.

In any case, the correlation between Doppler velocity and widths and tendency toward increased values for both parameters toward the top of the RBEs may suggest a link between the acceleration and heating mechanism involved in RBEs, if we speculate that the Doppler widths are related to temperature. Whatever the cause of this intriguing correlation, it provides strict constraints for any theoretical model for spicules.

5.4. Comparing Hα and Ca II 8542 RBEs

From the sequentially recorded Hα and Ca II 8542 data sets of Paper I, it was observed that Ca II 8542 RBEs are located closer to magnetic regions and it was inferred that the Ca II 8542 line samples the lower part of spicules. In our data sets with co-temporal Hα and Ca II 8542 observations, we can directly confirm that the two lines sample different parts of RBEs, with the Ca II 8542 line sampling the bottom part of the spicule, and Hα sampling the upper part, and both lines sampling an overlapping region in the middle (see Figure 8). Even though the automated detection method does not nearly identify all RBEs in both lines, we find from visual inspection that virtually all RBEs display signal in both lines.

This observation strengthens the explanation for the differences in Doppler velocity measured in Hα and Ca II 8542 (see Figure 4) as put forward in Paper I: Hα is sampling the top part of spicules where lower density plasma is propelled to higher velocities.

The observation of the Ca II 8542 and Hα lines sampling different parts of RBEs also removes some of the discrepancy between length measurements of RBEs and type II spicules at the limb: we can infer that the actual length of the RBEs is longer than measured in the two lines separately. In addition, of course, it remains the case that we cannot expect to completely remove the length discrepancy between RBEs and type II spicules. This is because off-limb measurements allow for more reliable measurements of faint signals.

5.5. Scattered RBEs

We find most RBEs to be concentrated near regions with enhanced magnetic fields. In addition to these dense concentrations, we find a number of more isolated RBEs that are scattered around the FOV. When comparing statistical properties of length, Doppler velocity, and Doppler width, we find that these isolated events are not particularly different from the RBEs in denser regions, except that we do not find a population of longer RBEs. For these isolated RBEs, it is often unclear if they have any association with regions of enhanced magnetic fields, although we note that our diagnostic, Ca II 8542–600 mÅ Stokes *V* maps, is not a particularly sensitive measure for magnetic fields. One might speculate that a more sensitive diagnostic might reveal a connection to weaker and possibly more extended, magnetic fields.

From fixed wavelength, -1300 mÅ Hα observations from the 1.6 m New Solar Telescope (NST) at Big Bear Solar Observatory, Goode et al. (2010) report the observation of small jet-like features that appear to originate from intergranular lanes. The authors claim that these features are different from

RBEs, as they are not unequivocally tied to strong magnetic field concentrations.

Figure 10, shows blue-wing Hα images of two examples of scattered RBEs. The left panels show far blue wing images of these events. In these images, these events seem to match the description of the jet-like features described by Goode et al. (2010): narrow features that cross granules and are not obviously connected to magnetic regions in the vicinity. The spectro-temporal information that we have for this data, however, reveals that these events are RBEs. Even though the bottom example of Figure 10 is not directly associated with photospheric bright points, it seems plausible that this feature is related to the extended magnetic region in the upper-right part of the FOV.

Goode et al. (2010) report a typical length of 1 Mm and a typical width of 0.2 Mm for the jet-like features in their blue-wing Hα data. The width agrees well with what we find for RBEs; the length is compatible but on the short side. It should be noted that the length in Goode et al. (2010) is measured at a fixed wavelength position at 60 km s^{-1} Doppler offset, while we measure RBE lengths taking the spectral profile into account. This naturally leads to a trend of measuring longer lengths. We confirmed visually that RBE lengths at fixed wavelength filtergrams have a trend of becoming shorter at a higher Doppler offset.

Given the striking similarities, we interpret the jet-like features reported by Goode et al. (2010) as similar features to what we observe as isolated RBEs scattered over the FOV.

6. CONCLUDING REMARKS

The statistical properties resulting from this data set, along with better estimated occurrence rates, further strengthen the interpretation of RBEs as the disk counterpart of type II spicules as first proposed by Langangen et al. (2008) and further established in Paper I. Given their important role in understanding the outer solar atmosphere, either as seemingly passive tracer for the pervasive presence of Alfvénic waves (De Pontieu et al. 2007) or more directly as a potential source for mass loading and heating of the corona (De Pontieu et al. 2011), further observational study of type II spicules is highly desired in order to advance knowledge of their physical nature. An essential property that is not part of this work but can readily be addressed from the analysis method employed on this time series is the spectral evolution of RBEs during their lifetime. Such detailed study of the temporal evolution of RBEs is currently under way and will be the subject of a forthcoming paper. We further note that observations from the *Solar Dynamics Observatory* of this target provide the possibility of investigating the response of the transition region and coronal diagnostics to RBEs.

The Swedish 1 m Solar Telescope is operated by the Institute for Solar Physics of the Royal Swedish Academy of Sciences in the Spanish Observatorio del Roque de los Muchachos of the Instituto de Astrofísica de Canarias. This research has made use of NASA's Astrophysical Data System. B.D.P. was supported through NASA grants NNX08BA99G, NNX08AH45G, and NNX11AN98G.

REFERENCES

Antolin, P., & Rouppe van der Voort, L. 2012, ApJ, 745, 152
Antolin, P., Vissers, G., & Rouppe van der Voort, L. 2011, Sol. Phys.
Beckers, J. M. 1968, Sol. Phys., 3, 367
de la Cruz Rodríguez, J. 2010, PhD thesis, Stockholm Univ.
de la Cruz Rodríguez, J., & Socas-Navarro, H. 2011, A&A, 527, L8
De Pontieu, B., Erdélyi, R., & James, S. P. 2004, Nature, 430, 536
De Pontieu, B., Hansteen, V. H., Rouppe van der Voort, L., van Noort, M., & Carlsson, M. 2007, ApJ, 655, 624
De Pontieu, B., McIntosh, S. W., Carlsson, M., et al. 2007, Science, 318, 1574
De Pontieu, B., McIntosh, S. W., Carlsson, M., et al. 2011, Science, 331, 55
De Pontieu, B., McIntosh, S. W., Hansteen, V. H., & Schrijver, C. J. 2009, ApJ, 701, L1
De Pontieu, B., McIntosh, S., Hansteen, V. H., et al. 2007, PASJ, 59, 655
Goode, P. R., Yurchyshyn, V., Cao, W., et al. 2010, ApJ, 714, L31
Hansteen, V. H., De Pontieu, B., Rouppe van der Voort, L., van Noort, M., & Carlsson, M. 2006, ApJ, 647, L73
Judge, P. G., & Carlsson, M. 2010, ApJ, 719, 469
Judge, P. G., Tritschler, A., & Chye Low, B. 2011, ApJ, 730, L4
Langangen, Ø., De Pontieu, B., Carlsson, M., et al. 2008, ApJ, 679, L167
Martínez-Sykora, J., Hansteen, V., & Moreno-Insertis, F. 2011, ApJ, 736, 9
Rouppe van der Voort, L., Leenaarts, J., De Pontieu, B., Carlsson, M., & Vissers, G. 2009, ApJ, 705, 272
Rouppe van der Voort, L. H. M., De Pontieu, B., Hansteen, V. H., Carlsson, M., & van Noort, M. 2007, ApJ, 660, L169
Scharmer, G. B., Bjelksjo, K., Korhonen, T. K., Lindberg, B., & Petterson, B. 2003a, Proc. SPIE, 4853, 341
Scharmer, G. B., Dettori, P. M., Lofdahl, M. G., & Shand, M. 2003b, Proc. SPIE, 4853, 370
Scharmer, G. B., Narayan, G., Hillberg, T., et al. 2008, ApJ, 689, L69
Schnerr, R. S., de la Cruz Rodríguez, J., & van Noort, M. 2011, A&A, 534, A45
Sterling, A. C. 2000, Sol. Phys., 196, 79
van Noort, M., Rouppe van der Voort, L., & Löfdahl, M. G. 2005, Sol. Phys., 228, 191
van Noort, M. J., & Rouppe van der Voort, L. H. M. 2008, A&A, 489, 429
Vissers, G., & Rouppe van der Voort, L. 2012, ApJ, 750, 22

Paper II

On the Temporal Evolution of the Disk Counterpart of Type II Spicules in Quiet Sun

Sekse, D.H., Rouppe van der Voort, L. and De Pontieu, B.

ApJ, 764, 164 (2013)

The Astrophysical Journal, 764:164 (14pp), 2013 February 20 doi:10.1088/0004-637X/764/2/164

ON THE TEMPORAL EVOLUTION OF THE DISK COUNTERPART OF TYPE II SPICULES IN THE QUIET SUN

D. H. Sekse[1], L. Rouppe van der Voort[1], and B. De Pontieu[2]
[1] Institute of Theoretical Astrophysics, University of Oslo, P.O. Box 1029, Blindern, N-0315 Oslo, Norway
[2] Lockheed Martin Solar & Astrophysics Lab, Org. A021S, Bldg. 252, 3251 Hanover Street, Palo Alto, CA 94304, USA
Received 2012 October 23; accepted 2012 December 19; published 2013 February 4

ABSTRACT

The newly established type II spicule has been speculated to provide enough hot plasma to play an important role in the mass loading and heating of the solar corona. With the identification of rapid blueshifted excursions (RBEs) as the on-disk counterpart of type II spicules we have analyzed three different high-quality timeseries with the CRisp Imaging SpectroPolarimeter (CRISP) at the Swedish Solar Telescope on La Palma and subjected to an automated detection routine to detect a large number of RBEs for statistical purposes. Our observations are of a quiet-Sun region at disk center and we find lower Doppler velocities, 15–40 km s^{-1}, and Doppler widths, 2–15 km s^{-1}, of RBEs than in earlier coronal hole studies, 30–50 km s^{-1} and 7–23 km s^{-1}, respectively. In addition, we examine the spatial dependence of Doppler velocities and widths along the RBE axis and conclude that there is no clear trend to this over the field of view or in individual RBEs in the quiet Sun at disk center. These differences with previous coronal hole studies are attributed to the more varying magnetic field configuration in quiet-Sun conditions. Using an extremely high-cadence data set has allowed us to improve greatly on the determination of lifetimes of RBEs, which we find to range from 5 to 60 s with an average lifetime of 30 s, as well as the transverse motions in RBEs, with transverse velocities up to 55 km s^{-1} and averaging 12 km s^{-1}. Furthermore, our measurements of the recurrence rates of RBEs provide important new constraints on coronal heating by spicules. We also see many examples of a sinusoidal wave pattern in the transverse motion of RBEs with periods averaging 54 s and amplitudes from 21.5 to 129 km which agrees well with previous studies of wave motion in spicules at the limb. We interpret the appearance of RBEs over their full length within a few seconds as the result of a combination of three kinds of motions as is earlier reported for spicules. Finally, we look at the temporal connection between Hα and Ca II 8542 RBEs and find that Ca II 8542 RBEs in addition to being located closer to the footpoint also appear before the Hα RBEs. This connection between Ca II 8542 and Hα supports the idea that heating is occurring in spicules and contributes more weight to the prominence of spicules as a source for heating and mass loading of the corona.

Key words: Sun: chromosphere – Sun: corona

Online-only material: animations

1. INTRODUCTION

When studying the solar chromosphere, numerous highly dynamical events can be observed taking place on very short timescales. One of these types of events is the thin jet-like features which can be seen protruding from the solar limb, called spicules. These jets have been observed and studied for several decades (for extensive reviews; see Beckers 1968; Suematsu et al. 1995; Sterling 2000; Tsiropoula et al. 2012), but only in the last few years has great progress in the characterization of these events been made. The launch of the *Hinode* satellite, situated in a seeing-free environment and equipped with a large aperture, opened an unprecedented view on the solar limb with high spatial and temporal resolution. From long-duration Ca H timeseries obtained with *Hinode*, a new type of spicule was discovered (De Pontieu et al. 2007c), which differentiates from the classical spicule by displaying only upward motion, shorter lifetimes, and higher velocities. These so-called type II spicules have typical lifetimes between 50 and 150 s, velocities between 30 and 110 km s^{-1}, and fade at around their maximum length (Pereira et al. 2012). The extensive work by Pereira et al. (2012) confirms the measurements from De Pontieu et al. (2007c) and contradicts claims by Zhang et al. (2012) that there are no type II spicules.

The type II spicule has been found to display a characteristic sideways swaying motion that has been regarded as a sign that the chromosphere is permeated with Alfvénic waves with energies large enough to accelerate the solar wind and potentially heat the quiet corona (De Pontieu et al. 2007b). In recent years, several studies have strengthened the interpretation that type II spicules play an important role in the mass loading and heating of the corona (De Pontieu et al. 2009, 2011). A wave analysis of high-cadence *Hinode* limb observations found a mix of upward propagating, downward propagating, and standing waves in spicules (Okamoto & De Pontieu 2011) whereas Judge et al. (2012) observed extremely high-cadence Hα wings and reported on the sudden appearance of spicule-like structures close to the limb that exhibit extreme propagation speeds. De Pontieu et al. (2012) demonstrated that the complex dynamical appearance of type II spicules must be interpreted as the result of the combination of three different types of motion: field aligned flows, swaying motions, and torsional motions.

While the classical type I spicule is well und1erstood and has been identified as the off-limb counterpart to on-disk dynamic fibrils in active regions (De Pontieu et al. 2004; Hansteen et al. 2006; De Pontieu et al. 2007a), the formation and driver of the type II spicule are still under debate. In their three-dimensional radiative magnetohydrodynamics simulation, Martínez-Sykora et al. (2011) describe in detail the formation of jets that resemble type II spicules in that cool chromospheric plasma is ejected into the corona while being heated to temperatures that are high enough to cause apparent fading in typical chromospheric diagnostics. The cause for these jets in the simulations is the increase in gas pressure from accelerated chromospheric

plasma that is accelerated by Lorentz forces arising from flux emergence. This triggers the ejection of plasma into the low-density corona. However, further modeling is required to firmly establish the physical mechanism that drives type II spicules.

In order to improve on the simulations of spicules, high-quality observations prove to be essential when it comes to constraining the models and guiding the direction of investigations. Unfortunately, spicule properties have proven to be notoriously difficult to measure at the solar limb due to the superposition of many spicules along the line of sight combined with their narrow spatial extent and significant displacement during their short lifetime. The problem of superposition can be overcome by observing their disk counterpart. The disk counterpart of type II spicules has been identified as short-lived and rapidly moving absorption features in the strong chromospheric Hα and Ca II 8542 spectral lines (Langangen et al. 2008; Rouppe van der Voort et al. 2009, Paper I). Sekse et al. (2012, Paper II) greatly expanded on the statistics of these events, commonly referred to as "rapid blueshifted excursions" (RBEs).

Here, we continue the work of Paper II by addressing various properties associated with the temporal evolution of RBEs. We use several data sets: the dual line Hα+Ca II 8542 data set from Paper II, as well as two new Hα data sets, of which one has an extremely high cadence of 0.88 s. This data set allows us to properly resolve the RBEs in time so that the lifetime of RBEs can be firmly established. The extreme temporal resolution merits further investigation of the apparent motion of some of the RBEs. The new data sets are of the quiet Sun and allow us to investigate differences with coronal hole RBEs as the previous studies, Papers I and II, are based on coronal hole target regions.

2. DATA REDUCTION AND OBSERVATIONS

The observations were obtained using the CRisp Imaging SpectroPolarimeter (CRISP; Scharmer et al. 2008) instrument at the Swedish 1 m Solar Telescope (SST, Scharmer et al. 2003a) on La Palma. The CRISP instrument contains a dual Fabry–Pérot interferometer (FPI) and three high-speed low-noise CCD cameras which operate at a frame rate of 35 frames s^{-1} with an exposure time of 17 ms per frame. Two of the cameras are located behind the FPI and a polarizing beam splitter. The third camera, which is used as an anchor channel for image processing, is positioned before the FPI. All three cameras are located behind the CRISP pre-filter and are synchronized by an optical chopper. CRISP has a field of view (FOV) of approximately $61'' \times 61''$ with an image scale of $0\farcs0592$ $pixel^{-1}$ and allows for fast wavelength tuning (<50 ms) between any two positions within the spectral region given by the spectral width of the pre-filter. These high-speed capabilities of CRISP make it an ideal instrument for studies of the dynamic chromosphere using imaging spectroscopy. In this study, we are interested in the Hα and Ca II 8542 lines, for which CRISP has transmission FWHMs of 66 mÅ and 111 mÅ, and pre-filter FWHMs of 4.9 Å and 9.3 Å, respectively. Through the use of the SST adaptive optics system (SST; Scharmer et al. 2003b) and the multi-object, multi-frame blind deconvolution (MOMFBD) image restoration technique (van Noort et al. 2005), we obtain high spatial resolution down to the telescope diffraction limit ($\lambda/D = 0\farcs14$). Employing the cross-correlation method developed by Henriques (2012) minimizes the remaining small-scale seeing signal introduced from the non-simultaneity of the narrowband CRISP images. More information on the details of the MOMFBD restoration and further processing steps can be found in Paper II.

On 2011 May 5 (08:31–09:02 UT), a 31 minute data set was obtained. The telescope was pointed at disk center, $(x, y) \approx (19'', 5'')$, which was a quiet-Sun region with some magnetic network concentrations scattered over the FOV; see Figure 1. This data set was optimized for studying the fast temporal evolution of RBEs and consisted of only four line positions—$\pm$1032 mÅ, line core, and $-$2064 mÅ—allowing for a cadence of 0.88 s. This extremely fast cadence allows us to resolve the temporal evolution of RBEs to much shorter timescales than previous studies. In addition to this data set, we acquired a time series of the same target just prior to this observation which consisted of 35 line positions symmetrically sampled up to $\pm$1290 mÅ, with 86 mÅ spacing, plus four additional blue wing positions going as far as $-$2064 mÅ, resulting in a cadence of 7.96 s. This other data set enables us to verify the validity of our detection methods, and explore differences between RBEs in the quiet Sun and coronal hole found in previous studies.

Finally, we analyze the dual-line Ca II 8542 and Hα data set from Paper II. This is a 38 minute, 11.77 s cadence, coronal hole observation away from disk center, $(x, y) \approx (-70'', 508'')$, ($\mu = 0.84$), targeting a unipolar magnetic island. For more details and characteristics on this data set we refer to Paper II.

3. METHOD

The RBEs were located within the data sets by the use of an automated detection algorithm working on Hα Dopplergrams, which is mostly identical to the one used in Paper II. The only differences are some minor modifications allowing us to detect shorter events, $\approx$600 km (14 pixels), than in Paper II where a threshold of 17 pixels or $\approx$725 km was used in order to reduce the number of false positives, which resulted in a steep and possibly artificial cutoff in the lower limit of RBE lengths. Because of the excellent quality of the data used in this study we can reduce the allowed length of detected RBEs to give us an increase in reliable detections. We set the new lower limit of allowed RBE lengths at 14 pixels due to an exponential increase in the detection of false positives at slightly lower lengths. We also found that using Hα Dopplergrams instead of the difference images of Paper II gives more reliable detections, as fainter RBEs stand out more clearly, and a slight increase in the number of detections.

The automated detection routine determines the location of each blueshifted event in both space and time and attempts to link these single timeframe events over time, creating multi-frame RBE chains, a process that is explained in detail in Paper II and not changed for this study. The very high cadence of 0.88 s of this data set provides an excellent opportunity to improve upon the previous measurements of the transverse motions and lifetimes of RBEs, which were limited by low cadence. An average lifetime of approximately 40 s for RBEs and a cadence of the data sets on the order of 10 s, means that multi-frame RBEs were only detectable in 4–5 frames on average, and could potentially suffer from an artificial cutoff in lifetimes around 20 s, which correspond to two frames. In addition, the measurement of transverse motions suffered from strong constraints due to the requirement of introducing an upper limit for the transverse displacement of a multi-frame RBE from one time step to the next in order to avoid linking up single-frame RBEs into false multi-frame RBEs in crowded regions.

Lifetime and transverse motion measurements have been improved upon compared to Paper II where only the duration and displacement of the chains that made up the multi-frame RBEs detected by the automated method were taken into account.

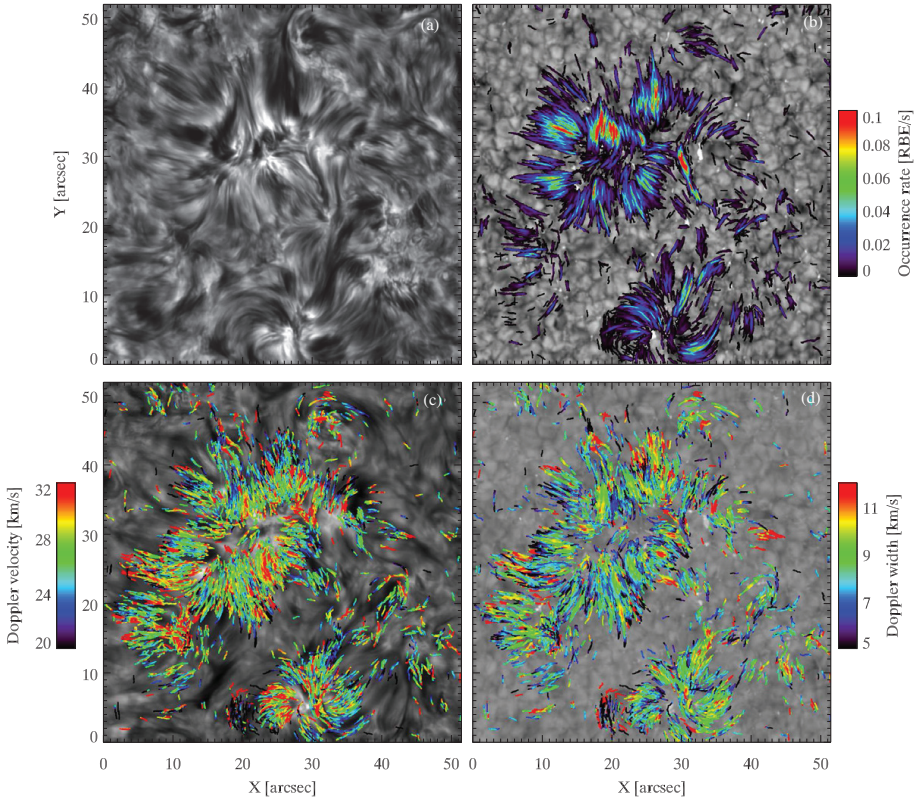

Figure 1. Clean image of the FOV taken from the fast cadence scan at line center (a). An occurrence map of identified RBEs detected at 45 km s^{-1} over the whole fast cadence time series in rainbow color scale plotted over an Hα blue wing image taken at 45 km s^{-1} in the fast cadence time series (b). Doppler properties of the identified RBEs in the full scan time series as a function of their position in the FOV plotted over an image of the line center as seen in the full scan timeseries (c) and an image of the 45 km s^{-1} blue wing position in the full scan data set (d).

Detecting RBEs is tricky and we note that the automated detection method has a limited success rate. To take into account that the method fails to identify all possible detections, due to too faint RBEs being ignored and too short detections being discarded, we choose to improve upon the method to measure lifetimes and displacements by introducing a semi-automated method. Here, the detection chains served as a basis for spacetime diagrams using slits, which are fixed in space, with a width of 20 pixels along the detected multi-frame RBEs. The images of the slits are recorded far into the past and future of the RBEs and each image is averaged over the width of the slits. On these spacetime diagrams, a manual measurement is performed, recording both the lifetime of the event and the transverse motion of the RBE during its lifetime. Any multi-frame RBEs that are found to be erroneous detections based on the image in the spacetime diagram are manually removed from the sample.

Due to the intrinsic difficulty of measuring longitudinal velocities systematically as RBEs display sideway motions and seem to grow erratically, we choose to manually select a number of examples to illustrate the typical behavior.

For the verification of multi-frame RBEs and the creation of the spacetime diagrams, we used a widget-based analysis tool called CRISPEX (Vissers & Rouppe van der Voort 2012), which allows for efficient exploration of multi-dimensional data sets.

4. RESULTS

4.1. Quiet-Sun RBEs

Two different observations of the same quiet-Sun region with different cadences and spectral samplings were searched for RBEs. In the data set with a cadence of 0.88 s, a total of 43,077 events were detected within 31 minutes, giving a detection rate of 20.48 $frame^{-1}$. The data set with a cadence of 7.96 s produced 6795 detected events over 52 minutes with a detection rate of 17.16 $frame^{-1}$.

In Figure 1, the location of every detected event for both data sets is plotted on the FOV. Panel (a) contains a clean image in the Hα linecenter of the FOV seen in the fast cadence data set, while panel (b) shows every detected event and the occurrence rate of RBEs per second from the fast cadence data set plotted over a blue wing image in Hα. The wing position used is the same as the one used when creating the detection Dopplergrams. On average, around the magnetic network where RBEs are detected and considering only those pixels that have an RBE at least once during the time sequence, the occurrence rate is 0.012 RBEs s^{-1}

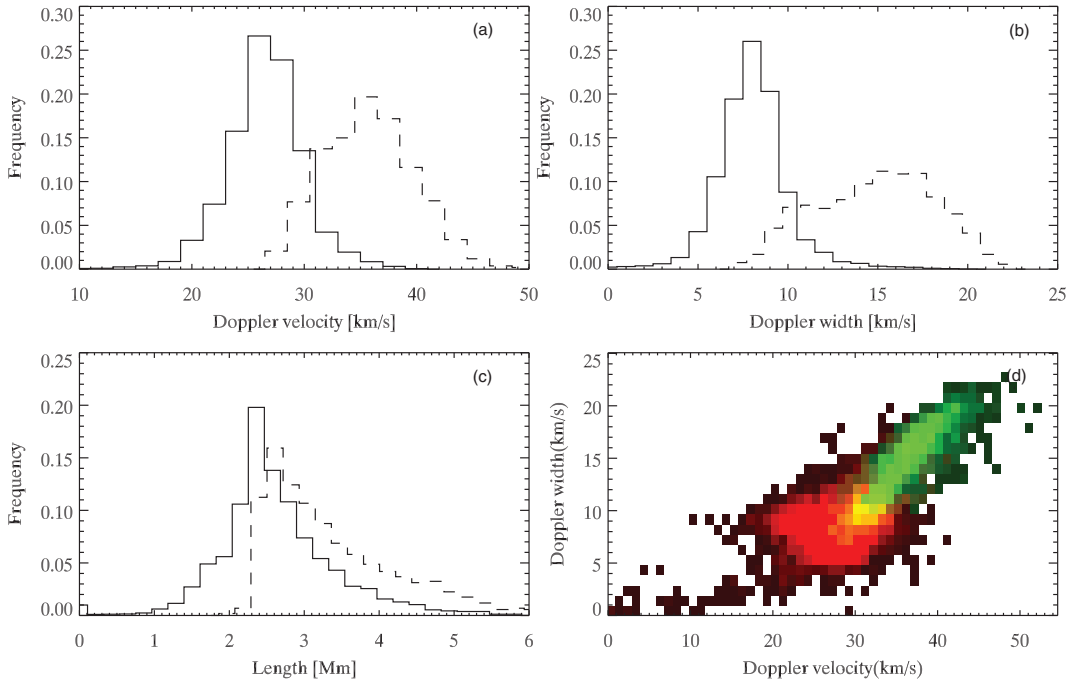

Figure 2. Histograms for (a) Doppler velocity, (b) Doppler width, and (c) length of multi-frame RBEs. The Doppler velocity and Doppler width are average measures for each timestep in each event. All histograms contain data from the 5041 events that make up the multi-frame RBEs. The dashed lines show the results of Paper II. Panel (d) is a density scatterplot of Doppler width against Doppler velocity with data from 2011 May 5 in red and Paper II in green, while yellow signifies overlap.

or one RBE every 84 s. Averaging this number over the full $61'' \times 61''$ area of the FOV, the occurrence rate is 0.0033 or every pixel in the FOV sees on average one RBE every 303 s.

For the last two panels, the underlying image is the same as for panels (a) and (b), but using the low-cadence data set. Overplotted on these images are the positions of every detected event from the low-cadence data set along with their Doppler velocities and Doppler widths in panels (c) and (d), respectively.

Histograms of the Doppler velocity and Doppler width of quiet-Sun RBEs are displayed in Figure 2(a) with Doppler velocity, showing a range from around 15 km s^{-1} up to 40 km s^{-1}, while Doppler widths have a range from 2–3 km s^{-1} up to 15 km s^{-1}.

Figure 2(c) shows the lengths of quiet-Sun RBEs which vary between 1 Mm and 6 Mm. For comparison, the corresponding data from the coronal hole studies in Paper II are added with dashed lines.

The scatterplot in panel (d) shows the distribution of the average Doppler width versus the average Doppler velocity in our quiet-Sun data, in red, and is compared to the same type of scatterplot from Paper II's coronal hole study, in green.

4.2. Spatial Dependence of RBE Properties

Figures 1(c) and (d) show the Doppler velocity and Doppler width along the RBEs for all events located in the timeseries. Most of the RBEs are concentrated around the network regions in the middle left and the center bottom part of the FOV. As these network regions can be interpreted as the footpoint regions for the RBEs, we have a general sense of the orientation for most of the RBEs. With this general sense of orientation in mind, the maps give a rather chaotic impression with a large variation of the Doppler properties along the RBE axis. There appears to be no systematic trend of most RBEs having increasing Doppler velocity or Doppler width toward their top end. To illustrate this, we show three examples of the variation of Doppler properties along the RBE axis in Figure 3. For all three examples, the footpoint (magnetic bright points) is located in the bottom of the subimage, and the RBE is extending toward the top. The top row shows an RBE which has an increase in both Doppler velocity and width away from the footpoint. In the middle row, we see an example which displays a decrease in Doppler velocity and width away from the footpoint, while the final row contains an RBE which has a more variable distribution of Doppler velocities and widths along its length.

4.3. RBE Dynamics from Temporally Resolved Data

4.3.1. Improved Lifetimes

By employing spacetime diagrams of multi-frame RBEs, the measurements of their lifetimes improve drastically. Figure 4 shows the lifetimes resulting from manual measurements on 1951 RBE spacetime diagrams in the solid line where we have a peak in the distribution around 20 s. The shortest living RBEs have a lifetimes of 5.3 s, are seen in only six frames, and stand in contrast to the longest living RBE with its 150 s.

The original lifetimes found by the automated detection routine are shown by the dashed line and stand in contrast to the manually measured lifetimes. From the manual measurements it became clear that the automated procedure failed to follow the

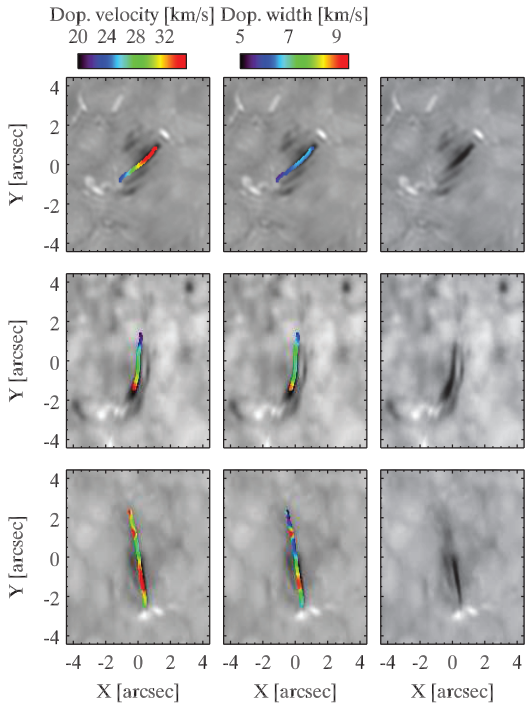

Figure 3. Three examples of the variation of Doppler velocities and Doppler widths along RBEs. Underlying images are Doppler images at the detection velocity from approximately the middle of the RBEs' lifetimes. The detected trajectories of the RBEs are plotted showing Doppler velocities in the left column and Doppler widths in the middle column. The right column contains a clean detection image of the RBEs.

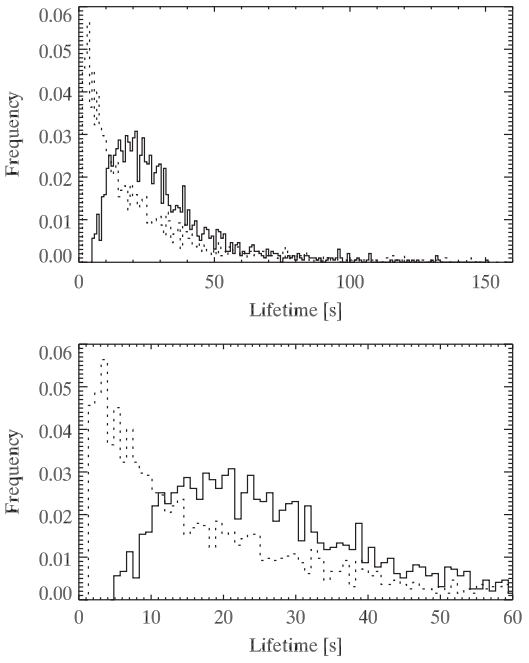

Figure 4. Lifetimes of RBEs from the fast cadence data set with manual measurements shown by the solid line and the automated detection method for the same RBEs shown by the dashed line. The lifetimes found by the automated detection method are added to clarify the imperfections of the detection algorithm. There are individual events out to ∼150 s for the manually measured lifetimes, while the automated detection lifetimes have individual events extending as far as ∼350 s. The top panel shows the entire range of lifetimes found by the manual method. The bottom panel is a zoomed in version of the top panel.

complete lifetime for many RBEs and therefore we see a shift toward longer lifetimes of the whole distribution. In addition, the spacetime diagrams revealed that some of the longest traced RBEs in the automated procedure consisted of several shorter lived RBEs.

4.3.2. Transverse Motions

Most RBEs display transverse displacement perpendicular to their main axis during their lifetimes. Figure 5(a) shows the distribution of the distance between the two extreme positions in the transverse motion of 1951 multi-frame RBEs (solid line) with an average transverse displacement of 200 km. The distribution has a concentration toward the lower end of the scale, but there are cases of a transverse displacement above 1 Mm and the maximum transverse distance recorded is 1.23 Mm. The dashed line in Figure 5(a) represents the integrated transverse displacement, which will show a larger displacement for RBEs that undergo a change of direction during their lifetime as compared to the maximum displacement. This results in an average displacement of 220 km, but the maximum recorded displacement is still 1.23 Mm. In Figure 5(b), the integrated transverse displacement is plotted against the maximum transverse displacement as a measure for the transverse path taken by an RBE, where the dotted line marks where the integrated transverse distance is 50% larger than the distance between the two extreme transverse positions. Of the RBEs ∼13% lie above this dotted line. The solid line, on the other hand, marks where the two transverse displacements are equal and hence, RBEs that lie close to this line are mainly moving in one direction.

Panel (c) shows the distribution of two measures of the transverse velocity: the maximum transverse velocity of each RBE (solid line) and the average unsigned transverse velocity over the whole lifetime of the RBE (dashed line). The maximum transverse velocity has a peak around 9 km s^{-1} and the average of the distribution is 11.77 km s^{-1} with the highest transverse velocity recorded at 57.87 km s^{-1}. For the average velocities, the mean of the sample lies at 8.54 km s^{-1} with a peak of the distribution around 3 km s^{-1}, while the maximum average transverse velocity is found to be 49.93 km s^{-1}.

From Figure 5(b), it is clear that RBEs that do not lie on the solid line have to display some sort of back and forth swaying motion, while those that lie above the dotted line would have more extreme cases of back and forth swaying. Figure 5(d) shows the number of changes in the direction of the transverse motion displayed by the RBEs. On average an RBE will have 0.61 directional changes, but a few RBEs are seen to have up to five changes in the direction of their transverse motion.

4.3.3. Grouping of RBEs Based on Transverse Spacetime Diagrams

Based on the number of transverse directional changes, RBEs can be grouped into different classes. A natural first class (A)

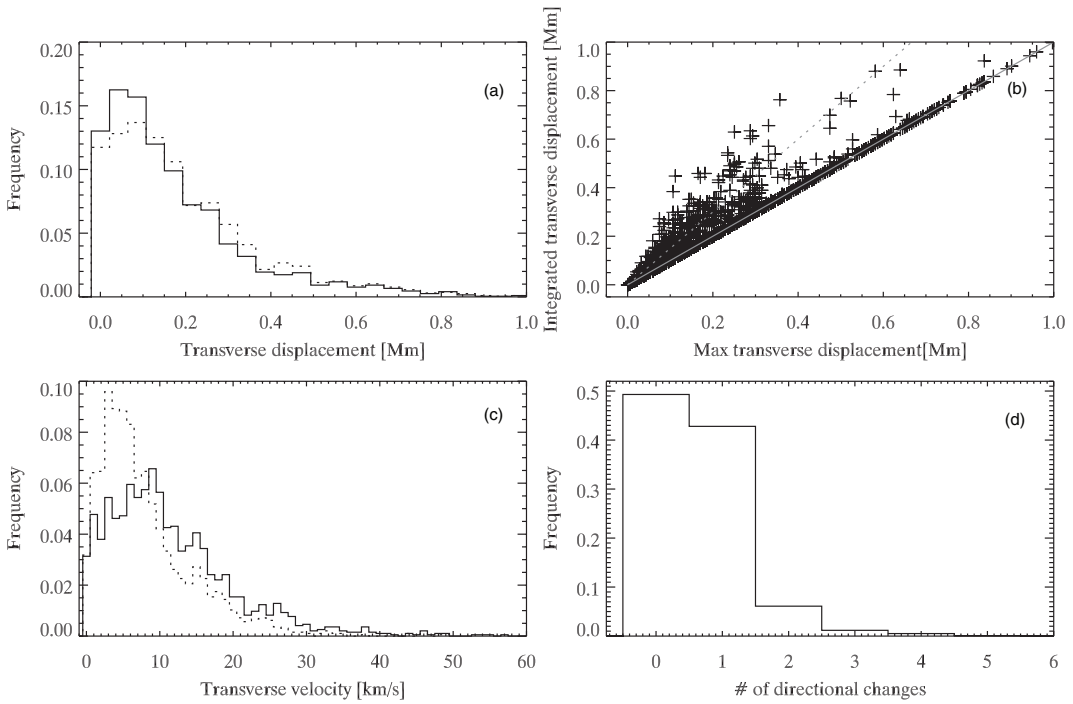

Figure 5. (a) Histogram showing the distance between the two extreme transverse positions during the lifetime of an RBE (solid line) plotted with the integrated or total transverse displacement covered by an RBE during its lifetime (dashed line). (b) Scatter plot showing the relationship between the transverse distance between the two extremes of an RBE and the integrated transverse distance of the same RBE. The solid line marks where the two measurements are equal and the dashed line marks where the integrated displacement is 50% larger than the distance between the two extreme positions. Panel (c) contains a histogram of the maximum transverse velocity during an RBE lifetime (solid line) and the average transverse velocity during the lifetime of an RBE (dashed line), while panel (d) displays the number of changes to the transverse direction in which an RBE is moving.

is all the RBEs that display a transverse motion in only one direction and hence move diagonally in a spacetime diagram as seen in the first column of Figure 6. For the second class (B) we took all the RBEs that turn once in their transverse motion, meaning all those that have a single change of direction in Figure 5(d). An example of this behavior is shown in the second column of Figure 6. The remaining RBEs, the ones with several directional changes in their transverse motion in Figure 5(d), are placed in the third class (C) and display the back and forth swaying motion of the example in the third column of Figure 6. We see an increase of the average lifetime with an increase in the number of directional changes, i.e., class C has longer lifetimes than class B which has longer lifetimes than class A.

In addition to these three classifications, we found a fourth class (D) of RBEs. These transcend the groups that are easily identified by Figure 5(d) and are identified from the transverse spacetime diagrams as back and forth swaying regions which are very long lived and faint in contrast with very high contrast patches happening periodically along the faint region. If these high contrast patches are taken as being the real RBEs, they can have a transverse motion which fits into any of the first three classifications. In the right column of Figure 6, an event that is supposed to fit into class A is seen around the 0 s mark in the top panel. This event seem to be a part of a longer lived event which is visible as a faint region that extends backward and forward in time compared to the group 1 event at 0 s and includes other small high contrast patches similar to the 0 s event.

We provide accompanying movies in the online version of the journal to vividly illustrate the different kinds of dynamical evolution patterns. The movies are sequences of Dopplergram images centered on the RBE of interest at $(x, y) = (0, 0)$. The slit for the spacetime diagrams is positioned perpendicular to the main axis of the RBE. We note that the high-frequency jitter of background pattern is caused by remaining local misalignment, caused by seeing, between the sequentially recorded blue and red wings. This slight misalignment is enhanced by the subtraction process when making the Dopplergrams. Example A appears next to an already existing RBE on the left and extends quickly to its full length going toward the left-hand side of the panel. Looking more closely at this example reveals that the full length of the RBE is visible, but faint, before the apparent motion along the RBE coming from the footpoint at the top of the FOV has extended all the way to the maximum length. The full extent of the RBE is progressively gaining higher contrast while the high contrast region propagates away from the footpoint until $t \approx 15$ s after which the RBE rapidly fades. For example B the movie shows an RBE that extends toward the bottom left corner. In the middle of the lifetime of the RBE, the expansion of the RBE structure stops for a short while before continuing to expand. Toward the end, the RBE stops again, and after a short while it starts to fade from the top down and vanishes within a few time steps (also see Figure 9(b)). During its lifetime the RBE displays a small back and forth motion. Example C appears at the bottom in the middle of the panel after a previous RBE has

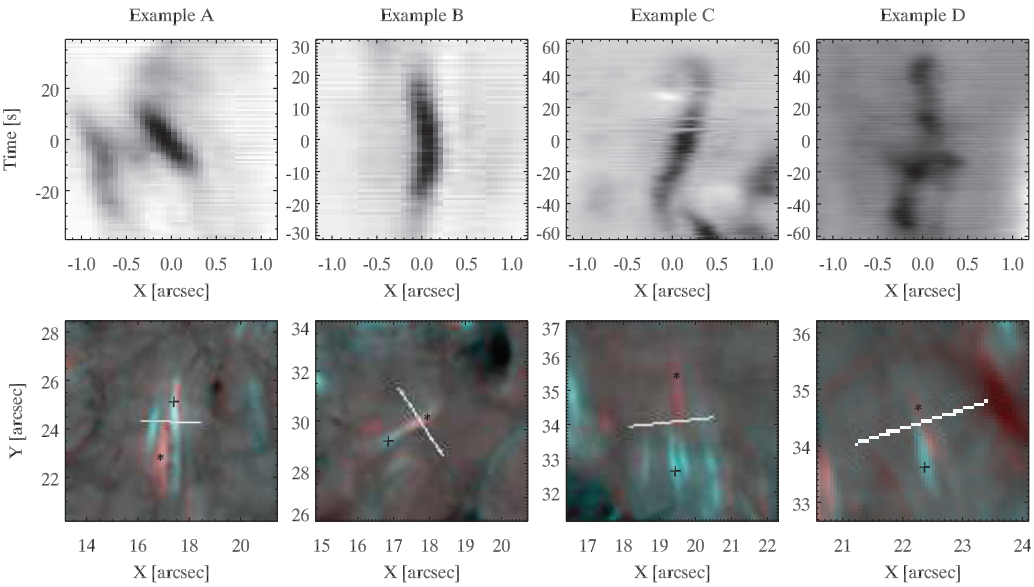

Figure 6. Different transverse behaviors seen in RBEs: example A has a motion in a single transverse direction, example B shows a single turn in the direction of the transverse motion, example C shows several turns in the direction of the transverse motion, example D shows a number of RBEs repeating so close in space and time as to give the impression of being connected in a single longer lived RBE. The shorter lived RBEs that make up an example such as example D can come from each of the other three groups. The top row shows a spacetime diagram taken across the examples. The bottom row shows a composite color image of the examples, where the first timeframe of the RBE is plotted in blue/green while the last time step is plotted in red. The line in the bottom images signifies the slit from which the spacetime diagrams were made and the crosses and stars mark the approximate positions of the RBEs in their first and last frames, respectively, to guide the eye.

(Animations (a, b, c, d) of this figure are available in the online journal.)

almost finished fading away. It then continues to move upward away from its footpoint at a nearly constant pace until, toward the end of its lifetime, the top third vanishes while the remaining RBE structure continues its upward propagation. During its lifetime the RBE also displays a sideways motion that moves mainly toward the right-hand side of the panel. This motion is, however, not constant and seems to start early in the RBE's lifetime and also come to a halt, turning toward the left-hand side near the end of its lifetime. In the movie for example D, it becomes clear that there are four short-lived RBEs recurring in roughly the same location within a timespan of 2 minutes and that the reason for the rather wide second RBE, at $t \approx -15$ s, is due to a fifth short-lived RBE appearing right next to the second RBE. Each of the four RBEs extends to its full length within a couple of seconds moving toward the top of the panel before fading from the FOV almost as rapidly.

4.3.4. Wave Motion in RBEs

From the grouping performed in Section 4.2, all the RBEs in class C were investigated for sinusoidal waves in their transverse motion. This was done by locating the lowest intensity pixel in the slit transverse to the RBE axis at each time step and fitting a sinusoidal curve to these positions. Out of 154 RBEs in class C, as many as 80 could be fitted to a sinusoidal function. The other fits were not acceptable either because of contaminations in the transverse slit from nearby low intensity regions or irregular variations in the intensity of the RBE that ruined the sinusoidal fit.

In Figure 7, a selection of six such sinusoidal fits to the transverse motion is displayed, where the top left example is the same as example C in Figure 6 and the other five are selected from the 80 accepted fits. These fits allowed for a measure of the amplitudes and periods of the transverse motions, which are plotted in the histograms in Figure 8 along with a measure of the velocity amplitude.

The periods vary from 9.7 s up to 168 s with an average of 54 s, while the distribution peaks around 40 s. For the amplitudes, the minimum lies at 21.5 km, which is exactly half the pixel scale of the data set, while the maximum amplitude measured is 129 km with a clear peak of the distribution at 43 km. The velocity amplitudes are calculated in the same way as in Okamoto & De Pontieu (2011), $v = 2\pi\delta x/P$ where v is the velocity amplitude, δx is the amplitude, and P is the period, and were found to lie between 1.5 and 21 km s^{-1} with a peak around 4 km s^{-1} and a median value of 7.5 km s^{-1}.

For the movies accompanying Figure 7, the FOV has been rotated so that the RBE is oriented upward. From the accompanying movies the example in panel (a), which is a zoomed-in version of the movie accompanying example C in Figure 6, displays an almost constant rise phase and a clear transverse motion during its lifetime. Also, the shortening of the RBE structure when the top third vanishes can be seen clearly from this movie. The example in panel (b) appears suddenly around $t \approx -20$ s over a length of approximately $2''$. The fading phase during the end of its lifetime appears to be from the top down and the sideways motion during the middle of its life is clearly discernible. The example in panel (c), on the other hand, extends rapidly from its footpoint and has several high-contrast blobs propagating along the fully extended RBE. This example also shows a clear back and forth sideways motion which from the spacetime diagram turns out to be sinusoidal. In the movie for the panel (d) example we see a long-lived RBE. This RBE first

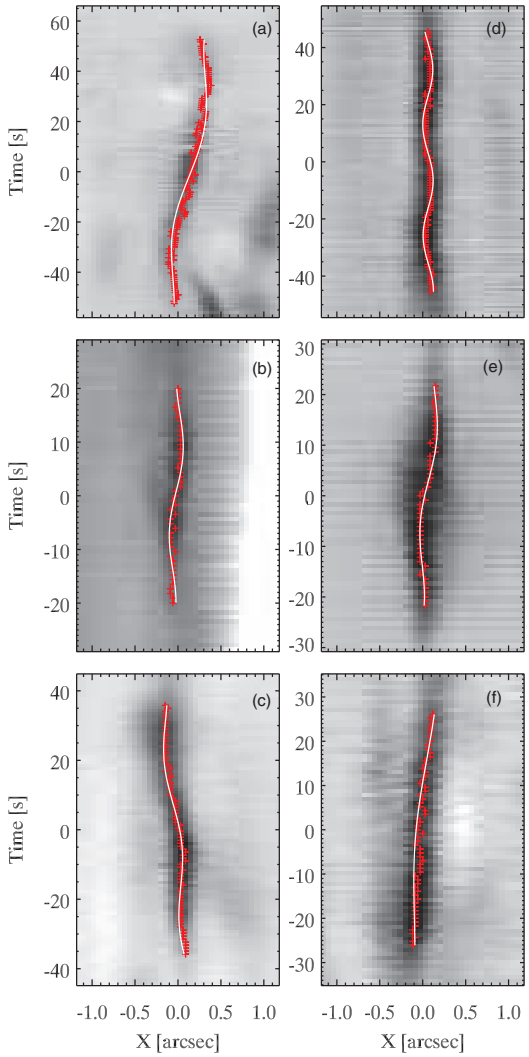

Figure 7. Six examples showing a sinusoidal fit to the transverse motion of an RBE. The red crosses mark the minimum intensity of the RBE at each time step of the lifetime of the RBEs, while the white line is the sinusoidal fit to the minimum intensity points. The underlying images are spacetime diagrams from a slit which is across the RBEs and averaged over 20 pixels in the longitudinal direction of the RBEs.

(Animations (a, b, c, d, e, f) of this figure are available in the online journal.)

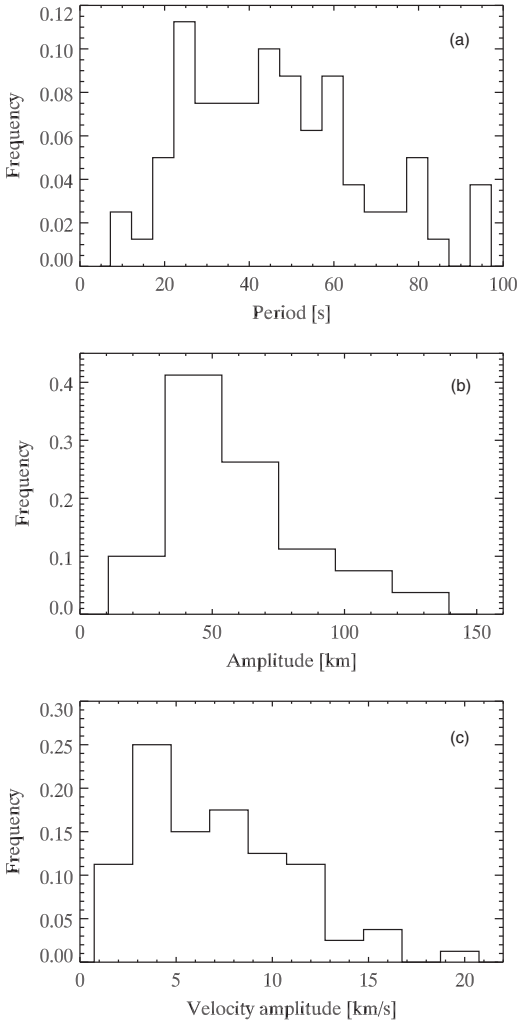

Figure 8. Histograms of the properties of the sinusoidal fit to RBE transverse motions: (a) periods, (b) amplitudes, and (c) velocity amplitudes.

extends to its full length before the entire RBE structure moves upward. The transverse back and forth motion is small but can be seen in the movie. The example in panel (e) grows very fast and reaches its full length within a few time steps. When examined more closely it appears as if sections of the RBE form simultaneously and progressively along the RBE axis creating the illusion of an extreme outward propagation. At the moment the full extent of the RBE has formed, $t \approx -20$ s, it displays a clear sinusoidal shape. As it evolves in time we can see it display the wave motion that is inferred from the spacetime diagram. The example in panel (f) displays a long-period wave motion. This RBE appears in place without any apparent propagation along the axis. There is a small sideways motion seen in this RBE and it fades along its full length simultaneously.

4.3.5. Longitudinal Velocities

In Figure 9, we plot the movement of the top of the RBE with respect to its footpoint for eight different RBEs. The first three examples in the top row are the same RBEs as in Figures 6(A)–(C). The next four examples were chosen from the sample for their stable seeing which made them easier to measure, while the bottom right example is an RBE that appears to become visible along the full length of the RBE within a few seconds. In the few examples studied more closely here, the largest movement of the top of an RBE with respect to its footpoint is about 2 Mm over a lifetime of about 120 s, which

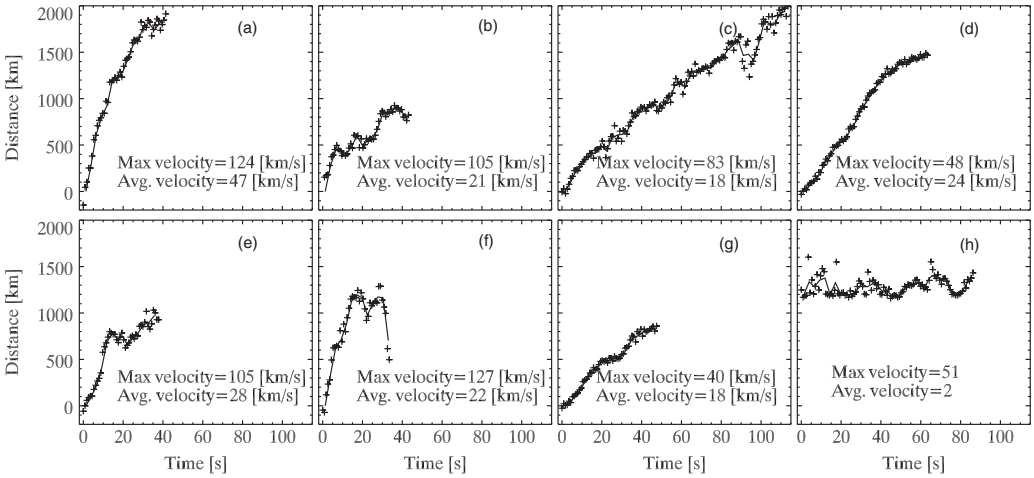

Figure 9. Movement of the top of eight RBEs with respect to a fixed position close to the footpoint of the RBEs.
(Animations (a, b, c, d, e) of this figure are available in the online journal.)

gives an average velocity of 18 km s^{-1} of the top point away from the footpoint. The maximum and average velocities in the panels of Figure 9 are calculated from the trajectory followed by the plotted line which is smoothed over three positions.

The movies accompanying Figure 9 are in the same format as in Figure 6 and examples a, b, and c are discussed in Section 4.3.3. The panel (d) example moves toward the bottom of the panel in the movie, while it is expanding in length in both the downward and upward directions. Toward the end of its lifetime the RBE seems to split into two halves where the top half continues to move downward and fades from the FOV. The bottom half remains stationary for some time before continuing its motion toward the bottom of the panel and at the same time fading from the FOV. In the movie for panel (e) we see an RBE extending toward the bottom from a footpoint close to the center of the panel. At a point toward the end of the RBE's lifetime the top part vanishes and the rest of the RBE continues its movement toward the bottom of the panel. It displays clear sideways motion resembling a sinusoidal wave pattern and fades from the FOV from the footpoint toward the top. The example in panel (f) quickly reaches its full length extending from the footpoint upward in the movie panel. After reaching its maximum length the RBE lingers in this position for a moment before rapidly fading from the FOV giving the impression of an extreme downward motion. Panel (g) shows an example which goes in the direction from left to right. When it appears it extends in both directions while keeping an overall motion to the right, away from the footpoint which lies to the left in the panel. The fading of the RBE happens in the same way, with the top and bottom of the RBE fading simultaneously leaving the middle of the RBE as the last visible part. This RBE appears to consist of several small concentrations. The example displayed in Figure 9(h) has its footpoint located toward the right edge of the panel in the accompanying movie. In this RBE, the top half appears first and is fully formed within seconds. The half closer to the footpoint then forms in the next few seconds, giving the impression of an apparent movement toward the footpoint. When it fades away, this happens from the bottom up and the top part of the RBE is the last to vanish from the FOV.

4.3.6. RBE Evolution in Simultaneous Ca II 8542-Hα Data

In Paper II, RBEs were detected in co-temporal Ca II 8542 and Hα observations. The RBEs were detected in single time steps separately for the two spectral lines. Subsequently, the detected RBEs were automatically connected into multi-frame Ca II 8542 and Hα RBEs. Finally, for a number of these multi-frame RBEs, it was possible to connect the Ca II 8542 and Hα chains. For these linked multi-frame RBEs, it is possible to study the temporal evolution in two different spectral lines.

We find that for most of these automatically linked multi-frame RBEs, the RBE appears first in Ca II 8542 or simultaneously in both lines. Manual inspection of the few cases where the automated detection found the RBE in Hα first revealed that there is always an associated Ca II 8542 signal, but it is too faint or small scale to be identified by the automated method.

Figure 10 shows an example of the evolution of a multi-frame RBE from its initial detection in Ca II 8542 in panel 3, left column, to when it fades from the FOV in Hα in panel 8, right column. We focus on the RBE farthest to the right, centered on $(x, y) \approx (40, 40)$ at $t = 47$ s. The RBE in this example was not detected in Hα until panel 5, which is at least 20 s after the initial detection in Ca II 8542. Also, the RBE is already fading away from the FOV in Ca II 8542 in panel 6, and is only barely visible in 7 and 8, whereas it is still strong in Hα for another two time steps, ∼20 s.

Figure 10 also shows very clearly that the Hα part of the RBE is located farther away from the origin of the RBE when compared to the Ca II 8542 part, with the origin being toward the left-hand side of the images where the data set contains a region of concentrated magnetic fields (see Paper II).

5. DISCUSSION

5.1. Quiet-Sun RBEs

The studies of Papers I and II have so far been conducted in coronal hole regions where the magnetic field is more unipolar. In this study, we have focused on a region with quiet-Sun

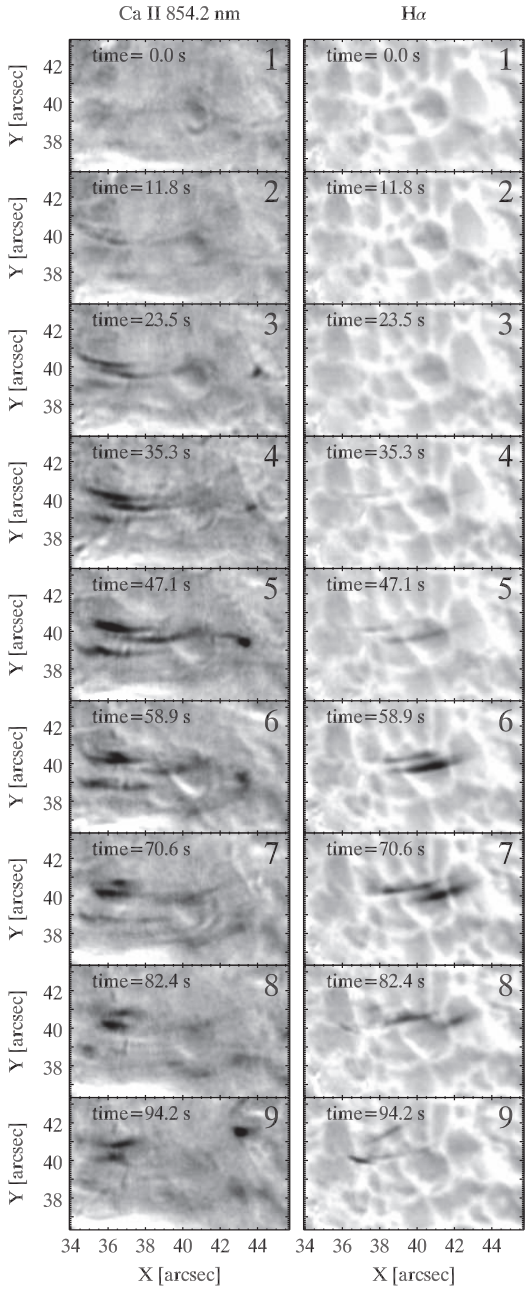

Figure 10. RBE found in both Ca II 8542 and Hα from the 2008 June 27 observations. Ca II 8542 images taken at the blue wing position of 20 km s^{-1} are in the left column with their simultaneous counterpart Hα images from the blue wing position of 45 km s^{-1} in the right column.

(An animation of this figure is available in the online journal.)

conditions, which are the conditions that on average cover 70%–80% of the solar surface (Priest 1982).

In Paper II, it was found that Hα RBEs in a coronal hole had Doppler velocities between 30 and 50 km s^{-1}. We see from our quiet-Sun observations that the range of Doppler velocities in our data match very well with what is seen in coronal holes, only shifted to lower values.

The Doppler widths seem to undergo the same effect as the Doppler velocities when moving from a coronal hole to the quiet Sun. While the range of Doppler widths is more or less the same as for the coronal hole in Paper II, it is shifted toward lower values. These measurements of Doppler velocity and Doppler widths serve to characterize the spectral profiles of RBEs. The Doppler velocity is related to the physical motion of plasma in the RBE and increased Doppler width could be related to enhanced temperatures or, alternatively, signs of unresolved substructures with varying velocities. However, we caution against a direct physical interpretation of these measurements: only through detailed modeling of the radiation transport in the atmospheres of these structures can knowledge about the exact physical conditions be obtained.

While the Doppler velocities and widths are lower in the quiet Sun than in a coronal hole, the physical lengths of RBEs do not seem to be very different for the two target area types. The only differences are that we find slightly shorter RBEs in our quiet-Sun data and a shift in the peak of the distribution to around 2.3 Mm instead of at 2.6 Mm, which can be attributed to the automated detection routine being allowed to search for these shorter events.

It is possible that all these differences are naturally occurring as a result of the intrinsic differences in coronal hole and quiet-Sun magnetic field configurations. While coronal holes have predominantly unipolar fields and vertical field lines, the quiet-Sun harbors mixed polarity fields with more horizontal field lines and closed loops. The difference in the magnetic field orientation might result in a different combined effect of the three types of spicule motion, field-aligned flow, transverse swaying, and torsional motion (De Pontieu et al. 2012). For example, for more inclined RBEs observed at disk center, the field-aligned flow would only have a small component along the line of sight, so that the more varying effects of swaying and torsional motions could become more dominant in the observed Doppler properties. In addition, it is possible that the different viewing angle, away from disk center (viewing angle $\mu = 0.84$) for the coronal hole of Paper II and at disk center for the quiet Sun here, is contributing to the different values for the RBE properties in the two data sets.

Using the recurrence rate of one RBE per 500 s from De Pontieu et al. (2011), Klimchuk (2012) dismissed type II spicules as a sufficient source of hot plasma and energy for heating coronal loops and their importance for the temperature structure in the corona. We now have data sets with a much higher cadence than before and we find average recurrence times around the magnetic network where RBEs appear of 84 s and a minimum recurrence time of 4.3 s in the densest regions. Our results indicate that the conclusions of Klimchuk (2012) are unwarranted, and also highlight the dangers of using simplified models and poorly determined observational characteristics.

5.2. Spatial Dependence of RBE Properties

Figure 3 shows three very different RBE examples of how the Doppler velocity and Doppler width changes with the position along the RBE. In Paper I, the large-scale FOV picture was

that RBEs in general would accelerate outward from their footpoints and this view was confirmed by examining single RBEs that behaved similar to the first example in Figure 3. In Paper II, this general large-scale FOV picture of having RBE Doppler velocities increasing outward from their footpoints was confirmed, but it was noted that a significant number of RBEs exist that display a more erratic variation in their Doppler properties. When making similar maps of the variation of Doppler properties along RBEs for our quiet-Sun observations, we see a more complicated mixture of longitudinal variations (see Figure 1). There are clear regions where the top of the RBEs is at a higher Doppler velocity and width than at the footpoint, but at the same time the exact opposite behavior can be seen in other regions of the FOV, where the Doppler velocity and width are clearly lowest farthest away from the footpoints. When examining the RBEs individually we see that both of these behaviors are quite normal and there are almost equal amounts of RBEs with Doppler velocities and widths increasing and decreasing away from the footpoints. In addition to RBEs that show monotonic increasing and decreasing Doppler properties along their axes, there are others that display a much more complex configuration of Doppler velocities and widths. These RBEs seem to have a change in their velocity in different locations along their lengths and may even display several changes both up and down in velocity in a single timeframe, as seen in the third example of Figure 3. Although the Doppler velocity and width in general seem to be changing simultaneously and with the same trend, there are cases where the Doppler width changes more or less independently from or opposite of the Doppler velocity. This is illustrated in Figure 2(d) where the Doppler velocity versus Doppler width has a looser correlation than for the coronal hole of Paper II where there is a trend of larger Doppler width for increased Doppler velocity.

When examining the maps of Figures 1(c) and (d), we see no apparent large-scale trend in the spatial variations of the Doppler velocities and Doppler widths of RBEs. At the same time, we note the absence of noise in the large-scale pattern of Doppler variations. If the Doppler velocity and width were completely independent of the position along the RBE, these maps would have a different appearance. There is clearly more scatter in the large-scale pattern than in the corresponding maps for the coronal hole targets of Papers I and II (cf. Figure 12 in Paper I and Figure 6 in Paper II), but the pattern in the color distribution is very unlike that of a random distribution. It is possible that systematic trends in the variation of the Doppler properties along the RBE axis are hidden by the more complicated magnetic field geometry of the quiet Sun with the presence of more mixed polarity fields and more associated inclined and curved field lines. In this less orderly configuration, large-scale trends would be harder to discern in maps like Figure 1. Moreover, we should realize that the combined effect of the three types of motions in spicules, field-aligned flow, swaying, and torsional motion, might be very different for varying angles between the line of sight (LOS) and the magnetic field configuration. Horizontal fields observed at disk center could give rise to more of the torsional motions showing up in the RBE signal, whereas the more vertical field lines at upper chromospheric heights of a coronal hole may show more of the field-aligned motion or outflow of material. We realize that the major unknown parameter in our analysis is the knowledge of the exact orientation of each RBE. Measurements of the magnetic field vector by means of various Stokes diagnostics would be a possible approach to becoming conclusive on the longitudinal variation of the Doppler properties of RBEs.

5.3. RBE Dynamics from Temporally Resolved Data

5.3.1. Improved Lifetimes

The first measurements of the lifetimes of type II spicules yielded values between 10 and 110 s (De Pontieu et al. 2007c), where the 10 s threshold was given by the cadence of the data set in which this new type of spicule was discovered. The extensive and systematic study of Pereira et al. (2012) employed automatic detection on a larger sample of type II spicules and established a typical lifetime between 50 and 150 s with a peak in the distribution around 80 s. For their disk counterparts, the lifetimes were estimated from a manual selection of 35 RBEs and measured to range between 10 and 70 s, with a few examples displaying lifetimes of up to 140 s (Paper I). An automated method on a much larger sample (453) established a range of 20–150 s (Paper II) which was in agreement with the Pereira et al. (2012) results.

For all these studies, the determination of the minimum lifetime of type II spicules was limited by the cadence of the observations. Here, we resolve this limitation by analyzing a much faster cadence data set (0.88 s) and we make further improvements by employing a secondary manual measurement based on spacetime diagrams across the RBEs. From Figure 4, we see that when measuring the lifetimes in the transverse spacetime diagrams, we find that RBEs seem to have a lower limit to their lifetimes at approximately 5 s, which is much higher than the cadence of the data set. Lifetimes measured from the automated method alone lower the threshold to the cadence of the data set and closer evaluation concluded that this method was not reliable for these kinds of measurements. The lower threshold of lifetimes of RBEs at 5 s that is found here is likely the real minimum lifetime of RBEs in our data set. We find a range of lifetimes between 5 and 60 s with an average of 30 s, which indicates that data sets with a slow cadence will easily connect recurring RBEs in high-density regions into longer lived RBEs. We remark that these numbers should not be interpreted as "the" lifetime of RBEs/type II spicules as we only have observations from one wing position. The RBEs can be shifted out of the observed passband by acquiring higher or lower Doppler velocities due to field-aligned flows, swaying, and torsional motions, and continue their evolution out of range of the diagnostics. This could be an explanation for the lower average lifetime we find for RBEs as compared to type II spicules at the limb. The latter were measured in *Hinode* Ca H intensity which is insensitive to these kinds of changes in the Doppler shift.

5.3.2. Transverse Motions

In Paper I, manual measurements of 35 RBEs resulted in transverse velocities ranging from 0 to 20 km s^{-1} with an average of 8 km s^{-1}, whereas Paper II, employing an automated method on a much larger sample for measuring multi-frame RBEs, found a range of 0–15 km s^{-1} with an average of 5 km s^{-1}. By checking the Paper I data set with the automated detection method, the authors of Paper II concluded that the discrepancy of the transverse velocities were due to the difference in cadence allowing for the detection of higher transverse velocities in the Paper I data set which had a cadence which was twice as fast as the Paper II data set. It became clear that the temporal resolutions of these studies were not sufficient to be conclusive in these

measurements which motivated us to pursue the acquisition of the high cadence data set analyzed here.

The average transverse velocity of RBEs in the high-cadence data set is comparable to the Paper I result with a peak in the distribution comparable to that in Paper II. What is different, however, is the increase in the distribution toward higher velocities; see Figure 5(c). The distribution of the maximum transverse velocity in the lifetime of RBEs is also found to be shifted to higher velocities and is now in close agreement with the corresponding measurements for type II spicules at the limb by Pereira et al. (2012) and the original measurements of De Pontieu et al. (2007b).

For the maximum displacement of the two extreme transverse positions we see a smaller difference between the high-cadence data and Paper II (see Figure 5(a)). There is an increase in the number of RBEs displaying maximum transverse displacements of 200 km and more, which is a direct result of having a higher cadence data set where it is much easier to follow the RBEs with a very rapid transverse motion covering a larger distance.

We actually see a slight lowering of the integrated transverse displacement (Figure 5(b)) in comparison with the lower cadence data of Paper II. This can be attributed to the employment of manual measurements in our high-cadence data sets compared to relying on the detected trajectories of the multi-frame RBEs in the low-cadence data set. Relying only on the detected trajectories resulted in a significantly higher integrated displacement due to noise in the measurements. The measurements of transverse displacement of RBEs are in close agreement with the corresponding measurements for type II spicules at the limb (Pereira et al. 2012; De Pontieu et al. 2007b).

5.3.3. Grouping of RBEs Based on Transverse Spacetime Diagrams

With the extremely fast cadence of the 2011 May 5 data set, it is possible to follow the transverse motion of RBEs in time. From a manual inspection of all spacetime diagrams taken across the RBEs we saw a pattern of three different transverse behaviors, where the most common transverse motion is seen going in a single direction from one extreme position to the other within the lifetime of the RBE. As the second most common transverse motion we found a single back and forth swaying motion which is characterized by one change in direction. This behavior is not necessarily going from one extreme to the other and back again to its starting position, although that seems to be the case in example B in Figure 6. The third behavior of the transverse motion seen in our data set can be classified as a proper back and forth swaying motion, where the direction of the transverse motion changes several times. In Figure 6(C), the RBE is seen to have a dominant transverse direction toward the right while exhibiting several turns in its transverse motion throughout its lifetime. There are also examples that display a back and forth swaying motion while seemingly being centered around a middle point and hence not displaying a dominant transverse direction. Even though these groups appear to have different behavior, these apparent differences could well be caused by different lifetimes and periods and are thus not necessarily a sign that the different subclasses are caused by different mechanisms.

In addition to the three clear-cut groups of RBEs, we also observed a fourth type in our transverse spacetime diagrams that consists of several repeating RBEs appearing so close in time and space as to give the impression of a longer lived RBE with concentrated blobs when examined in a spacetime diagram. This fourth class, example D in Figure 6, supports the idea that the transverse swaying motions are in some sense independent of the formation of the RBEs. That is, the waves are volume filling, with the RBEs occasionally tracing part the field lines that are affected. This is further supported by the observation that the lifetimes of the different classes are on average increasing, i.e., we see longer lifetimes for class C than for class A which shows no change in direction. Based on numerical simulations, De Pontieu et al. (2007b) proposed this scenario to interpret the swaying motions of type II spicules at the limb as tracers of Alfvénic waves that permeate the chromosphere. This scenario was later confirmed in AIA observations by McIntosh et al. (2011).

5.3.4. Wave Motion in RBEs

Type II spicules were recently found to undergo three types of motion: a field-aligned flow along the spicule axis, transverse swaying, and a torsional motion around the axis (De Pontieu et al. 2012). The transverse swaying in spicules was closely investigated by Okamoto & De Pontieu (2011), who concluded that they carry upward and downward propagating waves, as well as apparently standing waves with very high phase speeds. We find that for part of the RBEs of group C, the sideways motion can be fitted by a sinusoidal function (Figure 7). The periods and amplitudes of the these sinusoidal waves (Figure 8) correspond well to those found in type II spicules (Okamoto & De Pontieu 2011).

In their study of transverse motions in RBEs Yurchyshyn et al. (2012) also found a sinusoidal behavior. With periods averaging 90 s and amplitudes of 200 km, their results are not directly comparable to those found here, but with a cadence of 10 s it is likely that the RBEs studied were of the more extreme type when it comes to at least lifetimes and possibly also transverse movement. Because of the lower cadence of their data set it cannot be excluded that the long-lived RBEs observed are several distinct RBEs identified as one due to their superposition in time. However, it is clear that both type II spicules and RBEs display transverse sinusoidal wave motion.

5.3.5. Longitudinal Velocities

Type II spicules have high apparent rising velocities, 50–150 km s^{-1} (De Pontieu et al. 2007c). Pereira et al. (2012) examined type II spicules in both coronal holes and quiet-Sun regions, and found the maximum velocities of these spicules to typically lie between 40 and 100 km s^{-1}, with a few cases going beyond 150 km s^{-1}. They also found that the quiet-Sun spicules had a lower maximum velocity on average and a sharper drop-off after 100 km s^{-1} than coronal hole spicules.

We tracked the movement of the top of a number of RBEs and found maximum velocities from approximately 40 to 125 km s^{-1}. We also see that the top of an RBE does not move away from the footpoint linearly or exponentially, which would be expected if the RBEs would have a constant or increasing velocity as they propagate away from the footpoint. In fact, the behavior of the top part of the RBE is somewhat erratic and complex, with the RBE seemingly coming to a halt or even retreating for a short period of time before continuing its motion away from the footpoint. This cannot be explained by a relatively simple (in terms of spatio-temporal variation) mass motion along an outwardly expanding jet alone. Full understanding of such complex behavior will likely have to wait for detailed theoretical modeling of these jets. However, it is clear that the presence of time-varying torsional disturbances that propagate at high speeds can play an important role in understanding complex apparent motions seen in observations at

a fixed wavelength. Given the uncertainty and variations across the FOV of the angle between the magnetic field and the LOS, our Doppler observations are likely sensitive to a varying mix of field-aligned motions and torsional motions. The combination could well provide an explanation for the often erratic apparent motions observed by means of Doppler diagnostics in the wings of the Hα and Ca II 8542 spectral lines. The presence of very high phase speeds, as detected by Okamoto & De Pontieu (2011) and caused mostly by standing waves, can then provide a natural explanation for the sometimes sudden appearance of an RBE over the whole length within a few time steps.

In 1 s cadence red wing Hα IBIS observations of a region near the limb, Judge et al. (2012) reported chromospheric thread-like structures appearing and disappearing along the entire length within a few seconds and seemingly out of nowhere. They interpreted this observation as indirect evidence for the existence of plasma sheets in the solar chromosphere (see Judge et al. 2011). We confirm the observation of a sudden appearance for some RBEs in our data; see Figure 9(h). In their complex spectrum of dynamical behavior, we see some RBEs appear as thin threads without a clear rise phase in a few time steps. In contrast to Judge et al. (2012), we interpret this sudden appearance in the context of torsional modulation and high phase speeds of standing waves in spicules (as conclusively shown by Okamoto & De Pontieu 2011), rather than the superposition effects in two-dimensional sheet-like structures.

5.3.6. RBE Evolution in Simultaneous Ca II 8542-Hα Data

In Paper II, it was found that Ca II 8542 RBEs are located closer to the anticipated footpoints in the magnetic network regions than Hα RBEs and that Hα RBEs are a continuation of the Ca II 8542 RBEs. Here, we extended the analysis of the 2010 June 27 data set to study the Ca II 8542-Hα connection in the temporal evolution of RBEs. We found that for all the RBEs detected in both spectral lines, the RBE appeared first in Ca II 8542 or simultaneously in both lines. We could not identify cases of an RBE appearing first in Hα without an associated RBE signal in Ca II 8542.

The observation that some RBEs appear first in Ca II 8542 before becoming visible in Hα suggests that for these RBEs the origin of the jet is located in the lower chromosphere, below the sampling heights of the Hα line. For the RBEs appearing in both lines simultaneously, the origin must be located relatively higher in the atmosphere.

In the example in Figure 10, we see that the Ca II 8542 part of an RBE appears at least 20 s before the RBE becomes visible in Hα. It also vanishes from the FOV in Ca II 8542 earlier than in Hα. For this case, Ca II 8542 shows the RBE closer to its origin and early in its life, while Hα shows us the later stages of the RBE's life, further away from its footpoint and apparently at greater height. Progressively fading first in Ca II 8542 before Hα could also be related to heating of the spicule. This observation is interesting in connection with the work of De Pontieu et al. (2011) who found that the fading of *Hinode* Ca H spicules is directly linked to features appearing at transition region temperatures in He II 304 Å and sometimes even appearing in coronal diagnostics.

6. CONCLUSION

We addressed various aspects of the temporal evolution of RBEs by analyzing a number of high-quality data sets: a dual line Hα+Ca II 8542 timeseries, a spectrally resolved Hα series, and a coarsely sampled, extremely high-cadence series. Our analysis adds more weight to the interpretation of RBEs being the disk counterpart of type II spicules, for example from the close agreement in transverse speed and displacement when compared to type II spicules at the limb (Pereira et al. 2012) and from the agreement between sinusoidal wave parameters in RBEs we find here and those found in type II spicules at the limb (Okamoto & De Pontieu 2011). At the same time, the picture of the dynamical behavior of RBEs and spicules that arises from these kind of data sets is a very complex one. Even in the extremely high-cadence timeseries, specially tailored to resolve the dynamics at the shortest timescales, the variation in temporal behavior is bewildering. We see RBEs move sideways with velocities up to 55 km s^{-1}, while others are hardly displaced at all. Some RBEs live as short as 5 s, while others live for more than 2 minutes. Some RBEs have a distinct rise phase with velocities up to 127 km s^{-1}, some rise with velocities below 40 km s^{-1}, and others appear suddenly along the full length within a few seconds without a distinct rise. In dense regions, we see RBEs appear in rapid succession, sometimes as a short-lived apparent densification of a faint background structure.

Now that spectroscopic data of spicules at the limb have established that spicule dynamics is governed by three different types of motion—field-aligned flows, transverse swaying, and torsional motion (De Pontieu et al. 2012)—we realize that the complex appearance of RBEs has to be interpreted within this three-fold dynamical framework. Taking into account these three different types of motion, and the observed presence of apparent standing waves in type II spicules, the sudden appearance of RBE features at extremely high phase speeds is no longer as difficult to explain as suggested by Judge et al. (2012 who have used this observational finding to propose a sheet-like nature of spicules). While the extreme cadence of the fast data set was useful to resolve RBEs temporally, it is clear that the sparse spectral sampling is insufficient to fully characterize the RBEs' evolution. Significant changes in Doppler shift due to swaying or torsional modulation require denser spectral coverage. The measurement of a minimum lifetime of 5 s at one fixed Hα wavelength indicates that the observer has at least a few seconds to build up a more extended spectral sampling, so the characterization of RBE Doppler modulation appears to be within reach of present-day instrumentation.

The Swedish 1 m Solar Telescope is operated by the Institute for Solar Physics of the Royal Swedish Academy of Sciences in the Spanish Observatorio del Roque de los Muchachos of the Instituto de Astrofísica de Canarias. B.D.P. was supported through NASA contracts NNG09FA40K (IRIS), NNX11AN98G, and NNM12AH46G. We thank Jaime de la Cruz Rodrígues and Eamon Scullion for their help during the observations. This research has made use of NASA's Astrophysical Data Systems.

REFERENCES

Beckers, J. M. 1968, SoPh, 3, 367
De Pontieu, B., Carlsson, M., Rouppe van der Voort, L. H. M., et al. 2012, ApJL, 752, L12
De Pontieu, B., Erdélyi, R., & James, S. P. 2004, Natur, 430, 536
De Pontieu, B., Hansteen, V. H., Rouppe van der Voort, L., van Noort, M., & Carlsson, M. 2007a, ApJ, 655, 624
De Pontieu, B., McIntosh, S. W., Carlsson, M., et al. 2011, Sci, 331, 55
De Pontieu, B., McIntosh, S. W., Carlsson, M., et al. 2007b, Sci, 318, 1574
De Pontieu, B., McIntosh, S. W., Hansteen, V. H., et al. 2007c, PASJ, 59, 655
De Pontieu, B., McIntosh, S. W., Hansteen, V. H., & Schrijver, C. J. 2009, ApJL, 701, L1

Hansteen, V. H., De Pontieu, B., Rouppe van der Voort, L., van Noort, M., & Carlsson, M. 2006, ApJL, 647, L73
Henriques, V. M. J. 2012, A&A, 548, A114
Judge, P. G., Reardon, K., & Cauzzi, G. 2012, ApJL, 755, L11
Judge, P. G., Tritschler, A., & Chye Low, B. 2011, ApJL, 730, L4
Klimchuk, J. A. 2012, JGRA, 117, A12102
Langangen, Ø., De Pontieu, B., Carlsson, M., et al. 2008, ApJL, 679, L167
Martínez-Sykora, J., Hansteen, V., & Moreno-Insertis, F. 2011, ApJ, 736, 9
McIntosh, S. W., de Pontieu, B., Carlsson, M., et al. 2011, Natur, 475, 477
Okamoto, T. J., & De Pontieu, B. 2011, ApJL, 736, L24
Pereira, T. M. D., De Pontieu, B., & Carlsson, M. 2012, ApJ, 759, 18
Priest, E. R. 1982, Solar Magneto-hydrodynamics (Dordrecht: Reidel)
Rouppe van der Voort, L., Leenaarts, J., de Pontieu, B., Carlsson, M., & Vissers, G. 2009, ApJ, 705, 272
Scharmer, G. B., Bjelksjo, K., Korhonen, T. K., Lindberg, B., & Petterson, B. 2003a, Proc. SPIE, 4853, 341
Scharmer, G. B., Dettori, P. M., Lofdahl, M. G., & Shand, M. 2003b, Proc. SPIE, 4853, 370
Scharmer, G. B., Narayan, G., Hillberg, T., et al. 2008, ApJL, 689, L69
Sekse, D. H., Rouppe van der Voort, L., & De Pontieu, B. 2012, ApJ, 752, 108
Sterling, A. C. 2000, SoPh, 196, 79
Suematsu, Y., Wang, H., & Zirin, H. 1995, ApJ, 450, 411
Tsiropoula, G., Tziotziou, K., Kontogiannis, I., et al. 2012, SSRv, 169, 181
van Noort, M., Rouppe van der Voort, L., & Löfdahl, M. G. 2005, SoPh, 228, 191
Vissers, G., & Rouppe van der Voort, L. 2012, ApJ, 750, 22
Yurchyshyn, V., Kilcik, A., & Abramenko, V. 2012, arXiv:1207.6417
Zhang, Y. Z., Shibata, K., Wang, J. X., et al. 2012, ApJ, 750, 16

Paper III

Interplay of Three Kinds of Motion in the Disk Counterpart of Type II Spicules: Up-flow, Transversal and Torsional Motions

Sekse, D.H., Rouppe van der Voort, L., De Pontieu, B. and Scullion, E.M.

Accepted by ApJ (2013)

Draft version April 8, 2013
Preprint typeset using LaTeX style emulateapj v. 11/10/09

INTERPLAY OF THREE KINDS OF MOTION IN THE DISK COUNTERPART OF TYPE II SPICULES: UP-FLOW, TRANSVERSAL AND TORSIONAL MOTIONS

D. H. Sekse[1], L. Rouppe van der Voort[1], B. De Pontieu[2], and E. Scullion[1]
[1]Institute of Theoretical Astrophysics, University of Oslo, P.O. Box 1029 Blindern, N-0315 Oslo, Norway and
[2]Lockheed Martin Solar & Astrophysics Lab, Org. A021S, Bldg. 252, 3251 Hanover Street Palo Alto, CA 94304 USA
Draft version April 8, 2013

ABSTRACT

Recently, it was shown that the complex dynamical behaviour of spicules has to be interpreted as the result of simultaneous action of three kinds of motion: (1) field aligned flows, (2) swaying motions, and (3) torsional motions. We use high-quality observations from the CRisp Imaging SpectroPolarimeter at the Swedish 1-meter Solar Telescope to investigate signs of these different kinetic modes in spicules on the disk. Earlier, rapid blue-shifted excursions (RBEs), short-lived absorption features in the blue wing of chromospheric spectral lines, were identified as the disk counterpart of type II spicules. Here we report the existence of similar absorption features in the *red* wing of the Ca II 8542 and Hα lines: rapid *red*-shifted excursions (RREs). RREs are found over the whole solar disk and are located in the same regions as RBEs: in the vicinity of magnetic field concentrations. RREs have similar characteristics as RBEs: they have similar lengths, widths, lifetimes, and average Doppler velocity. The striking similarity of RREs to RBEs implies that RREs are a manifestation of the same physical phenomenon and that spicules harbour motions that can result in a net red-shift when observed on-disk. We find that RREs are less abundant than RBEs: the RRE/RBE detection count ratio is about 0.52 at disk center and 0.74 near the limb. We interpret the higher number of RBEs and the decreased imbalance towards the limb as an indication that field-aligned up-flows have a significant contribution to the net Dopplershift of the structure. Most RREs and RBEs are observed in isolation but we find many examples of parallel and touching RRE/RBE pairs which appear to be part of the same spicule. We interpret the existence of these RRE/RBE pairs and the observation that many RREs and RBEs have varying Dopplershift along their width as signs that torsional motion is an important characteristic of spicules. The fact that most RBEs and RREs are observed in isolation agrees with the idea that transversal swaying motion is another important kinetic mode. We find examples of transitions from RRE to RBE and vice versa. These transitions sometimes appear to propagate along the structure with speeds between 18 and 108 km s^{-1} and can be interpreted as the sign of a transverse (Alfvénic) wave.
Subject headings: Sun: atmosphere — Sun: chromosphere — Sun: corona

1. INTRODUCTION

The solar chromosphere is a highly dynamical atmospheric layer dominated by numerous small-scale structures. At the solar limb, some of these small-scale dynamical events can be seen as thin jet-like features protruding from above the photosphere to heights of 10 Mm or more. These jets are called spicules and have been known for more than a century, see Beckers (1968) for a review of the older literature, and e.g., Tsiropoula et al. (2012) for a more recent review. De Pontieu et al. (2007a) discovered the existence of a new class of spicules that differed from the known spicules by displaying only upwards motion, shorter lifetimes and higher velocities. From an extensive set of data sets, Pereira et al. (2012a) determined typical velocities for these so-called type II spicules to range between 30–110 km s^{-1}, and lifetimes between 50–150 s. The "other" type of spicules, or type I spicules, have typical lifetimes of 150–400 s, and show rising and falling phases in parabolic trajectories with maximum rise velocities ranging between 15–40 km s^{-1}. Type II spicules are the most abundant type which dominate both quiet Sun and coronal hole conditions, only in active regions type I spicules dominate (De Pontieu et al. 2007a; Pereira et al. 2012a). A recent investigation by Pereira et al. (2012b) demonstrated that only modern observational techniques can provide the required spatio-temporal resolution that is necessary to detect these highly dynamical type II spicules and that bad seeing and technical limitations precluded earlier identification from the ground-based "classical" observations.

Short lifetimes and high velocities are only two of several factors that contribute to make spicules notoriously difficult to observe: vigorous sideways and swaying motion add to its dynamical complexity but the foremost facet that impedes unambiguous and continuous detection throughout a spicule's lifetime is line-of-sight confusion. At and near the limb, the observer's line-of-sight crosses a large number of spicules that combine to a dense forest, in some spectral diagnostics almost a diffuse blanket, from which it is nearly impossible to trace all phases of a single spicule's evolution. For this reason, the identification of the disk counterpart of type II spicules was regarded as crucial for making progress on the determination of its nature and driving mechanism. Langangen et al. (2008) and Rouppe van der Voort et al. (2009, Paper I) linked so-called "rapid blue-shifted excursions" (RBEs), short-lived and spatially elongated spectral asymmetries in the blue wings of the chromospheric Ca II 8542 and Hα lines, in on-disk observations

to the type II spicules at the limb. Sekse et al. (2012, Paper II) and Sekse et al. (2013, Paper III) greatly expanded on the statistics of these events and reinforced the interpretation of RBEs as the disk counterparts of type II spicules.

Besides being one of the main constituents of the chromosphere, interest in type II spicules is motivated by their potential to play an important role in providing mass and energy to the upper solar atmosphere. Their characteristic sideways swaying motion has been interpreted as a sign that the chromosphere is permeated with Alfvénic waves with sufficient energy to heat the quiet Sun corona and accelerate the solar wind (De Pontieu et al. 2007b). Studies by De Pontieu et al. (2009) and De Pontieu et al. (2011) provided evidence that type II spicules play an important role in mass loading and heating of the corona. The characteristic rapid fading observed in the *Hinode* Ca H observations has been interpreted as a sign of heating of the structure to temperatures that leaves no significant opacity in the observation passband.

As mentioned above, type II spicules display a complex dynamical behaviour. Besides apparent rising velocities that vary over a range of more than 100 km s^{-1}, many are displaced transversally over distances up to 1 Mm and may reach transverse velocities up to 60 km s^{-1} (Pereira et al. 2012a). Oscillatory swaying motion has been observed with amplitudes of order 10–20 km s^{-1} and periodicities of 100–500 s (De Pontieu et al. 2007b). Okamoto & De Pontieu (2011) found a mix of upward and downward propagating as well as standing waves in a large number of spicules in high-cadence *Hinode* Ca H limb observations. Similar periods and amplitudes were found for Hα RBEs at disk center in Paper III. Suematsu et al. (2008) reported that some spicules appear as double and sometimes even multiple threads with evidence of spinning motion. Judge et al. (2012) reported the striking observation of spicule-like features that suddenly appear along their full length in extremely high-cadence Hα wing observations close to the limb. Paper III reported similar behaviour for RBEs at disk center. If upward moving plasma were the only motion in spicules, sudden appearance would imply extreme propagation speeds in excess of several thousand km s^{-1}. However, De Pontieu et al. (2012) established that besides field-aligned flows and swaying motions, a third type of motion, torsional motions of order 25–30 km s^{-1} are governing the dynamics of spicules. When torsional motions are considered, the sudden appearance of spicule-like features in fixed-wavelength imaging can be explained as the result of rotational Dopplershift into the observed passband (Paper III). The observed omni-presence of torsional motion in spicules implies that the combined action of all three modes of motion needs to be considered when interpreting Doppler signals to estimate the transport of plasma and Alfvénic wave energy by spicules through the solar atmosphere. The ubiquity of torsional motion may also have important implications for determining the production mechanism of spicules and suggest that they may be an important agent for transporting helicity to the upper solar atmosphere.

In this study, we continue the work by De Pontieu et al. (2012) and Papers I–III to investigate signs of torsional motions in the disk counterpart of type II spicules. The work of De Pontieu et al. (2012) was based on various slit and imaging spectroscopic data sets at the limb. Juxtaposition of the three kinetic modes was observationally established by curved spectral profiles in off-limb Ca II H λ-t diagrams, and tilted spectral profiles in λ-x diagrams of the Ca II H, Hα, and Ca II 8542 spectral lines. In addition, the striking similarity of rows of on-disk and near-limb absorption features in red and blue wing samplings was noted as an important indication of the presence of large-amplitude transversal velocities. In the blue wing, these absorption features are comparable to RBEs observed closer to disk center. Observed in the red wing, these absorption features are more appropriately referred to as "rapid *red*-shifted excursions", or *RREs*. Here we report the presence of RREs over the whole solar disk and characterise their properties.

2. OBSERVATIONS AND DATA REDUCTION

The observations were obtained at the Swedish 1-m Solar Telescope (SST, Scharmer et al. 2003a) on La Palma using the CRisp Imaging SpectroPolarimeter (CRISP, Scharmer et al. 2008) instrument. The CRISP instrument is based on a dual Fabry-Pérot interferometer (FPI) and contains three high-speed low-noise CCD cameras which operate at a frame rate of 35 frames per second with an exposure time of 17 ms per frame. All three cameras are located behind the CRISP pre-filter and are synchronised by an optical chopper. Two of the cameras are also positioned behind the FPI and a polarising beam splitter, while the third camera, which acts as an anchor channel for image processing, is located before the FPI. CRISP has a field of view (FOV) of approximately 61″×61″and an image scale of 0.″0592/pixel. Fast wavelength tuning (<50 ms) is possible between any two positions within the spectral region given by the spectral width of the pre-filter. With its high speed capabilities CRISP is an ideal instrument for studying the dynamics of the chromosphere through imaging spectroscopy. Here we are interested in the Ca II 8542 and Hα spectral lines. For Ca II 8542, CRISP has a transmission FWHM of 111 mÅ and a pre-filter FWHM of 9.3 Å. The transmission FWHM for Hα is 66 mÅ while the pre-filter has a FWHM of 4.9 Å. The combination of the SST adaptive optics system (Scharmer et al. 2003b) and the Multi-Object, Multi-Frame Blind Deconvolution image restoration technique (van Noort et al. 2005) results in high spatial resolution, down to the telescope diffraction limit (λ/D=0.″14 for Hα). Remaining small-scale seeing deformations introduced by the non-simultaneity of the narrowband CRISP images is minimized by using the cross-correlation method developed by Henriques (2012).

We analyze several high-quality datasets, each with different properties so that various properties of RREs can be addressed. Table 1 provides details on the different data sets. Data sets A and B are time series with extended wavelength coverage of both wings of the Ca II 8542 and Hα spectral lines. The other time series of 2011 May 5 (data set C) has an extremely high cadence (0.88 s) so that the dynamical evolution of RREs and RBEs are temporally resolved. Only 4 wavelength positions are sampled, ±1032 mÅ, line center, and the far blue wing at −2064 mÅ. For more details on the 2011

Table 1
Observational data sets.

Data set	Date	Spectral line	# Line positions	Cadence (s)	Duration (h:m:s)	Target	μ
A	2008 Jun 15	Ca II 8542	28	11.33	00:40:25	CH	0.987
B	2011 May 05	Hα	35	7.96	00:52:31	QS	1
C	2011 May 05	Hα	4	0.88	00:30:53	QS	1
D	2011 Sep 18	Ca II 8542	47	10.37	02:18:53	QS	1
E	2012 May 26	Hα	33	(...)	(...)	QS, CH	[1–0]
F	2012 Jun 02	Hα	33	(...)	(...)	QS, CH	[1–0]

Note. — CH: coronal hole, QS: quiet Sun.

May 5 data sets, see Paper III. Data set A was analysed in Paper I but the data was re-processed for this study: now an efficient correction was applied to deal with artefacts caused by the semi-transparency of the back-illuminated CCD chips at longer wavelengths (for details see de la Cruz Rodríguez 2010). Artefacts were effectively removed and led to a significant increase in the number of RBE detections.

For the other 3 data sets, the observations were recorded under conditions of "snapshot" seeing: the seeing varied between extremes of total blurriness and crystal-clear sharpness. Most of the time during snapshot seeing, the conditions are useless for science analysis but the intervals of good quality are of sufficiently long duration to cover the acquisition of a complete spectral line scan. On 2011 September 18 (data set D), this yielded a large number of disk center Ca II 8542 line scans with a dense sampling down to 55 mÅ (half of the CRISP transmission FWHM). On 2012 May 26, Hα line scans at 7 disk positions were acquired (data set E), starting at disk center and following the central meridian down to the South Pole in intervals of $\mu = 0.1$ (with $\mu = \cos(\theta)$ and θ the observing angle). On 2012 June 2 (data set F), the central meridian from disk center to the North Pole was covered by 22 Hα line scans (down to 86 mÅ sampling), combining into a near-continuous center-to-limb scan (continuous with the exception of one narrow interruption – see Fig 7). Precise pointing information was obtained from co-alignment with full disk images from the 1700 Å channel of the AIA instrument (Lemen et al. 2012) on NASA's Solar Dynamics Observatory. Using photospheric bright points in the far Hα wing as reference, sub-arcsecond accuracy in the co-alignment can be achieved.

3. METHOD

For each dataset used in this study, an automated detection routine designed for locating and analyzing RBEs was used to find both RBEs and RREs. The same detection method (with slight modifications) was used in earlier studies (Rouppe van der Voort et al. 2009; Sekse et al. 2012, 2013) When searching for RREs, the automated detection routine worked on inverse Doppler images and hence, found RREs in a similar way as RBEs. For Hα, the Dopplergrams were at $\sim$45 km s^{-1}, for Ca II 8542 at 20 km s^{-1}. In the process of detecting RREs we set the threshold of minimum length of the detected events to 20 pixels or $\sim$0.86 Mm (17 pixels for data set A from 2008, when the images scale was slightly larger then for the later data sets). This is longer than for our previous studies (17 pixels in Paper II and 14 pixels in Paper III) which was found to be necessary in order to avoid detecting false positives. For example, false positives are caused by the presence of small-scale downflowing features, or flocculent flows (Vissers & Rouppe van der Voort 2012). Flocculent flows are ubiquitously present in the vicinity of magnetic field concentrations and have distinctively different morphology and dynamical behavior than the RREs that we study here. For each detection, the automated routine records the spatial and temporal position as well as determining the Doppler velocity and Doppler width along the event. Doppler velocity and width were determined on a residual profile, obtained from subtracting the RRE/RBE profile from a reference profile that was constructed from averaging line profiles over the whole FOV. Furthermore, the automated detection routine attempts to link up detected events in successive frames into multi-frame RREs and RBEs which can be used for measurements of lifetimes, transverse motion, and longitudinal motions.

Every dataset was analysed for both RREs and RBEs in order to make comparisons and previously searched datasets were re-examined with the updated length constraint in order to make a proper comparison.

The verification of RREs and the creation of space-time diagrams was done with the widget based analysis tool CRISPEX (Vissers & Rouppe van der Voort 2012) which allows for efficient exploration of multi-dimensional datasets.

4. RESULTS

When searching on-disk Hα and Ca II 8542 datasets for excursions in the red wing, many events are detected. These events are very similar in appearance and morphology as RBEs. Figures 1 and 2 show details of RREs in comparison with RBEs. Figure 1 shows an RRE event observed in Hα. Just after the event disappeared in the Hα red wing, an RBE appeared in the blue wing just adjacent to where the RRE was before. This RBE is shown in the right column of Fig. 1. Figure 2 shows RRE and RBE events in Ca II 8542. These events were visible as an RRE/RBE pair of adjacent events of similar length and morphology giving a strong impression of being part of the same spicule structure. The middle panels (c and d) of these figures show the detailed line profiles at a central location in the event, together with reference average line profiles. Just like for RBEs, the RREs are characterised by an asymmetry of the line profile with enhanced depression of the line wing – in the red wing rather than the blue wing. Likewise, the

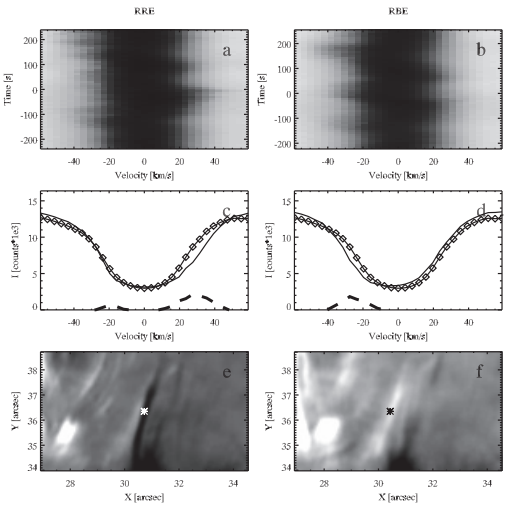

Figure 1. Details of an RRE (left column) and an RBE (right column) that occur in rapid succession in neighbouring locations in Hα (data set B). The top row shows the temporal evolution of the spectrum at a central location in the RRE and RBE, marked with asterisks in panels (e) and (f). The middle row shows the detailed spectral profiles (solid line) of the positions marked with asterisks in panel (e) and (f) at the time of the background image. The line profile marked with diamonds is an average over the whole FOV shown as reference. The thick dashed line is the difference between the average profile and the RBE/RRE profile which is used to calculate the Doppler velocity and width of the event from. The bottom row shows 35 km s^{-1} Doppler images of the RRE (dark) and RBE (bright) separated by a couple of timesteps.

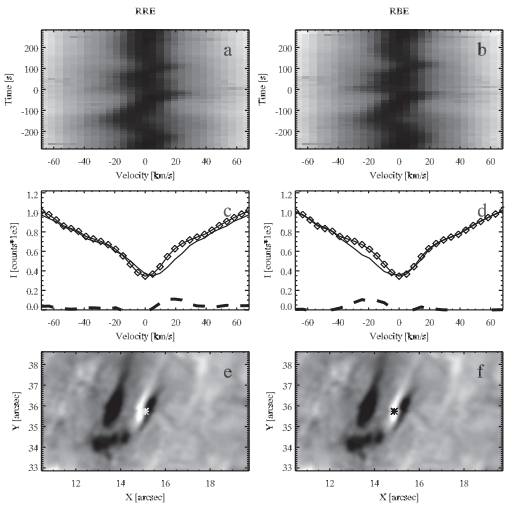

Figure 2. Details of an RRE and RBE observed in Ca II 8542 (data set A). The panels follow the same format as Fig. 1. Both the RRE and RBE are present in the same timestep and appear to be part of the same spicule structure. The background 20 km s^{-1} Dopplermaps in panels (e) and (f) are the same. The same event is shown in more detail in the right column of Fig. 8

temporal evolution for RREs and RBEs is similar: the asymmetry of the line profile is rather short-lived with comparable lifetimes for the two type of events. This is illustrated in the top panels (a and b). Furthermore, as can be seen from the bottom panels, the morphology for RREs and RBEs is similar: narrow, elongated structures often protruding from regions with enhanced magnetic fields (bright points, network regions, etc).

The measurements of Doppler velocities, Doppler widths, and lengths for detected events in the data sets A (Ca II 8542) and B (Hα) are shown in Fig. 3. As a way to suppress the contribution from possible false detections, we only include measurements on events that are part of a multi-frame event, i.e., events that could be identified in successive detection images and were therefore connected over a sequence of time steps. These measurements were done per time step. Doppler velocities and width measurements are averages over the detection length of the event. There are significantly more events in the blue wing than in the red wing: for the 52 min Hα quiet Sun time series (B) there are 3128 RBE and 1354 RRE detections (43%), whereas for the 40 min Ca II 8542 coronal hole time series (A) there are 2544 RBE and 1237 RRE detections.

From the histograms in Fig. 3 it is clear that for these properties, RREs (solid lines) are very similar to RBEs. Each property shows largely overlapping distributions. For Ca II 8542 RREs we see Doppler velocities lying mainly between 10 and 20 km s^{-1}, Doppler widths ranging from 1 to 20 km s^{-1}, and lengths ranging mainly from 1 Mm up to approximately 4.5 Mm. These RRE properties are comparable to the RBE properties (dashed lines) found in the same data set with only minor differences in that Doppler widths and lengths for RBEs are shifted to slightly higher values: average Doppler width for RREs at 7.0 km s^{-1} and for RBEs at 8.2 km s^{-1}, and average length for RREs at 2.5 Mm and for RBEs at 2.9 Mm. For Hα, the distributions for Doppler velocities (ranging between $\sim$20 and $\sim$35 km s^{-1}) and lengths (between $\sim$1.5 and $\sim$4.5 Mm) are almost identical for RREs and RBEs. For Hα Doppler widths, the distribution for RREs is slightly lower: the average for RREs is 7.5 km s^{-1}and for RBEs 8.7 km s^{-1}.

The variation of Doppler velocity and Doppler width along RREs and RBEs is shown in Figs. 4 (Hα) and 5 (Ca II 8542). In these figures, the variation of Doppler signal is shown in colour coding drawn at the physical locations of RREs and RBEs on a background image of the FOV. For each pixel, colour indicates the average value for all events that occurred at that location during the time series. Comparing the top and bottom rows in these figures, it is evident that there are more events in the blue wing than in the red wing: RBEs are more frequent than RREs (see above for detailed numbers). Furthermore, the spatial distribution of RREs is very similar to RBEs: mostly concentrated around regions of enhanced magnetic activity. RREs and RBEs occur at the same spatial locations.

Paper III shows comparable maps of Hα RBE Doppler velocity and width for the same data set (B) in their figure 1 as we do here in Fig. 4c and d. The differences are that in Paper III a shorter detection length

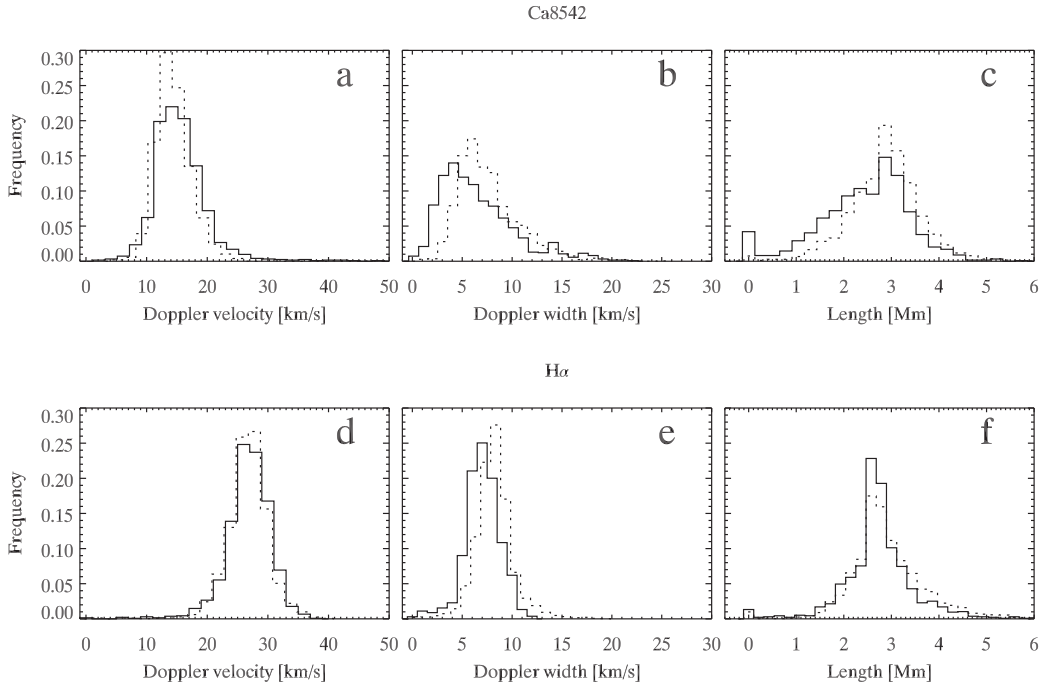

Figure 3. Histograms of RRE (solid line) and RBE (dashed line) properties in Ca II 8542 (top row) and Hα (bottom row). Doppler velocities (a and d) and Doppler widths (b and e) are averaged over the length of the event. Lengths are presented in panels (c) and (f). Number of measurements, Ca II 8542 data set A: 1237 RREs and 2544 RBEs, Hα data set B: 1354 RREs and 3128 RBEs.

constraint was used (resulting in 1.7 times more RBE detections) and a slightly different method of drawing these maps: events were drawn in sequential order so that later events mask earlier events. The maps in Fig. 4c and d have smoother appearance than their counterparts in Paper III but the same picture emerges: there appears to be no clear general trend for the variation of Doppler properties along the length of RBEs in this disk center quiet Sun time series. Similarly, the RRE Doppler properties in the top row panels seem to lack a clear general trend too. In the Doppler velocity map of Fig. 4a, there might be a weak preference for higher velocities towards the footpoints, closer to the magnetic network concentrations (a trend of more red in the lower parts of the RREs). For the Doppler widths in Fig. 4b, there might be a preference for lower widths towards the footpoints (more blue towards the bottom). Note that the trend of more dark and blue colours in the RRE Doppler width map as compared to the RBE Doppler width map reflects the lower Doppler width distribution for RREs in Fig. 3e.

The Doppler property maps for Ca II 8542 RBEs in Fig. 5c and d can be compared with the left panels of figure 12 of Rouppe van der Voort et al. (2009). They showed Doppler properties of 413 Ca II 8542 RBEs from the same data set but detected in Dopplermaps at 30 km s^{-1}. Here we show results from 3655 Ca II 8542 RBE events detected in 20 km s^{-1} Dopplermaps. We confirm the results from Paper I: in this coronal hole data set, there is a trend for increasing Doppler velocity and width along RBEs (in the colour scheme of this figure: a trend of more red towards the top end of RBEs). For Ca II 8542 RREs in the top panels of Fig. 5 the variation is much more diverse and it is hard to see any clear trend.

4.1. *Center to Limb Variation*

To further explore the occurrence of RREs on the solar disk, we ran the detection method on data sets at various disk positions. The detection was done on Dopplergrams at about the same wavelength offset for all different data sets: approximately ± 45 km s^{-1}. Figure 6 shows the number of RRE and RBE detections as function of disk position $\rho = r/R_\odot$ with r the distance from disk center and $R_\odot$ the solar radius. The numerous dots around $\rho = 0$ are the detection numbers from every frame of the 52 min data set A taken at disk center (396 time steps). Generally, more RBEs are detected than RREs. Although there is a significant scatter to the number of detections, we see a clear trend of increasing numbers of both RREs and RBEs being detected towards the limb. The solid and dashed lines are linear fits to the RRE and RBE detection numbers, respectively, and show an increase in the average number of detections from 5.3, at

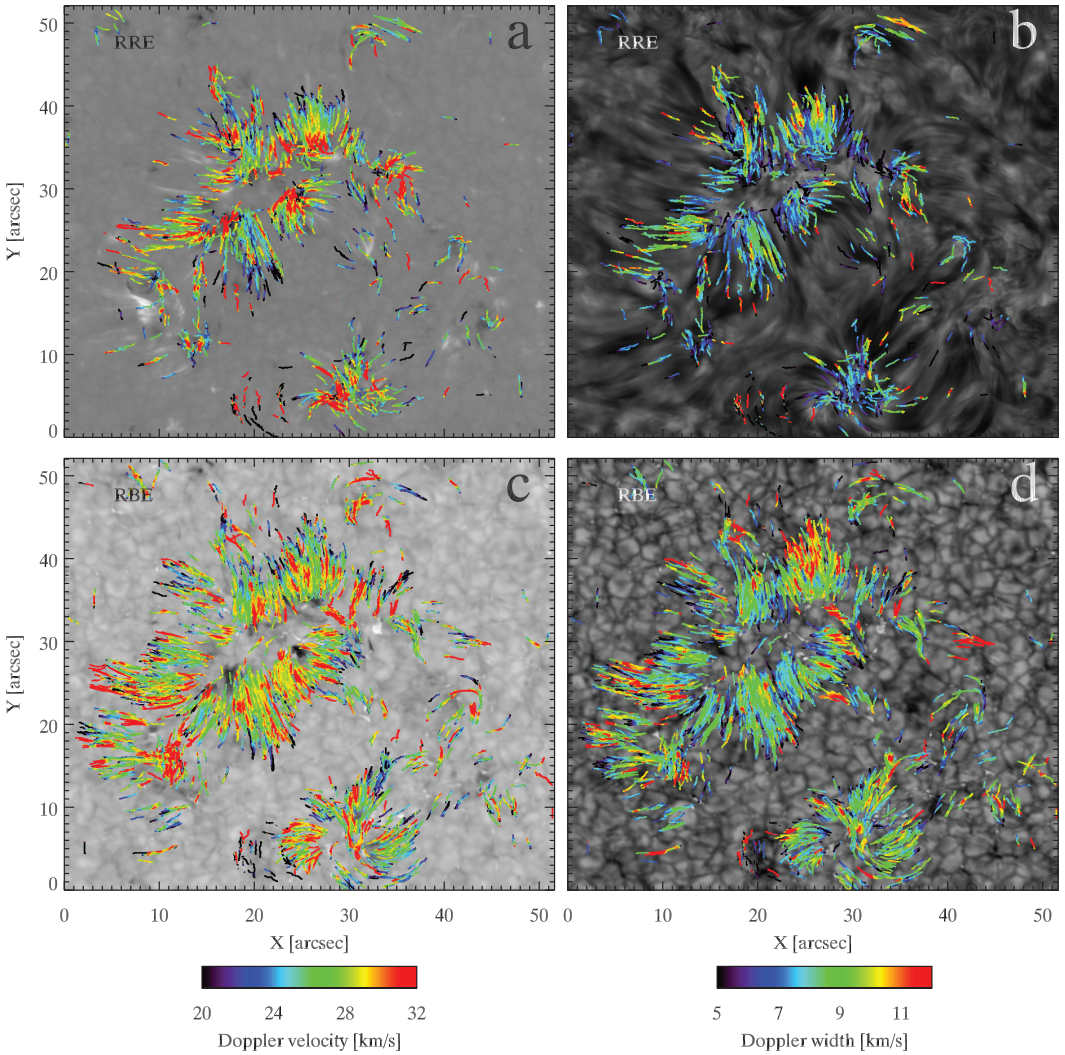

Figure 4. Hα Doppler properties as function of position along RREs and RBEs drawn at their location in the FOV. RREs are plotted in the top row and RBEs in the bottom row, with Doppler velocities being displayed in the left column and Doppler widths in the right column. Background images are ±1032 mÅ Doppler image (a), line core (b), +1032 mÅ red wing (c), and far blue wing image (d).

disk center, to 14.4, near the limb, for RREs, and from 10.1 to 19.4 for RBEs.

Figure 7 shows a number of close-up images centered on network regions at various disk positions. The center-to-limb scan of data set F mainly covered quiet Sun, it crossed a large equatorial coronal hole between heliocentric y=0″–210″. The upper-left close-up image is from the coronal hole (y=152″–174″). Over the whole disk, RREs and RBEs are observed in close vicinity. Most often, RREs and RBEs are seen in isolation, but there are a number of examples of RRE/RBE pairs where the RRE and RBE signal is observed in parallel and touching structures, suggestive of being part of the same physical entity. A prominent example is visible in the lower left panel (y=694″–704″) but close inspection reveals examples in every close-up image.

4.2. *Torsional motion*

Parallel and touching RRE/RBE pairs are found over the whole solar disk (see Sect. 4.1). Figure 8 shows examples from high spectral resolution Ca II 8542 scans close to disk center. The middle panels show spectrograms (λ-

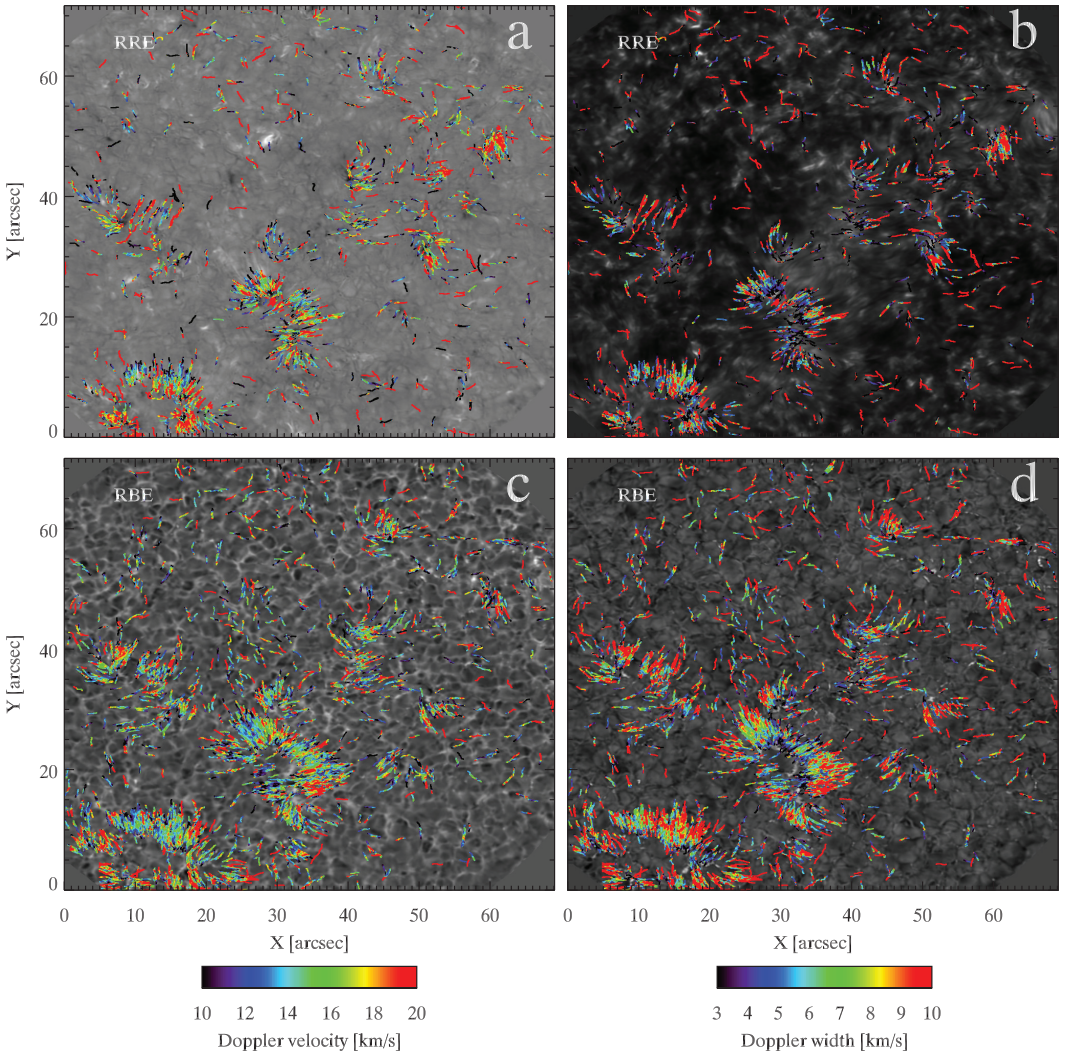

Figure 5. Ca II 8542 Doppler properties as function of position along RREs and RBEs drawn at their location in the FOV. RREs are plotted in the top row and RBEs in the bottom row, with Doppler velocities being displayed in the left column and Doppler widths in the right column. Background images are Ca II 8542 ±582 mÅ Doppler image (a), line core (b), +582 mÅ red wing (c), and far blue wing (d).

x diagrams) from an artificial "spectrograph slit" drawn in the direction transversal to the main axes of selected events close to a network region. The asymmetry of the spectral profiles changes rapidly from one wing to the other over short distances, resulting in tilted profiles in the spectrograms. For the main event in the left column, centered on $0''$ along the slit in the middle panel, the asymmetry changes from approximately $+20$ km s^{-1} to -20 km s^{-1} over only 250 km. Another less extreme example is visible at $-3.5''$ along the slit. The right column shows an example of an RRE/RBE pair with the asymmetry varying between approximately ± 20 km s^{-1} over the width of the structure.

4.3. *Temporal change between RREs and RBEs*

Besides parallel and touching RRE/RBE pairs, we frequently observe events for which the asymmetry changes from red-ward to blue-ward and vice versa. These changes are very rapid and the most convincing examples that these modulations really are occurring in the same physical structure can be found in the high temporal resolution dataset C (cadence 0.88 s). Figure 9 shows

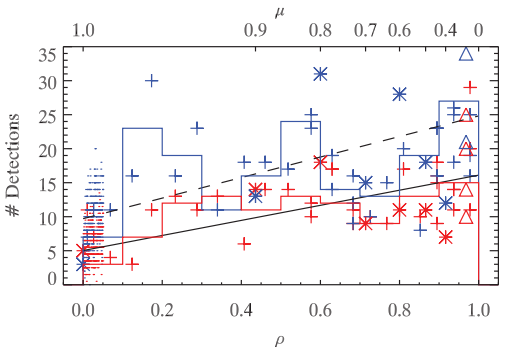

Figure 6. Number of detections of RREs (red) and RBEs (blue) per time step over the FOV of several datasets going from disc center ($\rho = r/R_\odot = 0$) to the solar limb ($\rho = 1$). Corresponding $\mu = \cos$(observing angle) scaling is shown on top. Dots near $\rho = 0$ signify data points from the disk center data set B, the spread in ρ is artificial to show the density of data points. Stars are from data set E, crosses are from F. The histogram bars are averages over the data points in $\Delta\rho = 0.1$ intervals. Linear fits to the data points are shown with a solid (RREs) and dashed (RBEs) line.

a few examples. The top panels show an event that starts as a long RRE of about 3″ length which changes into a short RBE that appears to be growing from the bottom. While the RBE appears, the RRE vanishes. This change occurs at a propagation speed that is estimated to be about 108 km s^{-1}. The bottom panels show two events that appear close to each other. The first event starts as an RRE (dark feature) that is centered on $\sim (17\farcs5, 34\farcs5)$ at $t = -16.1$ s and moves slowly (diagonally) upwards. At the same time, an RBE slowly grows from the bottom with a slight acceleration after about $t = 5$ s. The average propagation speed of the change is approximately 18 km s^{-1}. Almost parallel to this event, there is a similar event that starts as an RRE that is not visible before $t = 0$ s, the space-time diagram is shown as the rightmost panel. While the RRE slowly moves upward, an RBE grows at an approximate speed of 48 km s^{-1}. Similar space-time diagrams as the right panels of Fig. 9 were made for 7 other examples, finding propagation speeds between 18 and 102 km s^{-1}. The average over all events is 58 km s^{-1}.

5. DISCUSSION

The red wing counterpart of RBEs: narrow, elongated and short-lived absorption features in the Ca II 8542 and Hα lines in the form of asymmetries in the *red* wing, or RREs, can be observed in large abundance over the whole solar disk. They are very similar to RBEs in terms of length and average Doppler velocity, while the average Doppler width is slightly lower for RREs than for RBEs. Their spatial distribution is similar to RBEs: they are found around concentrations of enhanced magnetic field. We did not do a detailed study of the temporal evolution of RREs like in Paper III, but cursory inspection of our data suggests that the lifetimes of RREs are similar to RBEs. RREs are less abundant than RBEs, around disk center about half the number density, but significant numbers can be found anywhere on the disk.

When we reflect on our own work on the disk counterparts of type II spicules, we can identify several reasons why RREs were not identified earlier. One reason is that the observations from the early CRISP campaigns were not optimally suited to identify RREs. Limiting factors for the two data sets from 2008 that were used in Paper I: the Hα time series had an asymmetric spectral sampling that did not cover the red wing further than 800 mÅ. The Ca II 8542 time series (data set A in this study) suffered from artefacts related to the semi-transparency of the CCD chip at long wavelengths (see de la Cruz Rodríguez 2010). For this data set, this problem was not resolved until 2011. The 2010 observations acquired for follow-up studies (used in Paper II) were specifically designed for RBE detection: the Hα line was only sampled in the blue wing, and the Ca II 8542 sampling was relatively coarse.

It was not until high resolution off-limb Ca II H slit spectroscopy could be combined with high quality CRISP limb observations that the ubiquitous presence of torsional motions in spicules could be unequivocally established (De Pontieu et al. 2012). It was realised that spicules undergo three different types of motions at the same time: (1) field-aligned flows of order 50–100 km s^{-1}, (2) swaying motions of order 15–20 km s^{-1}, and (3) torsional motions of order 25–30 km s^{-1}. The presence of these three kinetic modes explained the appearance of spicular features in near-limb blue and red wing CRISP Hα and Ca II 8542 images. Bushes of red-shifted and blue-shifted features appear with similar morphology and orientation. Field-aligned flows towards and away from the observer alone cannot explain the striking similarity as the asymmetry of near-limb line-of-sight projection should cause large morphological inequality. Doppler modulation due to transverse motions from modes (2) and (3) can explain the presence of near-cospatial and morphologically similar absorption features in the blue and red wings of the near-limb CRISP observations. This understanding led us to this work investigating the presence of similar red-wing absorption features at disk positions further away from the limb.

We interpret the presence of RREs close to disk center as a strong indication that field-aligned flow cannot be the only type of plasma motion in spicules. High-amplitude transversal motions must be present too in order to produce an effective Dopplershift into the red wing. We find evidence for these transversal motions to be in the form of torsional motions and/or in the form of swaying motions.

The observation of parallel and touching RRE/RBE pairs is a direct indication of torsional or spinning motion in spicules (see Figs. 2, 6, and 8). We find a significant number of RRE/RBE pairs in our data but most common are isolated RREs and RBEs. The spectral profiles in λ-x diagrams extracted perpendicular to the main axes of isolated events in high-spectral resolution observations often show signs of tilts similar (but less pronounced) to the extreme cases of the RRE/RBE pairs in the middle row of panels in Fig. 8. This is most clear in the Ca II 8542 line which has a narrower core than Hα and therefore more pronounced Doppler modulation. This suggests that torsional motion is likely to be present in a large fraction of spicules and therefore an important kinetic mode.

The importance of swaying as a kinetic mode in RBEs

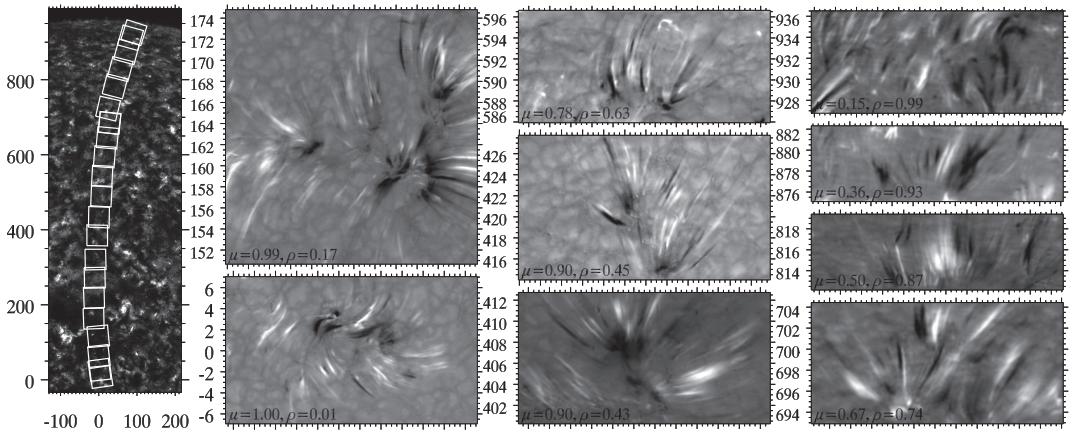

Figure 7. Examples of RRE + RBE concentrations around network regions at different disk positions from the center-to-limb scan of data set F. The left panel shows the various telescope pointings as white squares on the background of a co-temporal SDO/AIA 304 Å image. The 9 images are cutouts from ±1032 Hα Dopplergrams, each centered on network concentrations with enhanced RRE/RBE activity. RREs are white, RBEs are black. Axis labels in heliocentric coordinates (arcseconds).

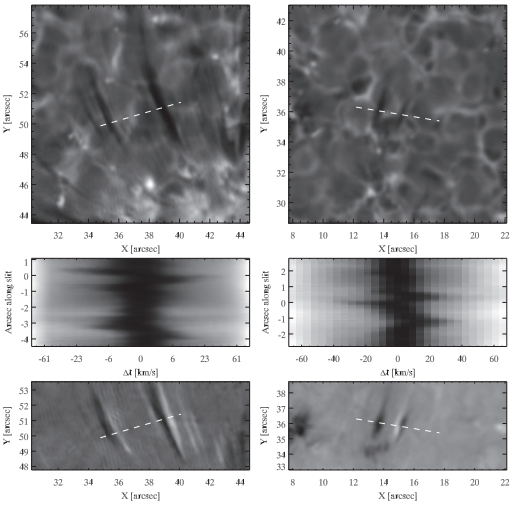

Figure 8. Examples of direct evidence of torsional motion in the disk counterpart of spicules. Spectral profiles are extracted from Ca II 8542 datasets (data set D in left column, data set A in the right column) in a direction perpendicular to the main axes of a number of RREs and RBEs (the "slit" drawn as white dashed lines in the Ca II 8542 images in the top panels). Top panels show Ca II 8542 red wing images (left: +440 mÅ, right: +582 mÅ). Corresponding spectrograms (or λ-x diagrams) are shown in the middle panels, with the origin of the y-axis centered on the main RRE/RBE pair. The bottom panels show ±16 km s^{-1} (left) and ±20 km s^{-1} (right) Dopplergrams with RREs black and RBEs white. Figure 2 shows more details of the right hand-side event.

was already evident from transverse motion measurements (see Papers I–III). The observation that most events are either RRE or RBE and not pairs can be interpreted as swaying producing significant offsets in the Dopplershift of these structures. Field-aligned up-flows can also result in a Doppler offset so that the dominance of isolated RRE and RBE events is probably due to the combined effect of both kinetic modes. Figure 10 illustrates the effect of swaying and/or up-flows on the observed Dopplershift from a tube with torsional motion. Only in the situation that these modes do not produce a significant net velocity component along the line-of-sight, a clear RRE/RBE pair can be detected.

The observation of finding generally more RBEs than RREs suggests that plasma up-flows are present in spicules and result in a bias towards blue-shifts. For the center-to-limb variation of the detection numbers, we see that the total number of detected events increases towards the limb (i.e., both more detected RBEs and RREs). In addition, we see that the number of RREs increases relatively more than the number of RBEs. Partly, the increase in total number of detected events towards the limb can be explained by the curvature of the Sun and the related increase of the solar surface covered by the fixed size of the FOV when pointing closer to the limb. In addition, this can be interpreted as resulting from transversal motions gaining weight as the line-of-sight becomes more inclined to the average spicule axis as we go towards the limb. The net contribution from field-aligned flows would decrease closer to the limb and we see a more balanced ratio of RRE to RBE detections: from RRE/RBE ≈ 0.52 near disk center to ≈ 0.74 near the limb.

The transition from RREs into RBEs and vice versa (see Fig. 9) can be interpreted as the result of an Alfvénic wave associated with the swaying motion. The exact nature of the wave is difficult to determine since the associated time scale is so short (high propagation speed). Only in the high temporal resolution dataset (cadence 0.88 s) we found a number of convincing examples where these changes were occurring in the same physical structure. Such high cadence observations could only be acquired at the expense of high spectral resolution so that valuable diagnostic information that could provide more

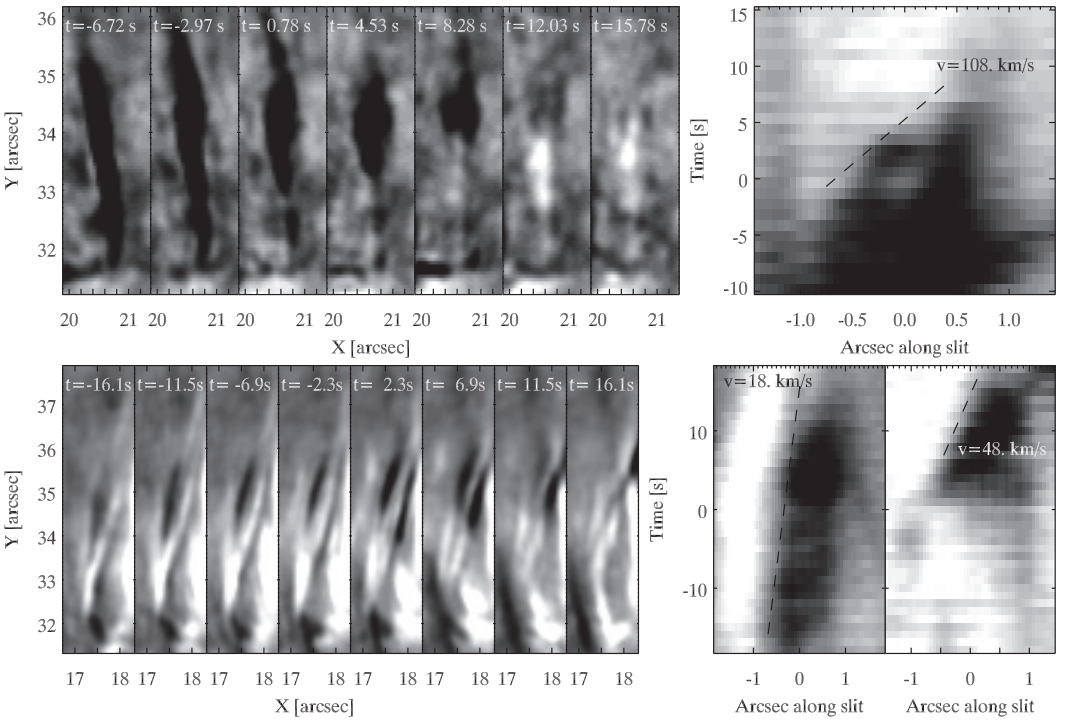

Figure 9. Examples of the rapid change from RRE to RBE in the fast Hα dataset C. Left panels: sequential images showing the time evolution of the transition from one form into the other. The right panels show the space-time (x-t) diagrams from a slit drawn along the RRE/RBE axis. The dashed lines serve as reference for a propagation speed for the transition. In the bottom panels, two examples of transitions from RRE to RBE can be seen. Both events are diagonally oriented in the images on the left. The left x-t diagram is associated with the RRE (dark feature) that is visible from the start of the sequence of images. The right x-t diagram is associated with the event slightly below that does not appear as an RRE before $t = 0$.

insight into the physical nature of the changes is lacking.

6. CONCLUSION

In a number of high-quality data sets with different observational characteristics (variation in e.g., spectral line sampled, temporal and spectral resolution, observing angle and target) we find clear evidence of the presence of three different types of motion in the disk counterpart of type II spicules: (1) field aligned flows, (2) swaying motions, and (3) torsional motions. Our results support the findings of De Pontieu et al. (2012) who established the presence and relative importance of these three kinetic modes in spicules at the limb. Rotational motion in spicules had been reported in the earlier literature (e.g., Beckers 1968; Pasachoff et al. 1968; Weart 1970) but only with the aid of modern observational techniques the ubiquity of this type of motion could be determined. We also see evidence for propagation of both the swaying and torsional motions, which is compatible with the presence and propagation of Alfvénic waves. Our analysis on the disk counterpart of type II spicules reinforces the conclusions of De Pontieu et al. (2012): the combined action of all three kinds of motion needs to be considered when interpreting spicule Doppler signals to estimate their contribution to the transport of plasma and energy through the solar atmosphere.

The Swedish 1-m Solar Telescope is operated by the Institute for Solar Physics of the Royal Swedish Academy of Sciences in the Spanish Observatorio del Roque de los Muchachos of the Instituto de Astrofísica de Canarias. B.D.P was supported through NASA contracts NNG09FA40K (IRIS), NNX11AN98G, and NNM12AH46G. We thank Sven Wedemeyer, Jorrit Leenaarts, Jaime de la Cruz Rodríguez, Ada Ortiz Carbonell, Ida Benedikte Hole, Håkon Skogsrud, and Gregal Vissers for their help during different observation campaigns. This research has made use of NASA's Astrophysical Data Systems.

REFERENCES

Beckers, J. M. 1968, Sol. Phys., 3, 367
de la Cruz Rodríguez, J. 2010, PhD thesis, Stockholm University (ArXiv e-prints 1204.4448)
De Pontieu, B., Carlsson, M., Rouppe van der Voort, L. H. M., et al. 2012, ApJ, 752, L12
De Pontieu, B., McIntosh, S., Hansteen, V. H., et al. 2007a, PASJ, 59, 655
De Pontieu, B., McIntosh, S. W., Carlsson, M., et al. 2011, Science, 331, 55

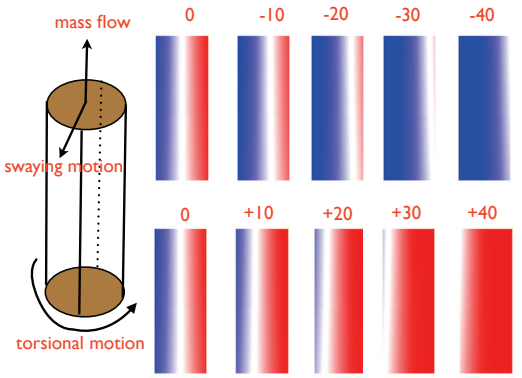

Figure 10. Illustration of the effect of the line-of-sight component from up-flow and/or swaying motion to the Doppler profile of a tube that undergoes torsional motion. The tube geometry is sketched on the left-hand side, with the observing angle $\neq 90^{\circ}$ to the tube's long axis so that both the up-flow along the tube and the swaying motion can have a non-zero component along the line-of-sight. The two rows with panels on the right show the Doppler profile in blue/red shift for varying line-of-sight velocities (denoted in km s^{-1} at the top, for a 40 km s^{-1} line-of-sight component from the torsional motion).

De Pontieu, B., McIntosh, S. W., Carlsson, M., et al. 2007b, Science, 318, 1574

De Pontieu, B., McIntosh, S. W., Hansteen, V. H., & Schrijver, C. J. 2009, ApJ, 701, L1

Henriques, V. M. J. 2012, A&A, 548, A114

Judge, P. G., Reardon, K., & Cauzzi, G. 2012, ApJ, 755, L11

Langangen, Ø., De Pontieu, B., Carlsson, M., et al. 2008, ApJ, 679, L167

Lemen, J. R., Title, A. M., Akin, D. J., et al. 2012, Sol. Phys., 275, 17

Okamoto, T. J. & De Pontieu, B. 2011, ApJ, 736, L24

Pasachoff, J. M., Noyes, R. W., & Beckers, J. M. 1968, Sol. Phys., 5, 131

Pereira, T. M. D., De Pontieu, B., & Carlsson, M. 2012a, ApJ, 759, 18

Pereira, T. M. D., De Pontieu, B., & Carlsson, M. 2012b, ArXiv e-prints

Rouppe van der Voort, L., Leenaarts, J., de Pontieu, B., Carlsson, M., & Vissers, G. 2009, ApJ, 705, 272

Scharmer, G. B., Bjelksjo, K., Korhonen, T. K., Lindberg, B., & Petterson, B. 2003a, in Society of Photo-Optical Instrumentation Engineers (SPIE) Conference Series, Vol. 4853, Society of Photo-Optical Instrumentation Engineers (SPIE) Conference Series, ed. S. L. Keil & S. V. Avakyan, 341–350

Scharmer, G. B., Dettori, P. M., Lofdahl, M. G., & Shand, M. 2003b, in Society of Photo-Optical Instrumentation Engineers (SPIE) Conference Series, Vol. 4853, Society of Photo-Optical Instrumentation Engineers (SPIE) Conference Series, ed. S. L. Keil & S. V. Avakyan, 370–380

Scharmer, G. B., Narayan, G., Hillberg, T., et al. 2008, ApJ, 689, L69

Sekse, D. H., Rouppe van der Voort, L., & De Pontieu, B. 2012, ApJ, 752, 108

Sekse, D. H., Rouppe van der Voort, L., & De Pontieu, B. 2013, ApJ, 764, 164

Suematsu, Y., Ichimoto, K., Katsukawa, Y., et al. 2008, in Astronomical Society of the Pacific Conference Series, Vol. 397, First Results From Hinode, ed. S. A. Matthews, J. M. Davis, & L. K. Harra, 27

Tsiropoula, G., Tziotziou, K., Kontogiannis, I., et al. 2012, Space Sci. Rev., 65

van Noort, M., Rouppe van der Voort, L., & Löfdahl, M. G. 2005, Sol. Phys., 228, 191

Vissers, G. & Rouppe van der Voort, L. 2012, ApJ, 750, 22

Weart, S. R. 1970, Sol. Phys., 14, 310